Università di Pisa

DIPARTIMENTO DI FISICA
Corso di Laurea Magistrale in Fisica

A novel method for searching for CP violation in the $D^0 \to K_s^0 K^\pm \pi^\mp$ decays with LHCb Run 2 data

Candidate:
Alice Biolchini

Advisor:
Dr. Michael J. Morello

Anno Accademico 2019-2020

Contents

Introduction

The Standard Model (SM) of particle physics is nowadays the widely accepted theory describing electroweak and strong interactions. It has demonstrated a great success during the last decades, providing a very large number of precise predictions and a quantitative interpretation of everything we observed in particle physics experiments. However, it leaves some phenomena unexplained, such as the nature of Dark Matter (if it does exist), the baryon asymmetry in our Universe, and last but not least, it is not yet able to fully accommodate a quantum theory of gravity. Physicists are therefore looking for any 'crack' of the theory in order to search clues of New Physics (NP).

The non-invariance of the weak interaction under the combined action of the charge conjugation (C) and the parity (P) operators is commonly referred as *CP* violation, and it is introduced in the SM through a single irreducible complex phase inside the Cabibbo-Kobayashi-Maskawa (CKM) quark mixing matrix [1, 2]. The search, and eventually a discovery, of new sources of *CP* violation is one of the main goal of High Energy Physics, since the amount of *CP* violation produced through the CKM mechanism and measured in the past and present experiments, is too tiny to explain the cosmological baryonic asymmetry observed in our universe. Recent theories predict new sources of *CP* violation, given by the existence of new particles beyond the SM at energy scales much higher than those explored at the LHC that could exclusively couple with the up-type quarks, and all experimental measurements so far, may have missed possible anomalies detectable only in the charm hadrons. In fact, the top quark decays too fast and it is not able to hadronise and form a neutral 'T^0' meson, while the π^0 meson and its antiparticle are the same particle. The charm quark is therefore the only up-type quark in which the *CP* violation can be studied in all its manifestations and possible deviations from the SM predictions can be experimentally observed.

The LHCb Collaboration has recently reported the first observation of *CP* violation in the decay of charm mesons on March 2019, looking at the golden observable, $\Delta A_{CP} = A_{CP}(D^0 \to K^+K^-) - A_{CP}(D^0 \to \pi^+\pi^-)$. It returned to be significantly different from zero, $\Delta A_{CP} = (-15.4 \pm 2.9) \cdot 10^{-4}$ [3], where the uncertainty includes both statistical and systematic contributions. This discovery opens a new interesting research frontier, with the aim of shedding light on the origin of such 'direct' *CP* violation manifestation [4, 5, 6, 7]. Is this standard or non-standard? In order to answer to this question, it is of fundamental importance to study many other charm decays and, eventually, observe similar *CP*-violating asymmetries. It would certainly help to constrain the effect from both an experimental and theoretical point of view and drastically increase our knowledge of the dynamics of heavy flavours, hopefully claiming new phenomena.

A large variety of physics can be accessed by studying the $D^0 \to K_S^0 K^- \pi^+$ and $D^0 \to K_S^0 K^+ \pi^-$ decays [1]. Both modes are singly Cabibbo-suppressed (SCS), with the $K_S^0 K^- \pi^+$ final state favored by ~ 1.5 with respect to its $K_S^0 K^+ \pi^-$ counterpart [8]. They are of interest for improving knowledge of the CKM matrix, *CP* violation measurements and mixing studies in the neutral D system. Analysis of the relative amplitudes of intermediate resonances, contributing to these decays, can help in understanding the behavior of the strong interaction at low energies. These decay channels, in particular those occurring through the $K^{*0} \to K\pi$ intermediate resonance, are a promising laboratory for probing hints of new sources of *CP* violation because SM predictions are very small (SM) ≤ 0.003, as explained in Ref. [9].

The LHCb Collaboration performed a full time-integrated amplitude analysis of these decays [8], with the aim of searching for local *CP* violation and measuring coherence factors and associated parameters. These studies used a data sample from pp collisions corresponding to an integrated luminosity of about 3 fb^{-1} collected by the LHCb detector during 2011 and 2012 (LHC Run 1) at center-of-mass energies $\sqrt{s}$ = 7 and 8 TeV, respectively. This sample contains about 190,000 signal decays, around one hundred times more than those were analyzed in a previous amplitude study of the same modes performed by the CLEO collaboration [10]. So far, no significant *CP*-violating effect has been found. However, LHCb collected an additional data sample of pp collisions, corresponding to an integrated luminosity of about 5.6 fb^{-1}, from 2015 to 2018 (the so called LHC Run 2) at center-of-mass energy $\sqrt{s}$ = 13 TeV, increasing the signal yields by about a factor 9, collecting about 1.7 million signal candidates, much higher than the factor of 2 expected from the only increase of the integrated luminosity. This is mainly due to the optimized trigger system and to the increase of the charm production cross section at the new center-of-mass energy of 13 TeV. Therefore, it is now possible to explore the region with a level of accuracy of per mil for such decay modes.

In this context, this thesis describes a new original analysis methodology to search for the time-integrated *CP* asymmetry, at very high precision, in the $D^0 \to K_S^0 K^\pm \pi^\mp$ decays using the full LHCb Run 2 data sample, without performing a full amplitude analysis as the previous LHCb measurement. A model-dependent approach is usually very complex and necessitates an accurate knowledge of a dynamic model [2] to account for all the intermediate resonances contributing to the process of interest. As suggested in Ref. [9], instead, this work aims at searching for *CP*-violating effects using a model-independent approach in order to exploit the whole sensitivity of the current available LHCb data sample. The methodology developed in the thesis allows measuring the time-integrated *CP*-violating asymmetry, both by integrating over the entire phase space (or the so-called Dalitz plot) and in a restricted region, such as in the vicinity of the $K^*(982)^0 \to K^+\pi^-$ resonance.

The neutral D^0 mesons are produced in pp collisions at the LHC, and they can be reconstructed using the $D^*(2010)^+ \to D^0\pi^+$ strong decays, where the charge of pion identifies the flavour of the neutral meson at production. The "raw" asymmetry of a final

[1] The inclusion of charge-conjugate processes is implied, except in the definitions of *CP* asymmetries.

[2] The model is usually built and refined during the analysis itself with the associated systematic uncertainties.

state f can be computed as follows:

$$A_{\text{raw}}(f) = \frac{N(D^0 \to f) - N(\overline{D}^0 \to \bar{f})}{N(D^0 \to f) + N(\overline{D}^0 \to \bar{f})},$$

where N stands for the number of reconstructed neutral D meson candidates. This asymmetry includes the contribution of the direct *CP* asymmetry, A_{CP}, along with the contribution of the production and detection asymmetries. The driving idea of the method developed in this thesis exploits the cancellation of all nuisance asymmetries through the famous ΔA_{CP} mechanism [3] between decay modes with very similar kinematics, and collected with similar online and offline selections. The $D^0 \to K^0_S\pi^+\pi^-$ decay mode is dominated by Cabibbo-favoured processes, where the direct *CP*-violating asymmetry [3] is expected to be negligible compared to the experimental uncertainty achievable with the available $D^0 \to K^0_S K^\pm\pi^\mp$ signal decays. Therefore, it can be used as an excellent calibration mode.

The difference of the two raw asymmetries allows a reliable cancellation of the asymmetry in producing a charged D^* meson at the LHC, $A_P(D^*)$, and of the detector-induced charge asymmetry in reconstructing the "soft" pion to form a D^* meson candidate, $A_D(\pi_s)$. However, residual detection asymmetries survive the cancellation mechanism, such as the detector-induced charge asymmetry in reconstructing the $K\pi$ pair, $A_D(K\pi)$, and the detection asymmetries due to the different probability of interaction with matter of neutral kaons, also including *CP*-violating effects present in the kaon system, $A_D(K^0)$.

The novel analysis methodology developed in this thesis aims at the cancellation of all these nuisance asymmetries at the per mil level to probe possible new sources of *CP*-violating asymmetries in the $D^0 \to K^0_S K^\pm\pi^\mp$ decays, using the full data sample collected by the LHCb experiment during the LHC Run 2. As a first stage of the work, the offline selection of the signal data samples is optimized with the aim of improving the statistical uncertainty on the observable of interest $A_{CP}(D^0 \to K^0_S K^\pm\pi^\mp)$. A fine scan of a multidimensional space is performed in order to find the configuration with the optimal value of the well known $S/\sqrt{S+B}$ figure of merit, linked to the statistical uncertainty on A_{CP}. In order to obtain a reliable cancellation in the differences, the kinematics of the signal and calibration modes is equalized in a multidimensional space of both D^*, D^0 and all the decay products. Particular attention is devoted to the removal of the neutral kaon asymmetry, which requires a time-dependent analysis as a function of the K^0_S proper decay time, and to the analysis strategy to determine the $A_D(K\pi)$ detection asymmetry. Lastly, a short review of possible dominant systematic uncertainties is also reported in the thesis.

[3] Mixing induced *CP*-violating effect are also very small, below the level of 10^{-4} from experimental bounds.

1 *CP* violation in the charm sector

This chapter provides a short overview of CP violation in the charm quark sector in the context of the Standard Model framework, along with a short introduction to the experimental techniques used to collect huge samples of charm hadrons data.

1.1 The Standard Model

The Standard Model (SM) of particle physics is a quantum field theory describing electroweak and strong interactions between elementary particles. It is based on three main ingredients:

- the symmetries of the Lagrangian;
- the representations of fermions and scalars;
- the pattern of spontaneous symmetry breaking.

The gauge group of symmetry of the SM is defined as

$$G_{SM} = SU(3)_C \otimes SU(2)_L \otimes U(1)_Y \tag{1.1}$$

where $SU(3)_C$ is the symmetry group of the Quantum Chromo-Dynamics (QCD), which describes the strong force theory, with the subscript C standing for the color charge of the field under a trasformation of this group. The group $SU(2)_L \otimes U(1)_Y$ represents the symmetry group of the electro-weak interactions as introduced by the theory of Glashow-Weinberg-Salam. In this case, the subscripts L and Y refers to the chirality of the weak interactions and to the hypercharge, respectively. The representations of the building blocks of matter under these symmetries read

$$Q^I_{Li}(3,2)_{+1/6}, \quad u^I_{Ri}(3,2)_{+2/3}, \quad d^I_{Ri}(3,1)_{-1/3}, \quad L^I_{Li}(1,2)_{-1/2}, \quad \ell^I_{Ri}(1,1)_{-1}, \tag{1.2}$$

where $i = 1,2,3$ runs over the generation of fermions (generation index), the index $L(R)$ indicates the left (right) chirality, while the index I denotes the interaction eigenstates. Finally, there is a single scalar multiplet:

$$\phi(1,2)_{+1/2}. \tag{1.3}$$

The following compact notation is very useful because it manifests the quantum number of the field. For example, the left-handed quarks, Q^I_L, are in a triplet of the

$SU(3)_C$ group, a doublet of $SU(2)_L$ and carry hypercharge $Y = +1/6$. Therefore, the numbers between the parenthesis are the dimensions of the representation of the $SU(3)_C$ and $SU(2)_L$ groups and the subscript is the hypercharge. The $SU(2)_L$ doublets can be decomposed into their components

$$Q^I_{Li} = \begin{pmatrix} u^I_{Li} \\ d^I_{Li} \end{pmatrix}, \quad L^I_{Li} = \begin{pmatrix} \nu^I_{Li} \\ \ell^I_{Li} \end{pmatrix}.$$

Usually, these particles are identified under two main groups:

- *quarks* (Q^I_{Li}, u^I_{Ri}, d^I_{Ri}) that are $SU(3)_C$ triplets and interact with the strong force;
- *leptons* (L^I_{Li}, $\ell^I_{Ri}(1,1)_{-1}$) that are $SU(3)_C$ singlets.

It is also possible to use a different classification:

- *left-handed* (Q^I_{Li}, L^I_{Li}) that are $SU(2)_L$ doublets and interact with W^i bosons;
- *leptons* (u^I_{Ri}, d^I_{Ri}, $\ell^I_{Ri}(1,1)_{-1}$) that are $SU(2)_L$ singlets, therefore they do not interact with W^i bosons,

where W^i (with $i = 1, 2, 3$) and B are the gauge fields coming from the electro-weak invariance under $SU(2)_L \otimes U(1)_Y$. The mix between W^3 and B bosons leads to the physically observed bosons Z^0 and A after the spontaneous symmetry breaking, that is due to the non-zero vacuum expectation value (VEV) of the additional scalar field ϕ. The expression of the VEV for the scalar field is:

$$\langle \phi \rangle = \frac{1}{\sqrt{2}} \begin{pmatrix} 0 \\ \nu \end{pmatrix}, \tag{1.4}$$

consequently the gauge symmetry group is spontaneously broken:

$$G_{SM} \to SU(3)_C \otimes U(1)_{EM}, \tag{1.5}$$

where $U(1)_{EM}$ is the symmetry group of electromagnetism. The field ϕ is often parameterized as

$$\phi(x) = \frac{1}{\sqrt{2}} \begin{pmatrix} 0 \\ \nu + H(x) \end{pmatrix} \tag{1.6}$$

where $H(x)$ is a neutral scalar field known as Higgs boson. Once the gauge symmetry, the particle content, and the pattern of spontaneous symmetry breaking are defined, the Standard Model Lagrangian, $\mathcal{L}_{SM}$, is derived as the most general renormalizable Lagrangian satisfying these requirements. The Standard Model currently provides the best description of the subatomic world but it does not explain the complete picture. In fact it incorporates three of the four fundamental forces, omitting gravity. Moreover the dark matter is not explained in the SM context, although there are several hints of its existence. The reasons why there are three generations of quarks and leptons is still an open question and also the mass scale hierarchy. For these reasons, it is easy to think that there is a more general theory able to include the SM as a lower energy approximation.

1.2 *CP* violation in the SM

In order to find a physics beyond the SM, the search of *CP* violation (CPV) plays an important role. Indeed, the CPV predicted by the SM is not sufficient to explain the observed matter-antimatter asymmetry in the Universe. The *CP* operator combines the charge conjugation C with the parity reverse P. Under the C transformation, all intrinsic quantum numbers are inverted, therefore particles and anti-particles are interchanged. Under P, the spatial coordinates are inverted, therefore the handedness is reversed, $\vec{x} \to -\vec{x}$. Hence, under *CP*, both C and P transformations are applied. The effect, for example, is that a left-handed electron, e_L^-, is transformed under *CP* into a right-handed positron, e_R^+ [11]. The SM Lagrangian is consistent with the gauge symmetry group G_{SM} of Eq. 1.1 and can be divided in three terms

$$\mathcal{L}_{SM} = \mathcal{L}_{kin} + \mathcal{L}_{Higgs} + \mathcal{L}_{Yukawa}. \tag{1.7}$$

The kinetic part, $\mathcal{L}_{kin}$, is the sum of all kinetic terms ($i\overline{\psi}\gamma^\mu\partial_\mu\psi$) of fermions. In order to maintain the gauge invariance, the standard derivative is replaced by a covariant derivative:

$$D^\mu = \partial^\mu + ig_s G_a^\mu L_a + igW_b^\mu T_b + ig' B^\mu Y, \tag{1.8}$$

where

- L_a are the $SU(3)_C$ group generators: $\frac{1}{2}\lambda_a$ for triplets (λ_a are the eight 3×3 Gell-Mann matrices) and 0 for singlets. G_a^μ are the eight gluon fields;
- T_b are the $SU(2)_L$ group generators: $\frac{1}{2}\sigma_b$ for doublets (σ_b are the three 2×2 Pauli matrices) and 0 for singlets. W_b^μ are the three weak interaction bosons;
- Y are the $U(1)_Y$ charges and B^μ is the single hypercharge boson.

The Higgs potential, $\mathcal{L}_{Higgs}$, describes the scalar self interaction of the Higgs field and reads

$$\mathcal{L}_{Higgs} = \mu^2\phi^\dagger\phi + \lambda(\phi^\dagger\phi)^2, \tag{1.9}$$

where λ is the self coupling constant and $\mu^2 = -v^2\lambda$. If μ^2 is negative there is an infinite set of VEV different from zero ($v \neq 0$). Both $\mathcal{L}_{kin}$ and $\mathcal{L}_{Higgs}$ are *CP* symmetric in the SM. **The Yukawa term**, $\mathcal{L}_{\mathbf{Yukawa}}$, describes the coupling between fermions and the scalar field. In general, this part of the Lagrangian is *CP* violating. This is the only source of *CP* violation predicted by the SM. The $\mathcal{L}_{Yukawa}$ term reads

$$\mathcal{L}_{Yukawa} = -Y_{ij}^d\overline{Q_{Li}^I}\phi d_{Rj}^I - Y_{ij}^u\overline{Q_{Li}^I}\overline{\phi}u_{Rj}^I - Y_{ij}^\ell\overline{L_{Li}^I}\phi\ell_{Rj}^I + \text{h.c.}, \tag{1.10}$$

where $Y_{ij}^{u,d,\ell}$ are 3×3 complex matrices, $i, j = 1, 2, 3$ are the generation indexes and $\overline{\phi} = i\sigma^2\phi^\dagger$. The fermion mass term arises when ϕ acquires a vacuum expectation value, v (see Eq. 1.4). By replacing Eq. 1.6 in Eq. 1.10 and neglecting the interaction term, one can write the mass term

$$\mathcal{L}_M = -(M_d)_{ij}\overline{d_{Li}^I}d_{Rj}^I - (M_u)_{ij}\overline{u_{Li}^I}u_{Rj}^I - (M_\ell)_{ij}\overline{\ell_{Li}^I}\ell_{Rj}^I, \tag{1.11}$$

where $M_{d,u,\ell} = \frac{v}{\sqrt{2}}Y_{d,u,\ell}$. It is possible to find the physical observed states, by diagonalizing $M_{d,u,\ell}$

$$V_{fL}M_f V_{fR}^\dagger = M_f^{diag} \qquad f = d, u, \ell \tag{1.12}$$

where V_{fL} and V_{fR} are unitary matrices and M_f^{diag} is diagonal and real. Then the mass eigenstates are identified as

$$d_{Li} = (V_{dL})_{ij} d^I_{Lj}, \quad d_{Ri} = (V_{dR})_{ij} d^I_{Rj}, \tag{1.13}$$
$$u_{Li} = (V_{uL})_{ij} u^I_{Lj}, \quad u_{Ri} = (V_{uR})_{ij} u^I_{Rj} \tag{1.14}$$
$$\ell_{Li} = (V_{\ell L})_{ij} \ell^I_{Lj}, \quad \ell_{Ri} = (V_{\ell R})_{ij} \ell^I_{Rj} \tag{1.15}$$
$$\nu_{Li} = (V_{\nu L})_{ij} \nu^I_{Lj}. \tag{1.16}$$

The Cabibbo–Kobayashi–Maskawa matrix

Within the SM, the *CP* symmetry in preserved in strong and electromagnetic interactions, but violated in weak interactions. In the SM Lagrangian the *CP* symmetry is broken by an irreducible complex physical phase in the Yukawa quark-term. Let's now take, from the $\mathcal{L}_{kin}$ term, the charge current interaction between the quarks and charged $SU(2)_L$ gauge bosons, $W^{\pm}_{\mu} = \frac{1}{\sqrt{2}}(W^1_{\mu} \mp W^2_{\mu})$, expressed as functions of the weak interaction eigenstates

$$\mathcal{L}_{W^{\pm}} = \frac{-g}{\sqrt{2}} \overline{Q^I_{Li}} \gamma^{\mu} W^+_{\mu} Q^I_{Li} + \text{h.c.}. \tag{1.17}$$

Only left-handed quarks are present because the charged weak bosons $W^{\pm}$ preserve the $SU(2)_L$ symmetry (unlike the Z^0 boson) and couple only with left-handed particles. Expressing it as a fuction of the mass eigenstates (Eq. 1.16), the $\mathcal{L}_{W^{\pm}}$ becomes

$$\mathcal{L}_{W^{\pm}} = \frac{-g}{\sqrt{2}} \overline{u_{Li}} V_{uL} \gamma^{\mu} W^+_{\mu} V^{\dagger}_{dL} d^I_{Li} + \text{h.c.}, \tag{1.18}$$

where u_i stands for the up type quarks (u, c, t) and d_i stands for the down type, (d, s, b). Therefore, one can write:

$$\mathcal{L}_{W^{\pm}} = \frac{-g}{\sqrt{2}} (\overline{u_L}, \overline{c_L}, \overline{t_L}) \gamma^{\mu} W^+_{\mu} V_{CKM} \begin{pmatrix} d_L \\ s_L \\ b_L \end{pmatrix} + \text{h.c.}.$$

The V_{CKM} is the product between the unitary matrices V_{uL} and $V^{\dagger}_{dL}$, hence it is a 3×3 unitary matrix, known as the Cabibbo-Kobayashi-Maskawa (CKM) matrix [1, 2]:

$$V_{CKM} \equiv V_{uL} V^{\dagger}_{dL} = \begin{pmatrix} V_{ud} & V_{us} & V_{ub} \\ V_{cd} & V_{cs} & V_{cb} \\ V_{td} & V_{ts} & V_{tb} \end{pmatrix}.$$

The CKM matrix can be parameterized by three mixing angles and a complex phase, as reported below

$$V_{CKM} = \begin{pmatrix} c_{12}c_{13} & s_{12}c_{13} & s_{13}e^{-i\delta} \\ -s_{12}c_{23} - c_{12}s_{23}s_{13}e^{-i\delta} & c_{12}c_{23} - s_{12}s_{23}s_{13}e^{i\delta} & s_{23}c_{13} \\ s_{12}s_{23} - c_{12}c_{23}s_{13}e^{i\delta} & -c_{12}s_{23} - s_{12}c_{23}s_{13}e^{i\delta} & c_{23}c_{13} \end{pmatrix},$$

where $s_{ij} = \sin\theta_{ij}$, $c_{ij} = \cos\theta_{ij}$ and δ is the phase, above mentioned, responsible for all *CP*-violating phenomena in flavour-changing processes in the SM[1]. It is known experimentally that $s_{13} \ll s_{23} \ll s_{12} \ll 1$, therefore it is convenient to use the Wolfenstein parametrization that instead of the parameters $(s_{12}, s_{23}, s_{13}, \delta)$ uses four new parameters $(\lambda, A, \overline{\rho}, \overline{\eta})$:

$$s_{12} = \lambda = \frac{|V_{us}|}{\sqrt{|V_{ud}|^2 + |V_{us}|^2}}, \quad s_{23} = A\lambda^2 = \lambda \left|\frac{V_{cb}}{V_{us}}\right|, \tag{1.19}$$

$$s_{13}e^{i\delta} = V_{ub}^* = A\lambda^3(\rho + i\eta) = \frac{A\lambda^3(\overline{\rho} + i\overline{\eta})\sqrt{1 - A^2\lambda^4}}{\sqrt{1-\lambda^2}[1 - A^2\lambda^4(\overline{\rho} + i\overline{\eta})]}, \tag{1.20}$$

where $\overline{\rho} = \rho(1 - \lambda^2/2 + \dots)$ and $\overline{\eta} = \eta(1 - \lambda^2/2 + \dots)$. One can write V_{CKM} to $\mathcal{O}(\lambda^4)$:

$$V_{CKM} \begin{pmatrix} 1-\lambda^2/2 & \lambda & A\lambda^3(\rho - i\eta) \\ -\lambda & 1-\lambda^2/2 & A\lambda^2 \\ A\lambda^3(1-\rho-i\eta) & -A\lambda^2 & 1 \end{pmatrix} + \mathcal{O}(\lambda^4). \tag{1.21}$$

The unitarity of the CKM matrix imposes

$$\sum_i V_{ij}V_{ik}^* = \delta_{jk}, \quad \sum_j V_{ij}V_{kj}^* = \delta_{ik}, \tag{1.22}$$

hence, the orthogonality among rows and columns. This six constraints are represented as triangles in a complex $(\overline{\rho} - \overline{\eta})$ plane, all having the same area. These are known as *unitarity triangles*. The most common one comes from the $V_{ud}V_{ub}^* + V_{cd}V_{db}^* + V_{td}V_{tb}^* = 0$ condition. Dividing each term by $V_{cd}V_{cb}^*$ (the best experimentally known term), one obtain that the vertices of the unitary triangle are exactly (0,0), (1,0) and $(\overline{\rho}, \overline{\eta})$, from the definitions in Eq. 1.19. The triangle is shown in Fig. 1.1. The area of the unitarity triangles

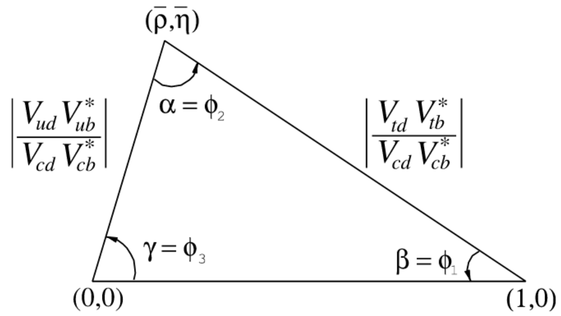

Figure 1.1: *Unitarity triangle in $(\overline{\rho}, \overline{\eta})$ plane.*

is equal to half of the Jarlskog invariant[12], J, that is a measure of CPV independent from the choice of the phase convention. It is defined as follows:

$$Im[V_{ij}V_{kl}V_{il}^*V_{kj}^*] = J \sum_{m,n \in (d,s,b)} \epsilon_{ikm}\epsilon_{jln} \tag{1.23}$$

and approximated by $J \approx \lambda^6 A^2 \eta$ in the Wolfenstein parametrization.

The CKM matrix elements are fundamental parameters of the SM, their precise determination is important to make predictions and to put strong constraints on beyond Standard Model theories. Most of the CKM matrix elements are determined through direct measurements, looking at tree level processes. In this way, it is possible to directly extract the value of $|V_{ij}|$. However, some elements have low precision, such as $|V_{tb}|$ and $|V_{cs}|$, or are too suppressed to be measured, such as $|V_{td}|$ and $|V_{ts}|$. In these cases, the indirect measurements are performed looking at higher-order process. It is useful to display the various measurements and compare them in the $\overline{\rho}, \overline{\eta}$ plane, as in Fig. 1.2. The shaded 99% CL regions all overlap consistently around the global fit region. Combining both the direct and indirect measurements of the CKM elements and imposing the unitarity constraints in Eq. 1.22, one can over-constraint the parameters, reducing the allowed range of possible value. The fit for the Wolfenstein parameters gives[11]:

$$\lambda = 0.22650 \pm 0.00048, \quad A = 0.790^{+0.017}_{-0.012}, \tag{1.24}$$

$$\overline{\rho} = 0.141^{+0.016}_{-0.017}, \quad \overline{\eta} = 0.356 \pm 0.011. \tag{1.25}$$

Whereas, the fit result for the magnitudes of all nine CKM elements are[11]

$$V_{CKM} = \begin{pmatrix} 0.97401 \pm 0.00011 & 0.22650 \pm 0.00048 & 0.00361^{+0.00011}_{-0.00009} \\ 0.22636 \pm 0.00048 & 0.97320 \pm 0.00011 & 0.04053^{+0.00083}_{-0.00061} \\ 0.00854^{+0.00032}_{-0.00016} & 0.03978^{+0.00082}_{-0.00060} & 0.999172^{+0.000024}_{-0.000035} \end{pmatrix}, \tag{1.26}$$

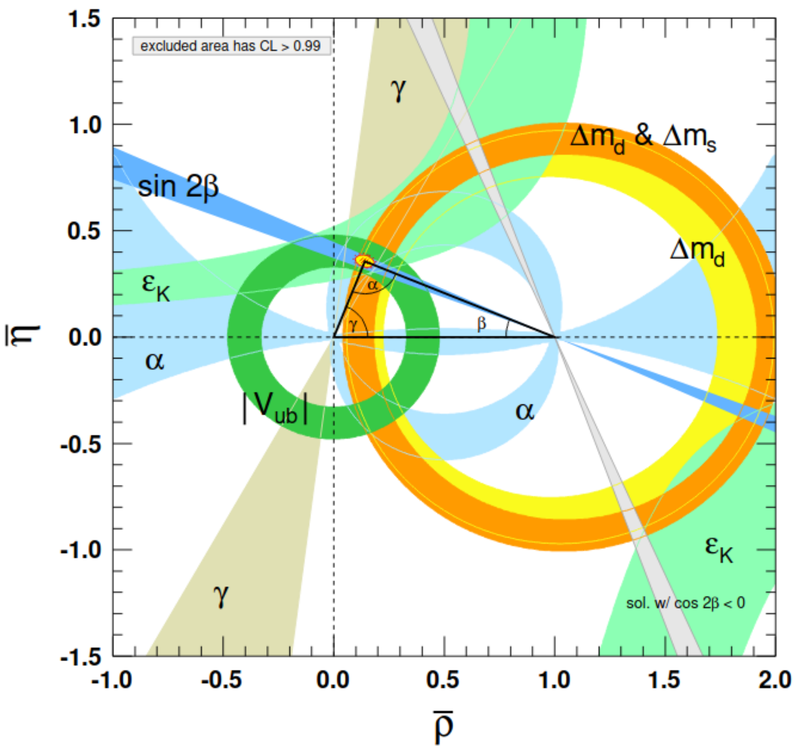

Figure 1.2: *Current experimental status of the global fit to all available experimental measurements related to the unitarity triangle phenomenology [11]. The shaded areas have 99% CL contours.*

1.3 Type of *CP* violation

The *CP* transformation for a *CP*-eigenstate f is $\mathrm{CP}|f\rangle = \omega_f |f\rangle$ and for the antiparticle $CP|\overline{f}\rangle = \omega_f^* |\overline{f}\rangle$, where ω_f is a complex phase ($|\omega_f| = 1$). Experimentally, there are three different manifestations of *CP* violation [13]:

- CPV in the decay;
- CPV in the mixing;
- CPV in the interference between decay and mixing.

The *CP* violation in the decay is also called *direct CPV*, whereas the other two types are called *indirect CPV*.

CPV in the decay

Let's define the decay amplitude of a generic (charged or neutral) particle P into a final state f

$$\mathcal{A}(P \to f) := \langle f|\mathcal{H}|P\rangle \tag{1.27}$$

$$\mathcal{A}(\overline{P} \to \overline{f}) := \langle \overline{f}|\mathcal{H}|\overline{P}\rangle, \tag{1.28}$$

where $\mathcal{H}$ is the decay Hamiltonian, and where Eq. 1.28 displays the decay amplitude related to the antiparticle $\overline{P}$ which decays to the C-conjugated final state $\overline{f}$. The CPV in the decay is observed if $\mathcal{A}(P \to f) \neq \mathcal{A}(\overline{P} \to \overline{f})$. These two decay amplitudes can be written considering a decay process which can proceed through several decay amplitudes

$$\mathcal{A}(P \to f) = \sum_i |a_i| \exp\{i(\phi_i + \delta_i)\}, \quad \mathcal{A}(\overline{P} \to \overline{f}) = \sum_i |a_i| \exp\{i(-\phi_i + \delta_i)\}, \tag{1.29}$$

where

- ϕ_i denotes the weak phases, originating from the weak interaction through the CKM matrix phase. They change sign under CP transformation;
- δ_i refers to the strong phases, due to the final state interaction. As the name suggests, they are generated by the strong interaction (whenever there are hadrons) and do not change sign under *CP* transformation.

A golden observable, sensitive to the *CP* violation in the decay, is the *CP* asymmetry

$$A_{CP}^{dir}(f) = \frac{\Gamma(P \to f) - \Gamma(\overline{P} \to \overline{f})}{\Gamma(P \to f) + \Gamma(\overline{P} \to \overline{f})} \tag{1.30}$$

where Γ is the time-integrated decay width: $\Gamma(P \to f) \propto |\mathcal{A}(P \to f)|^2$ and $\Gamma(\overline{P} \to \overline{f}) \propto |\mathcal{A}(\overline{P} \to \overline{f})|^2$, thus

$$A_{CP}^{dir}(f) = \frac{|\mathcal{A}(P \to f)|^2 - |\mathcal{A}(\overline{P} \to \overline{f})|^2}{|\mathcal{A}(P \to f)|^2 + |\mathcal{A}(\overline{P} \to \overline{f})|^2} \tag{1.31}$$

where the difference appearing in the numerator becomes:

$$|\mathcal{A}(P \to f)|^2 - |\mathcal{A}(\overline{P} \to \overline{f})|^2 = -2\sum_{i,j} |a_i||a_j| \sin(\phi_i - \phi_j) \sin(\delta_i - \delta_j). \tag{1.32}$$

It follows that, in order to generate an 'observable' direct-*CP* asymmetry, three different conditions are necessary [14]:

- the presence of at least two interfering amplitudes;

- two different weak phases ($\sin(\phi_i - \phi_j) \neq 0$);
- two different strong phases ($\sin(\delta_i - \delta_j) \neq 0$).

Another way to re-write the CP asymmetry is the following:

$$A_{CP}^{dir} = \frac{1 - R_f^2}{1 + R_f^2}, \quad R_f = \left| \frac{\mathcal{A}(P \to f)}{\mathcal{A}(\overline{P} \to \overline{f})} \right|, \tag{1.33}$$

Therefore, the CP violation in the decay occurs if $R_f \neq 1$.

CPV in the mixing

Within the Standard Model, the neutral mesons are defined as *flavoured* if they posses a non-null flavour quantum number (strangeness, charmness or bottomness), such as $K^0(d\bar{s})$, $D^0(c\bar{u})$, $B^0(d\bar{b})$. These mesons cannot decay into lighter particles through a strong or electromagnetic interaction. The interaction eigenstate (or flavour eigenstate) in which they are produced is different from the mass one, as seen in the previous sections. The mass eigentate is related to the free Hamiltonian, that drives the time evolution of the particle. Thus, it is possible for a flavoured meson to be produced with a certain flavour and then to oscillate into its antiparticle. This process is called *mixing*. In general the state of a meson can be expressed as a linear combination of the flavour eigenstate [15]:

$$|\psi(0)\rangle = a(0)|M^0\rangle + b(0)|\overline{M}^0\rangle, \tag{1.34}$$

where M^0 and $\overline{M}^0$ are the flavour eigenstates. The Schrodinger equation that describes the state time evolution reads

$$i\hbar\frac{\partial}{\partial t}|\psi\rangle = H_M|\psi(t)\rangle, \quad |\psi(t)\rangle = a(t)|M^0\rangle + b(t)|\overline{M}^0\rangle + \sum_k c_k(t)|f_k\rangle, \tag{1.35}$$

where H_M is the free Hamiltonian and $|f_k\rangle$ are all the possible final state in which the two mesons can decay. For the purpose of mixing, it is usefull to apply the Weisskopf-Wigner approximation[16, 11], in order to neglect the flavour-conserving strong and electromagnetic interactions. In fact, the aim is to find $a(t)$ and $b(t)$ (not the values of all $c_k(t)$). Moreover the time t that is considered is much larger than the typical strong interaction scale. Therefore, the simplified time evolution is determined by a 2×2 effective Hamiltonian $\boldsymbol{\mathcal{H}}$ that can be written in terms of the Hermitian matrices M and Γ:

$$\boldsymbol{\mathcal{H}} = \mathbf{M} - \frac{i}{2}\boldsymbol{\Gamma}. \tag{1.36}$$

The diagonal elements of the mass matrix M and the decay matrix Γ are associated with flavour-conserving transitions, whereas the non-diagonal elements are associated with flavour-changing transitions. The matrix elements of M and Γ satisfy $M_{11} = M_{22}$ and $\Gamma_{11} = \Gamma_{22}$, in order to obey the CPT invariance. It is now possible to define the $\boldsymbol{\mathcal{H}}$ eigenstates, $|M_{1,2}\rangle$, as

$$|M_{1,2}\rangle = p|M^0\rangle \pm q|\overline{M}^0\rangle, \tag{1.37}$$

where p and q are complex coefficients satisfying

$$|p|^2 + |q|^2 = 1, \quad \frac{q}{p} = \pm\sqrt{\frac{M_{12}^* - (i/2)\Gamma_{12}^*}{M_{12} - (i/2)\Gamma_{12}^*}}. \tag{1.38}$$

The eigenvalues of $\boldsymbol{\mathcal{H}}$ are

$$\lambda_{1,2} = m_{1,2} - \frac{1}{2}\Gamma_{1,2} = M - \frac{i}{2}\Gamma \pm \frac{q}{p}\big(M_{12} - \frac{i}{2}\Gamma_{12}\big), \tag{1.39}$$

thus

$$|M_{1,2}(t)\rangle = \exp\{-im_{1,2}t\}\exp\{-\Gamma_{1,2} - \frac{i}{2}\Gamma_{1,2}\}|M_{1,2}(0)\rangle. \tag{1.40}$$

Substituting Eq. 1.40 inside Eq. 1.37, one can find the time evolution of a particle that was created in its flavour eigenstate at $t = 0$:

$$|M^0(t)\rangle = f_+(t)|M^0\rangle + \frac{q}{p}f_-(t)|\overline{M}^0\rangle \tag{1.41}$$

$$|\overline{M}^0(t)\rangle = f_+(t)|\overline{M}^0\rangle + \frac{q}{p}f_-(t)|M^0\rangle, \tag{1.42}$$

with

$$f_\pm = \frac{1}{2}\exp\{-im_1\}\exp\{-\Gamma_1 t/2\}\big(1 + \exp\{-i\Delta m t\}\exp\{\Delta\Gamma t/2\}\big), \tag{1.43}$$

being $\Delta m = m_2 - m_1$ and $\Delta\Gamma = \Gamma_2 - \Gamma_1$. It follows that the probability of transition is given by

$$\mathcal{P}(M^0 \to M^0(t)) = |\langle M^0(t)|M^0\rangle|^2 = |f_+(t)|^2, \tag{1.44}$$

$$\mathcal{P}(\overline{M}^0 \to \overline{M}^0(t)) = |\langle \overline{M}^0(t)|\overline{M}^0\rangle|^2 = |f_+(t)|^2, \tag{1.45}$$

$$\mathcal{P}(M^0 \to \overline{M}^0(t)) = |\langle M^0(t)|\overline{M}^0\rangle|^2 = \left|\frac{q}{p}\right|^2 \cdot |f_-(t)|^2, \tag{1.46}$$

$$\mathcal{P}(\overline{M}^0 \to M^0(t)) = |\langle \overline{M}^0(t)|M^0\rangle|^2 = \left|\frac{p}{q}\right|^2 \cdot |f_-(t)|^2 \tag{1.47}$$

The *CP* violation in the mixing occurs if $\mathcal{P}(M^0 \to \overline{M}^0(t)) \neq \mathcal{P}(\overline{M}^0 \to M^0(t))$. Hence, from Eqs. 1.46 and 1.47 follows that it is possible only if the magnitude of the ratio between q and p differs from 1:

$$R_m := \left|\frac{q}{p}\right| \neq 1. \tag{1.48}$$

CPV in the interference

The *CP* symmetry can be violated in the interference between the decay without mixing, $M^0 \to f$ but also with the mixing, $M^0 \to \overline{M}^0 \to f$. The latter occurs when

$$Im(\lambda_f) + Im(\lambda_{\overline{f}}) \neq 0 \tag{1.49}$$

where

$$\lambda_f = \frac{q}{p}\frac{\mathcal{A}(\overline{M}^0 \to f)}{\mathcal{A}(M^0 \to f)} \quad \text{and} \quad \lambda_{\overline{f}} = \frac{q}{p}\frac{\mathcal{A}(\overline{M}^0 \to \overline{f})}{\mathcal{A}(M^0 \to \overline{f})}. \tag{1.50}$$

For final *CP* eigenstates, the condition of Eq. 1.49 simplifies to

$$Im(\lambda_f) \neq 0.$$

In this case, λ_f is usually written as

$$\lambda_f = -\eta_C P(f) R_m R_f e^{i\phi_f}, \tag{1.51}$$

where $\eta_{CP}(f)$ is the *CP*-parity of the final state f and

$$\phi_f := arg\left(-\eta_{CP}(f)\cdot\frac{q\mathcal{A}(\overline{M}^0\to f)}{p\mathcal{A}(M^0\to f)}\right). \tag{1.52}$$

The CPV condition for having CPV in the interference is expressed by $\phi \neq \{0,\pi\}$.

1.4 CPV in the charm sector

The existence of a fourth quark was theoretically discussed by Bjorken and Glashow in 1964 [17], who named it the charm quark. Ten years have passed before having a proof of its existence: the first $c\bar{c}$ bound state was discovered in 1974, by two independent research groups at SLAC and Brookhaven Laboratory [18, 19], it was called J/ψ. The charm quark belongs to the second generation of quarks, together with the strange one. It has a bare mass of about 1.3 GeV$/c^2$ and an electric charge of $+2/3$ as the other up-type quarks (up and top). It is never observed free, but only in bounded states with other quarks/anti-quarks. Charmed hadrons can contain a charm quark together with one (mesons) or more (baryons) different quarks. As said before, the only way to decay for a charm quark is through a weak interaction mediated by the charge $W^{\pm}$ boson, because according to the Standard Model, the strong and electromagnetic interactions preserve the flavour. Charmed mesons and baryon decays are the only ways to study the decay of an up-type quark to a down-type quark (strange or down) in a bounded state. In fact, the up quark is the lightest one, hence it is stable, while the top quark decays before interacting, *i.e.* it decays faster than the hadronization time scale. Studying the charmed mesons decays, the interesting elements of the CKM matrix are those in the first two rows, because the charm quark can decay only into lighter quarks. Therefore, the relevant unitarity relationship for charm mesons is

$$V_{cd}^* V_{ud} + V_{cs}^* V_{us} + V_{cb}^* V_{ub} = 0, \tag{1.53}$$

that can be written in a more compact way:

$$\Lambda_d + \Lambda_s + \Lambda_b = 0, \quad \Lambda_q = V_{cq}^* V_{uq} (q \in d, s, b). \tag{1.54}$$

Developing each term in the Wolfenstein parametrization, the result is a mashed triangle with a side of the order of λ^5, as shown in Fig. 1.3. The CPV in the charm decay was recently discovered studying the decays $D^0 \to K^+K^-$ and $D^0 \to \pi^+\pi^-$. It is found to be $\Delta A_{CP} = (-15.4 \pm 2.9) \times 10^{-4}$ [3], with the uncertainty including both statistical and systematic contributions. This result is in accordance with the SM predictions, close to the upper bound of the theory uncertainties. Further studies, both from theoretical and experimental point of view are, therefore, necessary to understand the nature of this *CP*-violating signal in the charm quark sector. The discovery of new sources of CPV would be of fundamental importance for the field, since the amount produced through the CKM mechanism is too tiny to explain the cosmological baryonic asymmetry observed in our universe.

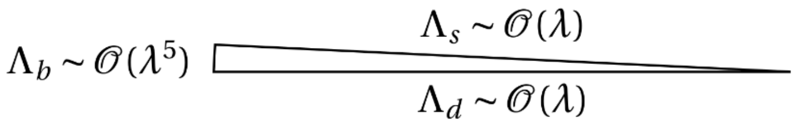

Figure 1.3: *Sketch of the charm unitarity triangle.*

1.5 Charm production

The charm physics is currently performed in two main ways: through e^+e^- and pp collisions. These different colliders come with different production mechanisms and thus with largely varying production cross-sections [15].

$\mathbf{e^+e^-}$ colliders Since e^+e^- is a puntual interaction, the environment is clean, with known interaction energy and few interaction vertices per event. Therefore, the background is very low and the detection efficiency is very high. In this kind of colliders two different running conditions are of interest for the charm physics:

- **D-factories:** The centre-of-mass energy is slightly over 3770 MeV: it resonantly produces $\Psi(3770)$ mesons which decay almost exclusively in quantum correlated $D^0\overline{D}^0$ or D^+D^- pairs. The $D^0\overline{D}^0$ production cross-section through the $\Psi(3770)$ resonance is approximately 8 nb. This production mode has been used for the CLEO-c experiment (CESR-c collider, Ithaca, New York) as well as for BESIII (BEPCII, Beijing, China).

- **B-factories:** The centre-of-mass energy is chosen to produce Υ(4S) resonance: it decays into quantum-correlated $B^0\overline{B}^0$ or B^+B^- pairs which decay into all possible charm particles and not only D^0 $\overline{D}^0$ pairs. The cross section for producing at least one D^0 is 1.3 nb. BaBar(PEP-II collider, SLAC, California) and Belle (KEKB collider, KEK, Japan) experiments are B-factories which have overcame the issue of the small cross section by integrating an higher luminosity: about 500 fb^{-1} and 1000 fb^{-1}, respectively.

Hadron colliders At hadron colliders the $c\bar{c}$ production cross-section is several order of magnitude higher with respect to the one at e^+e^- colliders. For proton anti-proton collisions ($p\overline{p}$) at the Tevatron accelerator at $\sqrt{s} = 1.96$ TeV, the CDF experiment measured a D^0 production cross section of 13 μb, inside the detector acceptance [20], and collected about 10 fb^{-1} of integrated luminosity in ten years of operation. For what concerns the pp collisions at the LHC with a centre-of-mass energy of 13 TeV, it has been measured a cross-section of about 2.7 mb for producing D^0 within the LHCb acceptance[1][21]. The collected data are written in Tab. 1.1, where one can see that thanks to the high $c\bar{c}$ cross section at hadron colliders, LHCb has collected the highest amount of charmed data.

[1]In a range of $p_T < 8$ GeV/c and rapidity $2.0 < y < 4.5$

Experiment	Year	Beam	$\sqrt{s}$	$\sigma_{acc}(D^0)$	$\int \mathcal{L}$	$\sim n(D^0)$
BaBar	1999-2008	e^+e^-	10.6 GeV	1.45 nb	500 fb^{-1}	7.3×10^8
Belle	1999-2010	e^+e^-	10.6-10.9 GeV	1.45 nb	1000 fb^{-1}	1.5×10^9
CDF	2001-2011	$p\overline{p}$	2 TeV	13 μb	10 fb^{-1}	1.3×10^{11}
LHCb Run1	2011-2012	pp	7-8 TeV	1.4-1.6 mb	1+ 2 fb^{-1}	4.6×10^{12}
LHCb Run2	2015-2018	pp	13 TeV	2.7 mb [21]	5.9 fb^{-1}	1.6×10^{13}

Table 1.1: *D^0 meson production values for different experiments inside the respective detector acceptances, as defined in the text.*

1.6 Flavour tagging

The measurement of the CP asymmetry usually requires the knowledge of the flavour at production (t = 0) of the decaying particles. In the present case, it is possible to distinguish a D^0 meson from an $\overline{D^0}$, this process is called *tagging* by the experimentalists. It can be done by exploiting the following production channels of the neutral D mesons:

- $D^{*+} \to D^0\pi^+$ and $D^{*-} \to \overline{D}^0\pi^-$
- $\overline{B} \to D^0\mu^-\overline{\nu}_\mu X$ and $B \to \overline{D}^0\mu^+\nu_\mu X$.

In the D^* **tagging**, the D^0 flavour is inferred from the sign of the charge of the pion. The pion from the $D^{*\pm}$ decay has little kinetic energy, for this reason it is commonly referred to *soft* pion (π_s). In the **semileptonic tagging**, $\overline{B}$ (B) stands for a generic beauty hadron (containing b or $\overline{b}$) quark, whereas X for all the additional particles that might be produced in the decay. The D^0 flavour is determined by the sign of the charge of the muon. This can be a good choice thanks to the high trigger efficiency for muons. However, since the production cross section of $c\overline{c}$ pairs is much larger than the $b\overline{b}$ at hadron colliders, most of the measurements have been performed using the first tagging technique. At the B-factories, the production cross sections become comparable but it is still true that the first decay chain is favoured as its branching fraction is larger[2] than the second one by a factor of 10.

The subject of this thesis is focused on searching for CPV in the charm quark sector, by means the study of the promising discovery channels $D^0 \to \overline{K}^{*0}K^0$ and $D^0 \to K^{*0}\overline{K}^0$, that can be experimentally accessed through the analysis of the laboratory decay channels $D^0 \to K^0_sK^\pm\pi^\mp$. Therefore, the next chapter is specifically dedicated to the description of the current state-of-the-art of these decay channels. In addition, the general analysis strategy, developed in this thesis work, is illustrated in order to perform a precise measurement of the *CP*-violating asymmetry using the current available LHCb Run 2 data sample.

[2] $\mathcal{B}(D^{*+} \to D^0\pi^+) = (67.7 \pm 0.5)\%$, whereas $\mathcal{B}(\overline{B}_{mix} \to D^0\mu^-\overline{\nu}_\mu X) = (6.79 \pm 0.34)\%$, $\overline{B}_{mix}$ stands for the admixture of bottom particles ($B^\pm/B^0/B^0_s/b - baryon$) at high energy colliders, such as LHC[11]

2

Neutral $D^0 \to KK^*$ decays as discovery channels

This chapter describes the theoretical framework of the $D^0 \to \overline{K}^{*0}K^0$ and $D^0 \to K^{*0}\overline{K}^0$ decays, inclusively referred as $D^0 \to KK^*$. They are potential promising discovery channels for charm CP violation in the Standard Model, as described in detail in Ref. [9]. They can be experimentally accessed through the analysis of the laboratory decay channels $D^0 \to K^0_s K^\pm \pi^\mp$, therefore the current experimental state-of-the-art for these decays is presented, along with a short overview of the new experimental analysis methodology developed with this work.

2.1 $D^0 \to KK^*$ as promising discovery channels

In the charm sector, a theoretical description of the underlying mechanism for exclusive hadronic D decays based on QCD is still not available. In fact, the mass of the charm quark is too light to allow for a heavy quark expansion. Therefore, there is not a reliable model which allows to estimate the phases and magnitudes of the decay amplitudes. For this reason, the *diagrammatic approach* is used. It is based on flavour $SU(3)$ symmetry and provides a model-independent analysis of the charmed meson decays, that allows to extract the topological amplitudes. Therefore, the flavour-flow diagrams are classified purely according to the topologies of the weak interactions with all the strong interaction effects included [22]. The classification is divided in two main groups of amplitudes.

- *Tree and penguin annihilation*: including the color-allowed (T) and color-suppressed (C) tree amplitudes, with an external and internal W-emission respectively, see Fig. 2.1, (a) and (b). Moreover, it includes the QCD-penguin amplitude (P): the color-favored (P_{EW}) and the color-suppressed (P^C_{EW}) electro-weak penguin amplitudes, Fig. 2.1, (c) and (d). Finally, there are the singlet QCD-penguin (S) amplitudes that involves SU(3)-singlet mesons like η, ω and ϕ, Fig. 2.1, (d).

- *Weak annihilation*: including W-exchange (E) and W-annihilation (A) amplitudes, Fig. 2.1, (e) and (f). The QCD- and electro-weak (EW-) penguin exchange (PE, PE_{EW}), the respective annihilation amplitudes (PA, PA_{EW}), are shown in Fig. 2.1, (g) and (h).

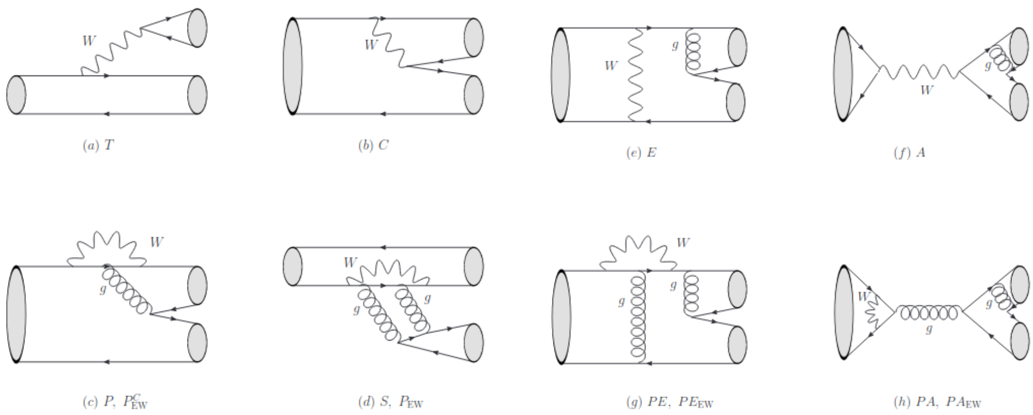

Figure 2.1: *Topological diagrams, from Ref [22].*

Another important classification of the charmed hadronic decays comes according to the degree of CKM matrix element suppression:

1. Cabibbo-Favoured decays (CF): the amplitude is proportional to the product $V_{ud}V_{cs}^*$.
2. Singly Cabibbo-Suppressed decays (SCS): the amplitude is proportional to the product $V_{uq}V_{cq}^*$ where $q = s, d, b;$.
3. Doubly Cabibbo-Suppressed decays $V_{us}V_{cd}^*$.

The $D^0 \to \overline{K}^{*0}K^0$ and $D^0 \to K^{*0}\overline{K}^0$ decays[1], inclusively referred as $D^0 \to KK^*$ decays throughout the text, belongs to the SCS decays category. Using the relation in Eq. 1.54, one can write the decomposition of some decay amplitudes, $\mathcal{A}(d)$, in term of CKM matrix elements, as described in Ref. [9]:

$$\mathcal{A}(d) \equiv \Lambda_{sd}\mathcal{A}_{sd}(d) - \frac{\Lambda_b}{2}\mathcal{A}_b(d), \tag{2.1}$$

where $\Lambda_{sd} = \frac{\Lambda_s - \Lambda_d}{2}$. At first order in $|\Lambda_b|/|(\Lambda_s - \Lambda_d)|$ the direct CP asymmetry reads

$$A_{CP}^{dir}(d) \equiv \frac{|\mathcal{A}(d)|^2 - |\overline{\mathcal{A}}(d)|^2}{|\mathcal{A}(d)|^2 + |\overline{\mathcal{A}}(d)|^2} \tag{2.2}$$

$$\equiv Im\frac{\Lambda_b}{\Lambda_{sd}} Im\frac{\mathcal{A}_b(d)}{\mathcal{A}_{sd(d)}}. \tag{2.3}$$

$\mathcal{A}_{sd}(d)$ and $\mathcal{A}_b(d)$ can be written as the sum of topological amplitudes. In the decay channels subject of study: $D^0 \to \overline{K}^{*0}K^0$ and $D^0 \to K^{*0}\overline{K}^0$, the topological decomposition of

$$\mathcal{A}_{sd}(K^{*0}) := \mathcal{A}_{sd}(D^0 \to K^{*0}\overline{K}^0) \tag{2.4}$$

$$\mathcal{A}_{sd}(\overline{K}^{*0}) := \mathcal{A}_{sd}(D^0 \to \overline{K}^{*0}K^0) \tag{2.5}$$

$$\mathcal{A}_b(K^{*0}) := \mathcal{A}_b(D^0 \to K^{*0}\overline{K}^0) \tag{2.6}$$

$$\mathcal{A}_b(\overline{K}^{*0}) := \mathcal{A}_b(D^0 \to \overline{K}^{*0}K^0) \tag{2.7}$$

[1] The inclusion of the charge conjugate decays is implied.

depends on exchange and penguin annihilation topologies [9]:

$$\mathcal{A}_{sd}(K^{*0}) = E_P - E_V + E_{P3} - E_{V1} - E_{V2} - PA_{PV}^{break}, \tag{2.8}$$
$$\mathcal{A}_{b}(K^{*0}) = -E_P - E_V - E_{P3} - E_{V1} - E_{V2} - PA_{PV}, \tag{2.9}$$
$$\mathcal{A}_{sd}(\overline{K}^{*0}) = -E_P + E_V - E_{P1} - E_{P2} + E_{V3} - PA_{PV}^{break}, \tag{2.10}$$
$$\mathcal{A}_{b}(\overline{K}^{*0}) = -E_P - E_V - E_{P1} - E_{P2} - E_{V3} - PA_{PV}, \tag{2.11}$$

where the subscripts P and V stands for the pseudo-scalar $K^0, \overline{K}^0$ and the vectorial $K^{*0}, \overline{K}^{*0}$ respectively. The corresponding topological diagram are shown in Fig. 2.2. The exchange diagrams corresponding to E_P and E_V are the pictures (a) and (b) respectively. Whereas, the pictures (c) and (d) show the penguin annihilation amplitudes PA_{Pq} and PA_{Vq}. Where the subscript q stands for the quark running in the loop at the weak vertex. PA_P is given by the following relation

$$PA_P = PA_{Ps} + PA_{Pd} - 2PA_{Pb}, \tag{2.12}$$

and analogously for PA_V. Finally, the PA_{PV} contribution is obtained as

$$PA_{PV} = PA_P + PA_V. \tag{2.13}$$

The topological diagrams of $PA_{Pq,Vq}^{break}$ is shown in Fig. 2.3, together with those relative to

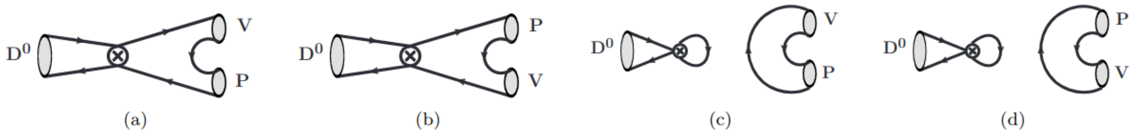

Figure 2.2: *$SU(3)_C$-limit topological amplitudes E_P (a), E_V (b), PA_{Pq} (c), and PA_{Vq} (d). The q in PA_{Pq} and PA_{Vq} labels the quark running in the loop at the weak vertex.*

the $E_{P(V)n}$ amplitudes, $n = 1, 2, 3$. The pictures (a), (b) and (c) show the $SU(3)_C$-breaking topological amplitudes of E_{Pn}, whereas the pictures (d), (e) and (f) show the amplitudes E_{Vn}. The pictures (g) and (h) depict the PA_P^{break} and PA_V^{break}, respectively. The PA_{PV}^{break} is given by an equation analogous to Eq. 2.13.

In the SU(3) limit Eqs. 2.8-2.11 imply

$$\mathcal{A}_{sd}(K^{*0}) = -\mathcal{A}_{sd}(\overline{K}^{*0}) \tag{2.14}$$
$$\mathcal{A}_{b}(K^{*0}) = \mathcal{A}_{b}(\overline{K}^{*0}). \tag{2.15}$$

Follows that the Eq. 2.3, can be written as follows for both the $D^0 \to K^{*0}\overline{K}^0$, $D^0 \to \overline{K}^{*0}K^0$ decays:

$$A_{CP}^{dir}(D^0 \to K^{*0}\overline{K}^0) = -\frac{Im(\Lambda_b)}{\Lambda_{sd}}\mathrm{Im}\Big(\frac{E_P + E_V + PA_{PV}}{E_P - E_V}\Big) \tag{2.16}$$
$$A_{CP}^{dir}(D^0 \to \overline{K}^{*0}K^0) = \frac{Im(\Lambda_b)}{\Lambda_{sd}}\mathrm{Im}\Big(\frac{E_P + E_V + PA_{PV}}{E_P - E_V}\Big), \tag{2.17}$$

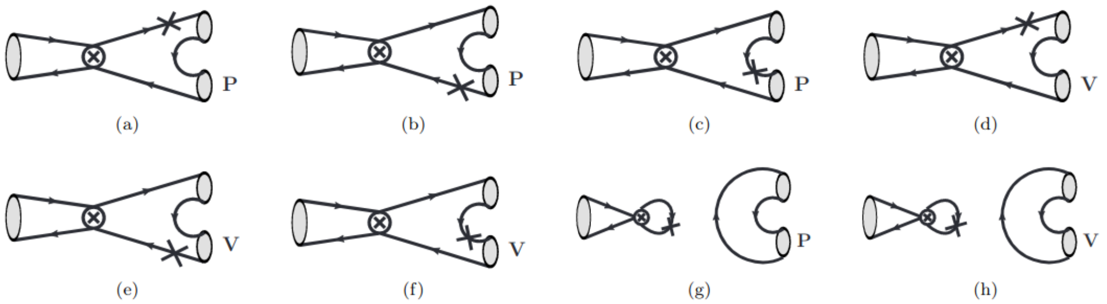

Figure 2.3: *$SU(3)_C$-breaking topological amplitudes: (a) E_{P1}, (b) E_{P2}, (c) E_{P3}, (d) E_{V1}, (e) E_{V2}, (f) E_{V3}, (g) $PA_P^{break} = PA_{Ps} - PA_{Pd}$, (h) $PA_V^{break} = PA_{Vs} - PA_{Vd}$ contributing to $D^0 \to K^{*0}\overline{K}^0$ and $D^0 \to \overline{K}^{*0}K^0$. The contribution PA_P^{break}andPA_V^{break} cannot be distinguished from each other.*

by implying the interesting relation between the two *CP* asymmetries

$$A_{CP}^{dir}(D^0 \to K^{*0}\overline{K}^0) + A_{CP}^{dir}(D^0 \to \overline{K}^{*0}K^0) = 0, \tag{2.18}$$

that can be used to experimental check the level of breaking of the $SU(3)_C$ symmetry. The two equations above also show that A_{CP}^{dir} can be enhanced if $E_P \sim E_V$. This can be only due to a possible contribution from $\frac{\mathcal{A}_b(d)}{\mathcal{A}_{sd}(d)}$, as shown in Eq. 2.2. The phase $Im(\Lambda_b/\Lambda_{sd}) = -6 \cdot 10^{-4}$ is a pure CKM phase, and it is small, while the small size of the two amplitudes, $|\mathcal{A}_{sd}(K^{*0})|$ and $|\mathcal{A}_{sd}(\overline{K}^{*0})|$ can be empirically determined from the following measured branching ratios [11]

$$\mathcal{B}^{exp}(D^0 \to K^{*0}K_S^0) = (1.12 \pm 0.21) \cdot 10^{-4} \tag{2.19}$$
$$\mathcal{B}^{exp}(D^0 \to \overline{K}^{*0}K_S^0) = (0.82 \pm 0.16) \cdot 10^{-4}, \tag{2.20}$$

where the presence of the K_S^0 is due to the fact it is the neutral kaon detectable, the K_L^0 do not decay inside the LHCb detector, as explained at the end of this section. The Eqs. 2.19 and 2.20 also entail $E_V \sim E_P$ for the two exchange amplitudes. $|\mathcal{A}_b(K^{*0})|$ and $|\mathcal{A}_b(\overline{K}^{*0})|$ are enhanced in this limit, because of the contribution from E and PA topologies. In conclusion, Ref. [9] shows that the contribution to the direct *CP*-violating asymmetry for those decays cannot exceed

$$|A_{CP}^{dir}| \lesssim 0.003.$$

There are also other features making $D^0 \to K^{*0}\overline{K}^0$ and $D^0 \to \overline{K}^{*0}K^0$ interesting for the search for charm *CP* violation [9].

- The direct *CP* asymmetry is canceled if $\frac{\mathcal{A}_b(d)}{\mathcal{A}_{sd}(d)}$ is real, as one can see in Eq. 2.3. This happens when the relative strong phase of interfering amplitudes equals zero or π, see Eq. 1.52. However, the strong phases strongly vary in the vicinity of resonances, hence one can perform the analysis in the vicinity of the invariant mass $m(K^{*0}) = 892$ MeV$/c^2$.

- The *CP* asymmetry does not vanish in the *untagged* D^0 decay, as shown in Ref [9], and assuming $SU(3)_C$ symmetry, one obtains $A_{CP}^{dir} = A_{CP}^{dir,untagged}$.

The *untagged* D^0 stands for that D^0 not coming from the main decay of the D^*. Therefore, nothing can be said about the flavour of the D^0: it cannot be tagged from the soft pion.

The *untagged* measurement is interesting because it comes with a significant statistical gain with respect to the *tagged* one[2].

The K^{*0} resonance decays, with a 100% branching ratio [11], into the pair $K^+\pi^-$. For what concerns the neutral kaon K^0, the following notation is used: $K_S^0 = \frac{1}{\sqrt{2}}(K^0 - \overline{K}^0)$ and $K_L^0 = \frac{1}{\sqrt{2}}(K^0 + \overline{K}^0)$. One can see that [9]

$$A_{CP}^{dir}(D^0 \to K^{*0}K_S^0) = A_{CP}^{dir}(D^0 \to K^{*0}K_L^0) = A_{CP}^{dir}(D^0 \to K^{*0}\overline{K}^0), \tag{2.21}$$
$$A_{CP}^{dir}(D^0 \to \overline{K}^{*0}K_S^0) = A_{CP}^{dir}(D^0 \to \overline{K}^{*0}K_L^0) = A_{CP}^{dir}(D^0 \to \overline{K}^{*0}K^0). \tag{2.22}$$

The K_L^0 particle lives to long to be detected with respect to a dector scale ($c\tau_{K_L^0}$ = 15.34 m [11] vs LHCb detector length $\sim$ 20 m). Therefore, the detectable final state is $D^0 \to K_S K\pi$ ($c\tau_{K_S^0} = 2.68$ cm [11]). It follows that the Eqs. 2.21 and 2.22 can be written

$$A_{CP}^{dir}(K^{*0}) \equiv A_{CP}^{dir}(D^0 \to K^{*0}K_S^0), \tag{2.23}$$
$$A_{CP}^{dir}(\overline{K}^{*0}) \equiv A_{CP}^{dir}(D^0 \to \overline{K}^{*0}K_S^0). \tag{2.24}$$

The D^0 particle decays into both $K_S^0K^+\pi^-$ and $K_S^0K^-\pi^+$ pairs with branching fractions reported in Eqs. 2.19 and 2.20. The equations are analogous for the $\overline{D}^0$. Therefore this final state involves 4 different decays:

$$\overset{(-)}{D}{}^0 \to K_S^0K^+\pi^- \tag{2.25}$$
$$\overset{(-)}{D}{}^0 \to K_S^0K^-\pi^+ \tag{2.26}$$

For simplicity, from here on, the inclusion of the charge conjugate is implied.

2.2 $D^0 \to K_S K\pi$: the laboratory decay channel

In a three-body decay (Fig 2.4), as the $D^0 \to K_S^0 K\pi$ decay mode, one can define two useful observables

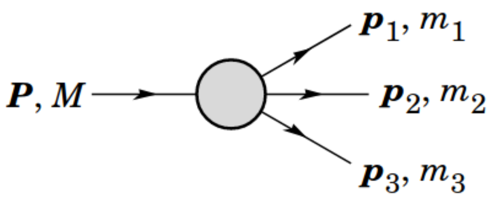

Figure 2.4: *Sketch of a three-body decay.*

$$m_{12}^2 := (\mathbf{p_1} + \mathbf{p_2})^2 \tag{2.27}$$
$$m_{23}^2 := (\mathbf{p_2} + \mathbf{p_3})^2, \tag{2.28}$$

where $\mathbf{p_i}$, $i = 1, 2, 3$ are the four-vectors of the particles of the final state. For a given value of m_{12}^2, the range of m_{23}^2 is determined:

$$(m_{23}^2)_{max} = (E_2^* + E_3^*)^2 - \left(\sqrt{E_2^{*2} - m_2^2} - \sqrt{E_3^{*2} - m_3^2}\right)^2, \tag{2.29}$$
$$(m_{23}^2)_{min} = (E_2^* + E_3^*)^2 - \left(\sqrt{E_2^{*2} - m_2^2} + \sqrt{E_3^{*2} - m_3^2}\right)^2, \tag{2.30}$$

[2]The present study is done using the *tagged* sample unless it is differently specified.

with $E_2^* = (m_{12}^2 - m_1^2 + m_2^2)/2m_{12}$ and $E_3^* = (M^2 - m_{12}^2 - m_3^2)/2m_{12}$ that are the energies of the particles 2 and 3 in the m_{12} rest frame. The scatter plot in m_{12}^2 and m_{23}^2 of a generic three-body decay is shown in Fig. 2.5. It is called *Dalitz Plot* (DP) and it is a useful representation of the decay. Indeed, if the matrix element of the decay $\overline{|\mathcal{M}|^2}$ is constant, the allowed region of the plot will be uniformly populated with events, as one can see from

$$d\Gamma = \frac{1}{(2\pi)^3 8M}\overline{|\mathcal{M}|^2} dm_{12}^2 dm_{23}^2. \tag{2.31}$$

The Equation 2.31 is valid if the decaying particle is scalar or one mediated over spin states [11]. Therefore, a non-uniformity on the plot gives immediately information about the dynamics of the decay. In presence of intermediate resonances bands, bumps, and wholes appear.

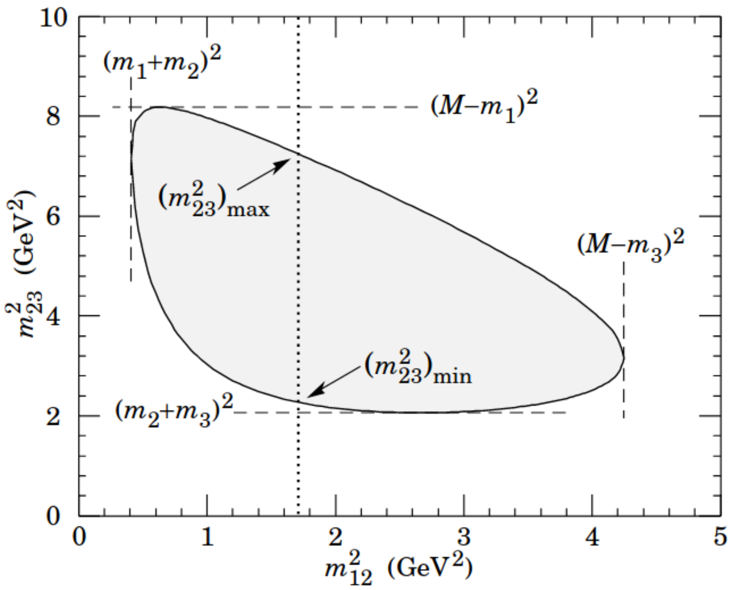

Figure 2.5: *Dalitz Plot for a three-body final state. Four-momentum conservation restricts events to the shaded region.*

For the $D^0 \to K_S^0 K\pi$ decay mode, which is the subject of this thesis, one can generally define as *ABC* the particle ordering convention of decay products, as reported in Tab. 2.1, together with the intermediate resonances contributing to the final state. In order

Decays		A	B	C
$D^0 \to K_S^0 \overset{(-)}{K}{}^{*0}$	$\overset{(-)}{K}{}^{*0} \to K^\pm\pi^\mp$	π	K	K_S^0
$D^0 \to K^\mp K^{*\pm}$	$K^{*\pm} \to K_S^0\pi^\pm$	K_S^0	π	K
$D^0 \to \pi^\mp(\rho^\pm, a^\pm)$	$(\rho^\pm, a^\pm) \to K_S^0 K^\pm$	K	K_S^0	π

Table 2.1: *Resonant structure of $D^0 \to K_S^0 K\pi$ modes. From Ref. [8].*

to disentangle the different contributions and to search for *CP*-violating asymmetries, LHCb performed a time-integrated amplitude analysis, as reported in Ref. [8], using pp collisions data corresponding to an integrated luminosity of 3.0 fb^{-1} collected during 2011 and 2012 (LHC Run 1) at center-of-mass energies $\sqrt{s} = 7$ TeV and 8 TeV, respectively. This sample contains about 189k signal decays, around one hundred times more with respect to the previous amplitude study of the same modes performed by the CLEO collaboration [15]. This kind of study is in general very complex and sophisticated, and allows distinguishing all the different amplitudes, contributing to the physical process of interest, through quantitative values (amplitudes and phases). The amplitude model is constructed using a formalism where the observed intensity is written as the coherent sum of resonant terms [23]. For the decay mode subject of this study, it reads as

$$|\mathcal{M}_{K_S^0 K^\pm \pi^\mp}(\mathbf{x}, m_{ABC})|^2 = \sum_S \left| \sum_R a_R e^{i\phi_R} \mathcal{M}_R(\mathbf{x}) \right|^2 + |a_{nr}|^2, \tag{2.32}$$

where a_{nr} is an incoherent non-resonant term, $\mathbf{x} = (m_{AB}^2, m_{AC}^2)$ represents the position in the Dalitz plot, whereas $a_R e^{i\phi_R}$ is the complex amplitude for the resonance $'R'$. The index S denotes the spin sub-state of the final states particles $(A, B, C\ )$. The matrix element $\mathcal{M}_R$, for each intermediate state, is given by the product of different factors[3] describing the resonance R. Once the probability density function (p.d.f) is well defined, a fit to data is performed, sharing all the parameters between the p.d.f.s for both modes ($D^0 \to K_S^0 K^+ \pi^-$ and $D^0 \to K_S^0 K^- \pi^+$) and both D^0 flavours, except for the complex amplitudes $a_R e^{i\phi}$. Table 2.2 shows, as an example, the fit results for the $D^0 \to K_S^0 K^- \pi^+$ mode. All intermediate resonances, contributing to the process, are listed in the table.

Resonance	a_R	ϕ_R(deg)	Fit fraction [%]
$K^*(892)^+$	1.0 (fixed)	0.0 (fixed)	$57.0 \pm 0.8 \pm 2.6$
$K^*(1410)^+$	$4.3 \pm 0.3 \pm 0.7$	$-160 \pm 6 \pm 24$	$5 \pm 1 \pm 4$
$(K_S^0\pi)^+_{S-wave}$	$0.62 \pm 0.05 \pm 0.18$	$-67 \pm 5 \pm 15$	$12 \pm 2 \pm 9$
$\overline{K}^*(892)^0$	$0.213 \pm 0.007 \pm 0.018$	$-108 \pm 2 \pm 4$	$2.5 \pm 0.2 \pm 0.4$
$\overline{K}^*(1410)^0$	$6.0 \pm 0.3 \pm 0.5$	$-179 \pm 4 \pm 17$	$9 \pm 1 \pm 4$
$\overline{K}_2^*(1430)$	$3.2 \pm 0.3 \pm 1.0$	$-172 \pm 5 \pm 23$	$3.4 \pm 0.6 \pm 2.7$
$(K\pi)^0_{S-wave}$	$2.5 \pm 0.2 \pm 1.3$	$50 \pm 10 \pm 80$	$11 \pm 2 \pm 10$
$a_2(1320)^-$	$0.19 \pm 0.03 \pm 0.09$	$-129 \pm 8 \pm 17$	$0.2 \pm 0.06 \pm 0.21$
$a_0(1450)^-$	$0.52 \pm 0.04 \pm 0.15$	$-82 \pm 7 \pm 31$	$1.2 \pm 0.2 \pm 0.6$
$\rho(1450)^-$	$1.6 \pm 0.2 \pm 0.5$	$-177 \pm 7 \pm 32$	$1.3 \pm 0.3 \pm 0.7$
$\rho(1700)^-$	$0.38 \pm 0.08 \pm 0.15$	$-70 \pm 10 \pm 60$	$0.12 \pm 0.05 \pm 0.14$

Table 2.2: *Fit results using GLASS model for the $D^0 \to K_S^0 K^- \pi^+$ mode obtained from the study in Ref.[8]. The first uncertainties are statistical and the second ones are systematic.*

The DP relative to both $D^0 \to K_S^0 K^- \pi^+$ and $D^0 \to K_S^0 K^+ \pi^-$ decay modes, using Run 1 data sample, are shown in Fig. 2.6. Both are dominated by an horizontal structure due to the presence of the intermediate $K^*(892)^\pm$ resonance. The $K^*(892)^0$ is visible as an excess in the high-$m^2_{K_S^0\pi}$ region in the $D^0 \to K_S^0 K^+ \pi^-$ mode, whereas it is visible as a destructively interfering contribution to the $D^0 \to K_S^0 K^- \pi^+$ mode at low-$m^2_{K_S^0\pi}$. Finally, the distribution of $m^2_{K\pi}$ and $m^2_{K_S^0\pi}$ are shown for both the decay modes in Fig. 2.7 and Fig. 2.8. The blue line stands for the global fit, whereas, the other curves with different colors stand for the main resonances contributing to the decay. Searches for time-integrated CP-violating effects in the resonant structure of these decays are also

[3]The $\mathcal{M}_R$ is given by the product of the Blatt-Weisskopf centrifugal barrier factors for the production and the decay of the resonance R [24], the spin factor of the resonance and, finally, the relativistic Breit-Wigner is used as a dynamical function to describe the propagators. For further details see Ref. [8].

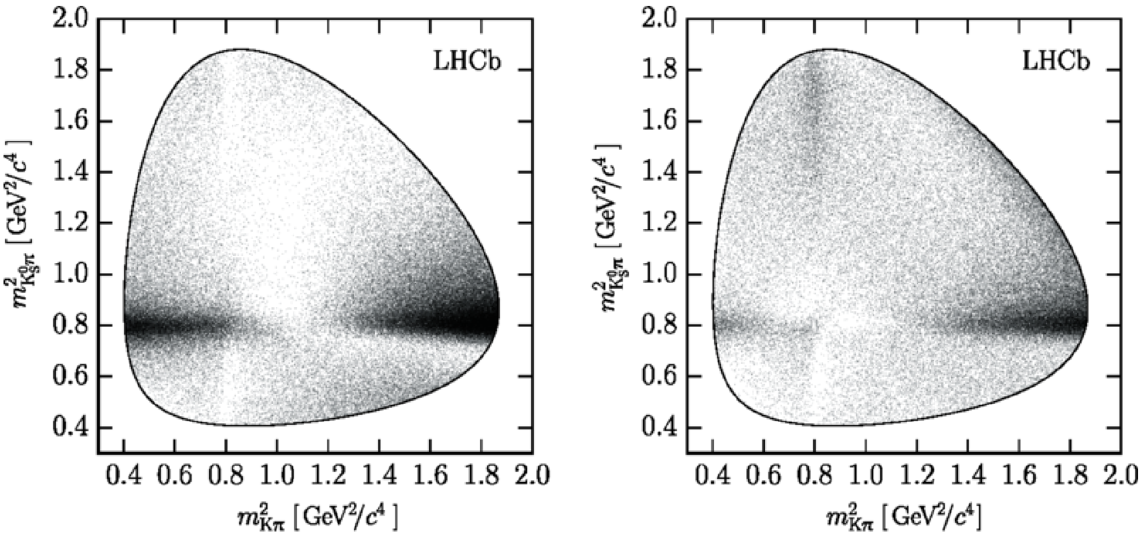

Figure 2.6: *Left: Dalitz plot of the $D^0 \to K^0_S K^- \pi^+$ mode. Right: Dalitz plot of the $D^0 \to K^0_S K^+ \pi^-$ mode.*

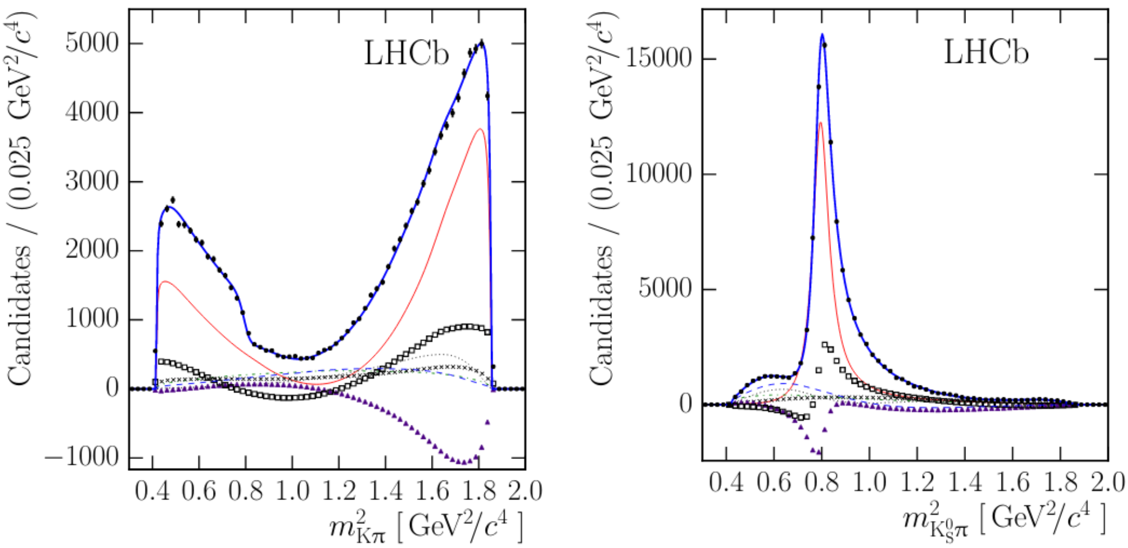

Figure 2.7: *Left: distribution of $m^2_{K\pi}$. Right: distribution of the $m^2_{K^0_S\pi}$. Both the distribution are for the $D^0 \to K^0_S K^- \pi^+$ mode.*

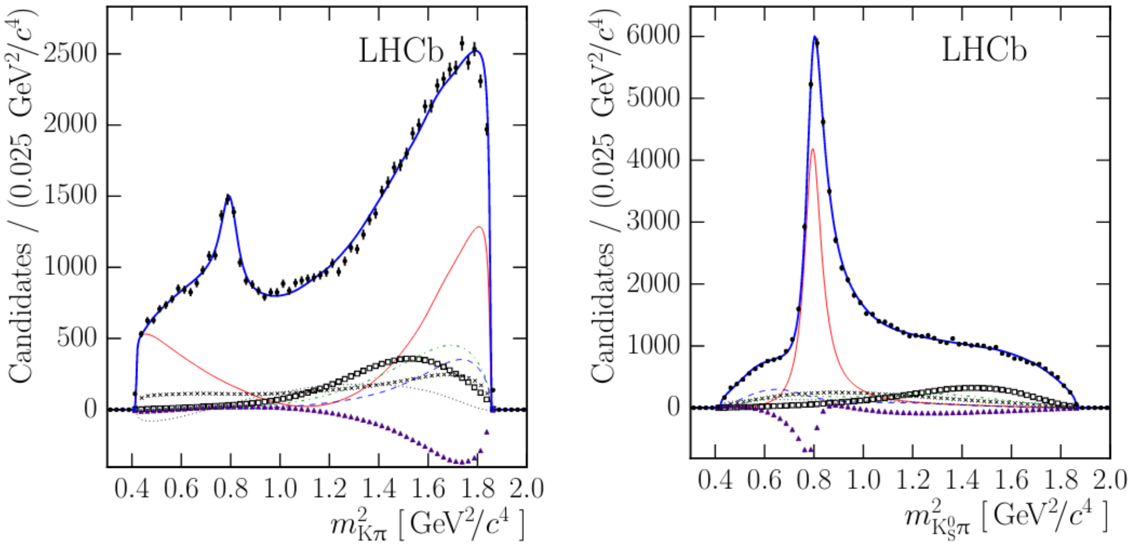

Figure 2.8: *Left: distribution of $m^2_{K\pi}$. Right: distribution of the $m^2_{K^0_S\pi}$. Both the distribution are for the $D^0 \to K^0_S K^+\pi^-$ mode.*

performed. The resonance amplitude and phase parameters a_R and ϕ_R are replaced with $a_R \pm \delta a_R$ and $\phi_R \pm \delta\phi_R$, respectively, where the signs are set by the flavor tag. No significant *CP*-violating effect has been found for all the amplitudes. For instance, using the GLASS model, one obtains $\delta a_R = -0.046 \pm 0.031$ (stat) ± 0.005 (syst) and $\delta\phi_R = (1.2 \pm 1.6$ (stat) ± 0.3 (syst)$)^\circ$ for the $D^0 \to K^0_S K^-\pi^+$ decays, $\delta a_R = -0.010 \pm 0.024$ (stat) ± 0.001 (syst) and $\delta\phi_R = (-1.4 \pm 2.9$ (stat) ± 2.2 (syst)$)^\circ$ for the $D^0 \to K^0_S K^+\pi^-$ decays, for the $K^*(892)^0$ resonance. Results for all contributing resonances can be found in Tab. XI of Ref. [8].

LHCb, nowadays, collected an additional data sample of pp collisions corresponding to an integrated luminosity of about 5.6 fb^{-1}, from 2015 to 2018 (the so called LHC Run 2) at center-of-mass energy $\sqrt{s} = 13$ TeV, by increasing the signal yields by about a factor of about 9 with respect to the previously analysed data sample, much higher than the factor 2 expected from the only increase of the integrated luminosity. This is mainly due to the optimized trigger system and to the increase of charm production cross section at the new center-of-mass energy of 13 TeV. After the application of final requirements, as it will be described in detail in Chapt. 5, the final Run 2 data sample contains about 1 M of $D^0 \to K^0_S K^-\pi^+$ RS decays and 0.7 M of $D^0 \to K^0_S K^+\pi^-$ WS signal candidates. It is, therefore, now possible to explore the region with a level of accuracy of per mil for such decay modes.

In this context, this thesis describes a new original analysis methodology to search for the time-integrated *CP* asymmetry, at very high precision, in the $D^0 \to K^0_S K^\pm\pi^\mp$ decays using the full LHCb Run 2 data sample, and without performing a full amplitude analysis, as the previous LHCb measurement. A model-dependent approach, as that one used in the previous analysis, is usually very complex and necessitates an accurate knowledge of a dynamic model to account for all the intermediate resonances contributing to the process of interest. This work, instead, aims at searching for *CP*-violating effects using a model-independent approach in order to exploit the whole sensitivity of the current available LHCb data sample, as suggested in Ref. [9]. The methodology developed in the thesis allows measuring the time-integrated *CP*-violating asymmetry, both by integrating over the entire Dalitz plot, or in a restricted region, such as in the vicinity of the $K^{*0} \to K\pi$ resonance. Any possible signal of violation of the *CP* symmetry, at the current level of accuracy, could be interpreted as a potential hint of New Physics, above all in the vicinity of the $K^*(892)^0$ resonance. A full amplitude analysis is necessary, in a later stage, to fully characterize the source of the observed standard or non-standard effect.

2.3 This thesis: the analysis strategy

The purpose of this work is to develop a new analysis method able to extract the full DP integrated *CP*-violating asymmetry, without performing an amplitude analysis. In order to do that, a calibration sample is used, *i.e.* a decay channel chosen ad-hoc, sharing many features (kinematics and nuisance asymmetries) with the signal mode. This approach allows to search for the *CP* violation even in a restricted region of the DP, as in the region populated by the K^{*0} resonance, where contributions from new interactions could enhance the value of the measured *CP* asymmetry with respect to the same value determined over the full DP or immediately near the resonance [9]. The method is based on two fundamental ingredients

- an 'appropriate' choice of the control mode,
- a reliable cancellation of all nuisance asymmetries (or of the majority of them) in the difference of the "raw" asymmetries between signal and control modes, in order to exploit the well-known ΔA_{CP} mechanism.

The "raw" asymmetry of a final state f is the quantity that can be directly measured from the experiment, and it is defined as

$$A_{\mathrm{raw}}(f) = \frac{N(D^0 \to f) - N(\overline{D}^0 \to \overline{f})}{N(D^0 \to f) + N(\overline{D}^0 \to \overline{f})}, \tag{2.33}$$

where N stands for the number of reconstructed D^0 and $\overline{D}^0$ meson candidates, and f is the final state of interest. This observable is linked to the *CP* asymmetry, but the measurement of the physics observable of interest, $A_{CP}(D^0 \to f)$, is contaminated by several experimental asymmetries. The flavour identification techniques, described in Sect. 1.6 , can easily introduce both acceptance and efficiency asymmetries, due to the additional charged particle whose sign is opposite for D^0 and $\overline{D}^0$ candidates. In fact, particles of opposite charge are deflected in opposite directions by magnetic field. Therefore, if the detector is not perfectly symmetric and aligned with the magnetic field, acceptance asymmetries occur. Moreover, particles of opposite charge usually interact differently with matter, causing also detection asymmetries. Furthermore, the number of D^{*+} and D^{*-} produced in pp collisions is not the same because the initial state of the collision is not CP-symmetric. As a result, for small asymmetries ($\mathcal{O}(10^{-2})$) , the "raw" asymmetry can be written as

$$A_{raw} \approx A_{CP} + A_D + A_P, \tag{2.34}$$

where A_D and A_P stand for the detection and production asymmetries, respectively. They may be nonzero due to the different interaction cross-sections of the matter and antimatter states with the LHCb detector. There may also be charge-dependent reconstruction and selection effects. In all cases, they depend on the kinematics of the involved particles, in fact, an experimental asymmetry is assumed to be fully parameterized by the kinematics of the objects involved.

The signal mode: $D^0 \to K^0_S K^\pm \pi^\mp$

The method is developed using the *tagged* D^0 reconstructed candidates, where the flavour is determined by the charge of the reconstructed 'soft' pion used to form the $D^{*\pm} \to \overset{(-)}{D}{}^0 \pi^\pm$ decay chain, as explained in Sect. 1.6. The knowledge of the flavour of the D^0 meson at production allows to separate the data sample into two different subsamples: if the pion coming from the D^0 has the same charge of the soft pion, the sub-set is called Right-Sign (RS), instead if the sign is opposite the relative sub-set is called Wrong-Sign (WS). The precise charge sign of the final states $K^0_S K\pi$ for the D^0 and $\overline{D}^0$ particles, RS and WS samples, is reported in Tab. 2.3. From here on, the inclusion of the charge conjugate is implied.

		RS	WS
$D^{*+} \to D^0 \pi_s{}^+$,	$D^0 \to$	$K^0_S K^- \pi^+$	$K^0_S K^+ \pi^-$
$D^{*-} \to \overline{D}^0 \pi_s{}^-$,	$\overline{D}^0 \to$	$K^0_S K^+ \pi^-$	$K^0_S K^- \pi^+$

Table 2.3: *Final states for the RS and WS subsamples.*

The "raw" asymmetry of the RS[4] signal mode reads

$$\begin{aligned} A^{RS}_{raw}(D^{*+} \to [K^0_S K^- \pi^+]\pi_s{}^+) \approx A^{RS}_{CP}(D^0 \to K^0_S K^- \pi^+) + A_P(D^{*+}) + \\ + A_D(\pi_s{}^+) + A^{RS}_D(K^- \pi^+) + A^{RS}_D(K^0), \end{aligned} \tag{2.35}$$

where

$A^{RS}_{CP}(D^0 \to K^0_S K^- \pi^+)$ is the time-integrated CP asymmetry of the signal mode, the physical leading quantity of the present study.

$A_P(D^{*+})$ is the production asymmetry of the D^*, due to the difference between the number of the D^{*+} and D^{*-} produced in the pp collisions. The measurement performed at pp collisions at the center-of-mass energy 7 TeV has evaluated this experimental asymmetry to be $A_P(D^+) = [-0.96 \pm 0.26\ \text{(stat)} \pm 0.18\ \text{(syst)}]\%$ [5] [25]

$A_D(\pi_s{}^+)$ and $A^{RS}_D(K^-\pi^+)$ terms are the detection asymmetries of the soft pion and of the $K\pi$ pair, respectively. The first one is due to the necessity to detect the soft pions, in order to provide the D^0 flavour tagging. The LHCb detector has in general a different probability (acceptance and interactions with the material) to reconstruct a positive and a negative soft pion. The detection asymmetry $A^{RS}_D(K^-\pi^+)$, instead, is nonzero because of the different interaction cross-sections of positive and negative kaons (and pions) in matter. Both effects are of the order of per cent [6].

[4] Similar equations hold for WS data sample.

[5] when integrated over the kinematic range $2.0 < p_T < 18.0$ GeV/c and $2.20 < \eta < 4.75$.

[6] The detection asymmetry $A_D(\pi_s{}^+)$ in general spans a range between $\pm 100\%$, however if averaged along the LHCb x direction, by exploiting the left-right symmetry of the LHCb detector, it is at level of few per cents.

$\boldsymbol{A_D^{RS}(K^0)}$ term is the time dependent detection asymmetry of the neutral K^0 and $\overline{K}^0$. The mass eigenstates of the neutral kaon are the K_S^0 and K_L^0 states, that entail a mixing of the K^0 and $\overline{K}^0$ states. The neutral kaon candidates are reconstructed in their *CP* eigenstate $\pi^+\pi^-$, leading the $K_S^0 \to \pi^+\pi^-$ decay to be *CP* violating[7]. Moreover, the K^0 and $\overline{K}^0$ mesons have different absorption rates in the detector material. All these effect (mixing, *CPV*, and absorption) interfere. An example of time evolution of the neutral kaon asymmetry traversing the matter is reported in Fig. 2.9 as a function of K_S^0 proper decay time, in units of $\tau_{K_S^0}$ [26]. The different contributions are obtained through a simplified model: the LHCb detector is modelled by a constant material distribution with a density equal to 2% of that of aluminium and it is assumed an average K_S^0 meson momentum of 30 GeV/c [26]. At the production, the flavour of the neutral kaon is defined. This means

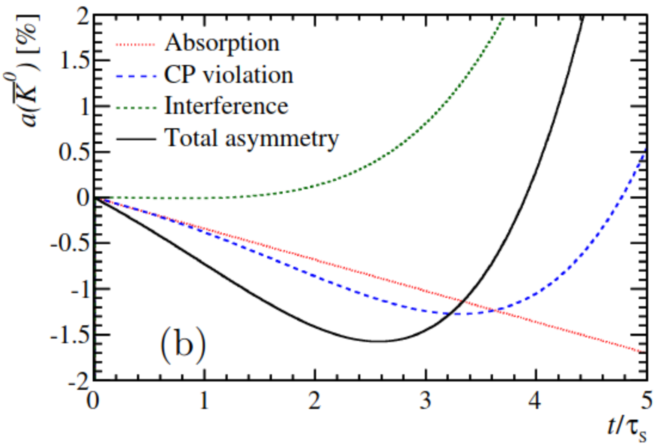

Figure 2.9: *The time-dependent neutral kaon asymmetry for K_S^0 decay time. Picture from Ref. [26].*

that the detection asymmetry $A_D^{K\pi}(K^0)$ is equal to zero for $t = 0$, as one can see from the figure.

The "raw" asymmetry for the WS sample is analogous to that one of the RS sample, shown in Eq. 2.35,

$$\begin{aligned} A_{raw}^{WS}(D^{*+} \to [K_S^0 K^+\pi^-]\pi_s{}^+) \approx A_P(D^{*+}) + A_{CP}^{WS}(D^0 \to K_S^0 K^+\pi^-)+ \\ +A_D^{WS}(K^+\pi^-) + A_D^{WS}(K^0) + A_D(\pi_s{}^+), \end{aligned} \tag{2.36}$$

where one can exploit the following relation

$$A_D(K\pi) := A_D^{RS}(K^-\pi^+) \approx -A_D^{WS}(K^+\pi^-), \tag{2.37}$$

and one can assume with a very good level of approximation

$$A_D^{K\pi}(K^0) := A_D^{RS}(K^0) \approx -A_D^{WS}(K^0). \tag{2.38}$$

Equations 2.35 and 2.36, therefore, can be rewritten as

$$\begin{aligned} A_{raw}^{RS}(D^{*+} \to [K_S^0 K^-\pi^+]\pi_s{}^+) \approx A_P(D^{*+}) + A_{CP}^{RS}(D^0 \to K_S^0 K^-\pi^+)+ \\ +A_D(K\pi) + A_D^{K\pi}(K^0) + A_D(\pi_s{}^+), \end{aligned} \tag{2.39}$$

$$\begin{aligned} A_{raw}^{WS}(D^{*+} \to [K_S^0 K^+\pi^-]\pi_s{}^+) \approx A_P(D^{*+}) + A_{CP}^{WS}(D^0 \to K_S^0 K^+\pi^-)+ \\ -A_D(K\pi) - A_D^{K\pi}(K^0) + A_D(\pi_s{}^+). \end{aligned} \tag{2.40}$$

[7]The K_S^0 is reconstructed in the symmetric $\pi^+\pi^-$ final state with a branching ratio of 69% [11], and it does not introduce any further detection asymmetry.

The control mode: $D^0 \to K^0_S\pi^+\pi^-$

The strategy used to search for the *CP* asymmetry in the $D^0 \to K^0_S K\pi$ signal mode involves the control mode $D^0 \to K^0_S\pi\pi$. The choice of the $D^0 \to K^0_S\pi\pi$ as control mode is given by its similarity with the signal mode. They both are a three-body decays involving a K^0_S. This leads to a simplification of the process to determine A_{CP}. The "raw" asymmetry of the control mode reads

$$\begin{aligned} A^{\pi\pi}_{raw}(D^{*+} \to [K^0_S\pi^+\pi^-]\pi_s{}^+) \approx A_{CP}(D^0 \to K^0_S\pi^+\pi^-) + A_P(D^{*+}) + \\ + A_D(\pi_s{}^+) + A_D(\pi^+\pi^-) + A^{\pi\pi}_D(K^0), \end{aligned} \tag{2.41}$$

where

$A_{CP}(D^0 \to K^0_S\pi^+\pi^-)$ is the time-integrate *CP* asymmetry of the $D^0 \to K^0_S\pi^+\pi^-$ decay channel. This observable is expected to be much smaller than the achievable uncertainty, being dominated by Cabibbo-Favoured decay modes. It is, therefore, assumed to be null for the measurement described in this thesis.

$A_P(D^{*+})$ and $A_D(\pi_s{}^+)$ are the production asymmetry of the D^* and the detection asymmetry of the π_s, the same as for the signal mode.

$A_D(\pi^+\pi^-)$ is the detection asymmetry of the pair $\pi^+\pi^-$. This is caused by the difference in the momentum dependent reconstruction efficiency of the charged pions. In the case of a three-body decay, where the resonances arrange differently in the Dalitz Plot, these differences are relevant. They do not cancel out between the particle and antiparticle (D^0 and $\overline{D}^0$) causing a net detection asymmetry different from zero [8]. The term $A_D(\pi^+\pi^-)$ is expected to be of the order of 0.1%, and it is measured with great accuracy using a sample of two-body $D^0 \to \pi^+\pi^-$ decays. The determination of this term is not subject of study of this thesis, and it will be assumed to be known with a very high precision. The methodology used to measure this quantity is currently developed within the LHCb-Pisa group in a parallel analysis effort.

$A^{\pi\pi}_D(K^0)$ is the time-dependent detection asymmetry of the neutral K^0. This detection asymmetry is analogous to the $A^{K\pi}_D(K^0)$. In general, they can be different because the presence of different interference terms and a different initial mixture of K^0 and $\overline{K}^0$. However, these two contributions are expected to be small. Therefore, they are treated initially as two different independent quantities, with a similar trend as function of the time (see Fig. 2.9).

The measurement: $\Delta A_{raw} = A_{raw}(D^0 \to K^0_S K\pi) - A_{raw}(D^0 \to K^0_S\pi\pi)$

The difference between the "raw" *CP* asymmetries of signal and control modes, for the RS decays as an example, is the following:

$$\begin{aligned} \Delta A^{RS}_{raw} = & A^{RS}_{raw}(D^{*+} \to [K^0_S K^-\pi^+]\pi_s{}^+) - A^{\pi\pi}_{raw}(D^{*+} \to [K^0_S\pi^-\pi^+]\pi_s{}^+) \approx \\ & A^{RS}_{CP}(D^0 \to K^0_S K\pi) + A_D(K\pi) - A_D(\pi\pi) + A^{K\pi}_D(K^0) - A^{\pi\pi}_D(K^0). \end{aligned} \tag{2.42}$$

[8] This term is not present for instance in the two-body $D^0 \to \pi^+\pi^-$ decay.

The same can be written using the WS decays, obtaining an analogous observable. Just few terms survive after the cancellation mechanism. The detection asymmetry of the π_s and the production asymmetry of the D^* cancel out in the difference as long as the kinematic of the decay $D^* \to D^0\pi_s$ is the same between signal and control samples. The $A_D(\pi^+\pi^-)$, as previously mentioned, will be assumed to be known at high accuracy, much better than the current achievable statistical uncertainty for the final measurement. In order to determine the observable of interest $A^{RS}_{CP}(D^0 \to K^0_S K\pi)$, it is necessary to 'remove' the remaining terms, related to the presence of a neutral kaon in both final states, and the detection asymmetry term $A_D(K^-\pi^+)$.

The detection terms of the neutral kaons As explained before, it is not possible to assume a priori that the two terms $A^{K\pi}_D(K^0)$ and $A^{\pi\pi}_D(K^0)$ are equal. Even if this could be assumed, the cancellation would work only for WS decays, and not for the RS ones, without any special treatment. Therefore, they will be considered as two different terms in the method. The K^0 detection asymmetry varies as a function of the K^0_S decay time, as shown in Fig. 2.9. It can be also noted that the trend can be assumed linear for short decay time values (up to $2.5\tau_{K^0_S}$) with a good level of accuracy. This is particularly true if one looks at the dependence of the ΔA_{raw} difference between the signal and the control mode. It is not possible to assume that the time dependence is the same between the two modes, but the difference can be assumed to be certainly small [9]. The difference between two approximately linear similar functions, as a function of the proper decay time of the K^0_S, can be further expanded at first order, and approximated with an excellent level of precision with a linear function.

The idea is, therefore, to exploit the fact that the neutral kaon detection asymmetry depends on decay time, and that is null for $t = 0$. Hence, the "raw" asymmetry of both signal and control samples, $A^{RS(WS)}_{raw}$ and $A^{\pi\pi}_{raw}$, are measured as a function of K^0_S proper decay time, precisely in bins, in order to perform a time dependent measurement of the golden $\Delta A_{raw}(t)$ difference, between the signal and the control mode. This observable is, then, fitted to a linear function, where the $\Delta A^{RS(WS)}_{raw}(t = 0)$ is the parameter of interest. In this way the contribution due to the difference of the neutral kaon detection asymmetries cancel out, obtaining

$$\Delta A^{RS}_{raw}(t = 0) \approx A^{RS}_{CP}(D^0 \to K^0_S K^-\pi^+) + A_D(K\pi) - A_D(\pi\pi), \tag{2.43}$$

$$\Delta A^{WS}_{raw}(t = 0) \approx A^{WS}_{CP}(D^0 \to K^0_S K^+\pi^-) - A_D(K\pi) - A_D(\pi\pi). \tag{2.44}$$

The remaining terms are assumed to be independent of the proper decay time of the neutral kaon. This is true with a very good level of approximation, for the current measurement, as it is described in Chapt. 8. A systematic uncertainty is associated to this assumption.

Detection asymmetry $A_D(K\pi)$ The $A_D(K\pi)$ detection asymmetry is determined by exploiting a similar approach based on a difference of raw asymmetries of two similar decay modes: the two-body $D^0 \to \pi\pi$ and $D^0 \to K\pi$ decays. The "raw" *CP* asymmetries of the $D^0 \to K\pi$ mode and the $D^0 \to K^0_S K\pi$ signal mode share the same detection asymmetry ($A_D(K\pi)$). The kinematics of the $K\pi$ pair of the two-body decays must be reweighted to the kinematics of the same pair of the $D^0 \to KsK\pi$ decays mode. The $D^0 \to \pi\pi$ decay mode is necessary to precise cancel out all other nuisance detection

[9]This can be in any case verified a *posteriori* using data itself.

asymmetries, such as $A_p(D^*)$ and $A_D(\pi_s)$, in order to extract only the detection term of interest. The "raw" CP asymmetry of the $D^0 \to K\pi$ control sample [10] reads

$$\begin{aligned} A^{RS}_{raw}(D^{*+} \to [K^-\pi^+]\pi_s{}^+) \approx A_P(D^{*+}) + A^{RS}_{CP}(D^0 \to K^-\pi^+) + \\ + A^{RS}_D(K^-\pi^+) + A_D(\pi_s{}^+), \end{aligned} \tag{2.45}$$

where $A^{RS}_{CP}(D^0 \to K^-\pi^+)$ can be considered null because it is a Cabibbo-favoured decay. A similar relation can be written for the $D^0 \to \pi^+\pi^-$ decays

$$\begin{aligned} A^{\pi\pi}_{raw}(D^{*+} \to [\pi^-\pi^+]\pi_s{}^+) \approx A_P(D^{*+}) + A_{CP}(D^0 \to \pi^+\pi^-) + \\ + A_D(\pi^+\pi^-) + A_D(\pi_s{}^+), \end{aligned} \tag{2.46}$$

where, in this case, the detection asymmetry of the pair $\pi^+\pi^-$ is equal to zero. The $D^0 \to \pi^+\pi^-$ is a two-body decay, therefore there is no Dalitz Plot structure. The difference between the raw asymmetries of $D^0 \to K\pi$ RS and $D^0 \to \pi\pi$ decays modes, therefore, reads as

$$\begin{aligned} A^{RS}_{raw}(D^{*+} \to [K^-\pi^+]\pi_s{}^+) - A^{\pi\pi}_{raw}(D^{*+} \to [\pi^-\pi^+]\pi_s{}^+) \approx \\ -A_{CP}(D^0 \to \pi^+\pi^-) + A^{RS}_D(K^-\pi^+), \end{aligned} \tag{2.47}$$

where the value of $A_{CP}(D^0 \to \pi^+\pi^-)$ is known to be $(0.07 \pm 0.14(\text{stat}) \pm 0.11(\text{syst}))\%$ from literature [27]. Hence, the detection asymmetry of the pair, $A^{RS}_D(K^-\pi^+)$ can be computed. The relation of Eq. 2.37 allows to immediately determine also $A^{WS}_D(K^+\pi^-) = -A^{RS}_D(K^+\pi^-)$.

[10] As for the $D^0 \to K^0_S K\pi$ also for two-body decays it is possible to define RS and WS decays. In this case, however, RS decays are Cabibbo-Favoured, while WS are doubly-Cabibbo-suppressed decays.

3 The LHCb experiment at the LHC

This chapter briefly describes the Large Hadron Collider and the LHCb experiment, which is the experimental apparatus used to collect the data samples analysed in this thesis work.

3.1 The Large Hadron Collider

The Large Hadron Collider (LHC) is a superconducting circular hadron accelerator and more precisely a proton-proton (pp) collider operating at the laboratories of CERN (*Conseil Européen pour la Recherche Nucléaire*). It is hosted in the 27 km tunnel that previously housed the Large Electron Positron collider (LEP), sited about 100 m underground across the French-Swiss border near Geneva[28].
Protons are extracted from hydrogen gas, then they pass through various sequential acceleration stages to increase their energy, before being injected in the LHC. A schematic representation of the CERN accelerator complex is reported in Fig. 3.1:

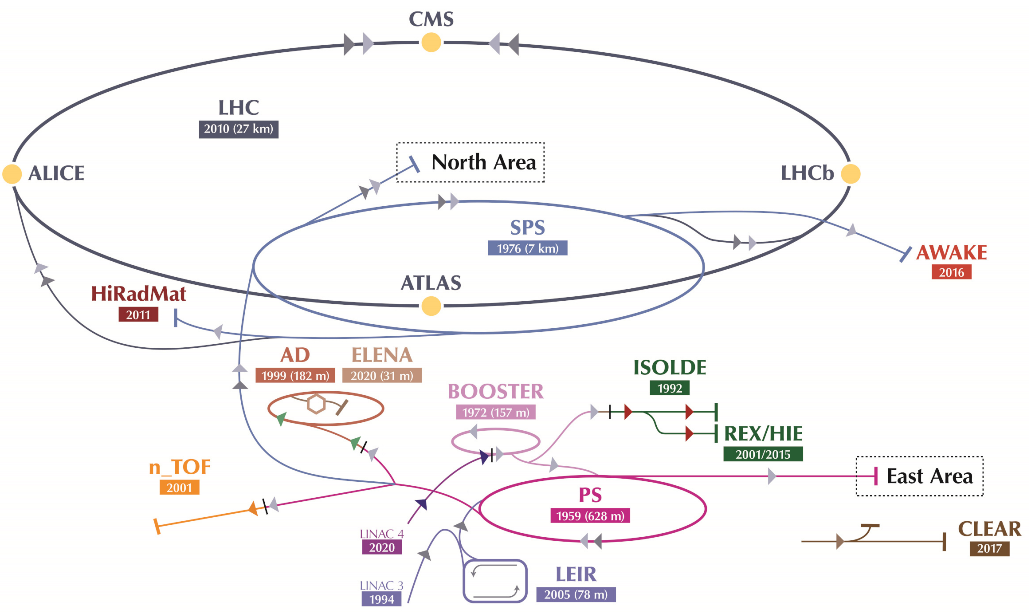

Figure 3.1: *CERN accelerator complex.*

1. **LINAC 2** : protons are first accelerated in a Linear Accelerator up to 50 MeV.

2. **BOOSTER**: in the Proton Synchrotron Booster, the beams reach the energy of 1.5 GeV.

3. **PS**: beams circulating in the Proton Synchrotron reach a maximum energy of 25 GeV

4. **SPS**: beams are then injected in the Super Proton Synchrotron, where they reach the energy of 450 GeV.

Finally, proton beams are injected in the LHC, where they circulate in opposite directions accelerated by radio-frequency (RF) cavities. The beams are bent around the circumference of the LHC using NbTi superconducting dipole magnets which produce a field of 8.3 T, thanks to their low temperature, 1.9 K, reached by using a liquid helium cooling system. Ultra-high vacuum is needed for the pipes in which particle beams travel ($1.013 \cdot 10^{-10}$ mbar or 10^{-13} atmospheres), to avoid collisions with gas molecules inside the accelerator.
Beams collide in four interaction regions placed along the LHC ring, where the detectors of the four major LHC experiments are installed: ALICE, ATLAS, CMS and LHCb.
The energy in the center of mass was kept at $\sqrt{s} = 7$ TeV in 2011 , while in 2012 it was raised to 8 TeV. After a two years shut-down, in which several upgrades and checks to magnets system were done, LHC was restarted at the energy of 13 TeV, maintained for the entire Run 2: from 2015 to the end of 2018.
Proton beams are grouped in bunches of about 10^{11} protons and are time-spaced by a multiple of 25 ns (50 ns in Run1), corresponding to a bunch-crossing rate of 40 MHz (20 MHz in Run1). However, bigger gaps are present between some bunches, in order to allow the injection and the dumping of the beams. Therefore, the effective crossing rate is about 30 MHz (15 MHz in Run1). Thanks to the relation below, it is possible to calculate the events rate:

$$\frac{dN}{dt} = \mathcal{L} \cdot \sigma(\sqrt{s}) \cdot \epsilon \tag{3.1}$$

where ϵ is the detection efficiency, $\sigma(\sqrt{s})$ is the cross section of the process at center-of-mass energy $\sqrt{s}$. $\mathcal{L}$ is the LHC instantaneous luminosity, assuming the distribution of the protons in the bunches to be Gaussian (good approximation for bunches at LHC), $\mathcal{L}$ can be defined according to the relation:

$$\mathcal{L} = \frac{kfn_1n_2}{4\pi\sigma_x\sigma_y} \cdot \frac{1}{\sqrt{1 + (\frac{\sigma_z}{\sigma_x} \tan\frac{\phi}{2})^2}} \tag{3.2}$$

where

- k is the number of bunches per beam ($\sim$ 2500 in Run2).

- f is the revolution frequency of the bunches (f $\sim$11kHz).

- n_1 and n_2 are the number of proton in the 2 colliding bunches: $n1 = n2 = 10^{11}$. $\sigma_x, \sigma_y, \sigma_z$ are the standard deviation in the three spatial direction of the gaussian distributed bunch $\sigma_x = \sigma_y \sim 16\mu$m and $\sigma_z \gg \sigma_x, \sigma_y$.

- ϕ is the crossing-angle between the two beams.

Another handy quantity is the integrated luminosity, $L = \int \mathcal{L}dt$, that multiplied by the interesting cross section straight gives the number of events of the process of interest. The LHCb experiment is not limited by the number of $c\bar{c}$ and $b\bar{b}$ produced in the pp interactions but by the trigger, reconstruction efficiencies and by the amount of data that can be saved to be analysed. While CMS and ATLAS aim to reach the maximum peak luminosity of $\sim 10^{34}\mathrm{cm}^{-2}\mathrm{s}^{-1}$, LHCb is designed for a much lower luminosity. Hence, the luminosity is kept constant to the level of $2 \cdot 10^{32}\mathrm{cm}^{-2}\mathrm{s}^{-1}$ by introducing an transverse offset between the two colliding beams [29]. Only in 2012 it was increased to $4 \cdot 10^{32}\mathrm{cm}^{-2}\mathrm{s}^{-1}$.

3.2 LHCb detector

The Large Hadron Collider beauty (LHCb) experiment is the only LHC experiment entirely dedicated to heavy flavor physics. Its primary goal is to search for indirect evidences of non-SM physics in heavy quark transitions, mainly by studying CP violation and rare decays of charmed and bottom hadrons[30]. The LHCb detector is a single-arm spectrometer with a forward angular acceptance between 10 *mrad* and 300 (250) *mrad* in the horizontal (vertical) plane, corresponding to a pseudorapidity range of $1.8 < \eta < 4.9$[1].

The reason of this design choice must be sought in the main research aim of the experiment: in a high-energy pp collider, b and c quarks are mainly produced in $b\bar{b}$ and $c\bar{c}$ pairs by strong interaction. These pairs are likely to be produced along the beam axis, in a forward and a backward cones along the beam axis pairs via the strong interaction, as shown in Fig. 3.2. Developed only in the forward direction, the LHCb detector collects

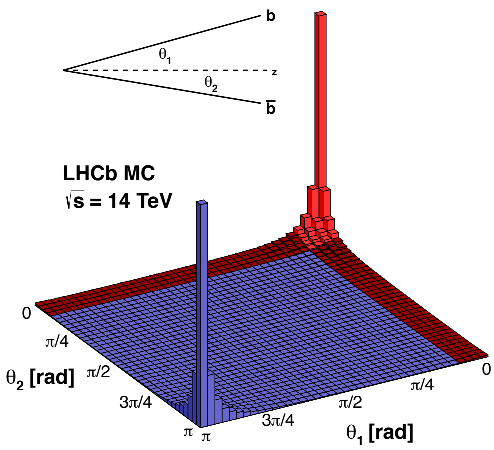

Figure 3.2: *$b\bar{b}$ production cross section as a function of their polar angle with respect to the beam axis, in pp collisions simulated with Pythia[31]. The LHCb acceptance is displayed in red.*

24%[32] of the total $b\bar{b}$ produced pairs, with a much lower covered solid angle compared to general purpose detectors such as CMS and ATLAS ($|\eta| < 2.4$), with a clear advantage in terms of costs and ease of construction and access to sub-detectors.
Before to start the description of the LHCb experiment, its reference system is defined as follows:

[1] $\eta = -\log(\tan(\frac{\theta}{2})$ and θ is the polar angle with respect to the beam direction

- The *origin* of the coordinate system O is the nominal interaction vertex position of the pp collision.
- The *z-axis* is aligned to the nominal beam direction.
- the *x-axis* and *y-axis* are respectively the horizonatal and vertical axis, perpendicular to each other and to the beam axis.

While, in the following lines a schematic description of the LHCb detector is given and a sketch is reported in Fig. 3.3:

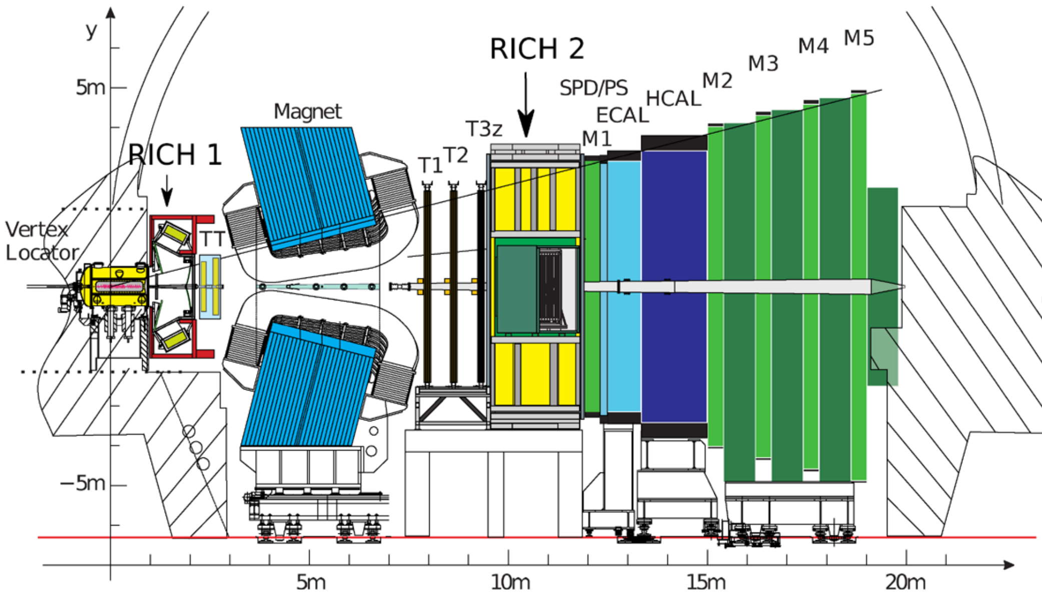

Figure 3.3: *Side view of LHCb detector.*

- **VELO:** the VErtex LOcator is a silicon strip detector placed around the pp interaction vertex, which aims to reconstruct with high precision the position of decay vertices;
- **RICH1:** the first Ring Imaging CHerenkov detector is placed next to the VELO. Its main function is to help in particle identification (PID) for particles in the 1-60 GeV/c momentum range;
- **TT:** the Track Turcensis is a silicon strip detector placed just before the magnet;
- **Magnet:** a warm dipole magnet provides a bending power of 4 Tm for the measurement of particles momenta;
- **T1, T2, T3:** three station made up of two subdetectors, the Inner Tracker (silicon strips) and Outer Tracker (straw tubes);
- **RICH2:** the second Ring Imaging Cherenkov covers a different momentum range with respect to the RICH1 (15-100 GeV/c);
- **ECAL:** the Electromagnetic CALorimeter identifies electrons and photons and gives important information for the trigger system;

- **SPD/PS:** the Scintillating Pad and the Preshower Detectors improve the particle identification of electrons;
- **HCAL:** the hadronic calorimeter is used to identify and trigger hadrons;
- **M1-5:** finally five muon stations (multi-wire proportional chambers alternated to iron layers) identify and trigger muons, the only particles capable to reach this region of the detector.

3.3 Tracking system

The tracking system must provide accurate spatial measurements of charged particle tracks, in order to allow quantities such as charge, momentum, and vertex locations to be determined.

The dipole magnet

The LHCb magnet is placed between the TT and the T-stations and provides bending for the measurement of the momentum of particles. The magnet is formed by two saddle-shaped coils placed with a small angle with respect to the beam axis, to increase the opening window with z, in order to follow the acceptance of the LHCb detector. The field mainly develops in the y direction, as shown in Fig. 3.4, hence particles are bent in the xz plane. The maximum intensity of the field is about 1.1 T, while its integral

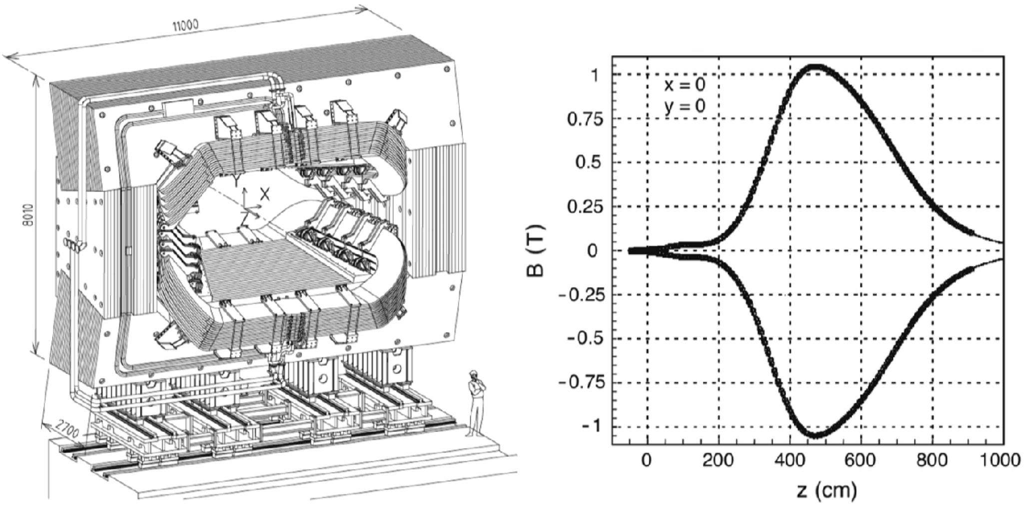

Figure 3.4: *Left: prospective view of the dipole (lengths in mm), the interaction point is behind the magnet. Right: the y component of the magnet field varying along z, for both the polarities.*

$\int Bdl = 4$ Tm. Before the data-taking period, a precise map of the magnetic field is obtained with Hall probes, in order to ensure good momentum resolution. The geometry of this detector is not charge symmetric. Indeed, due to the vertical field, particles will be bent in a direction or in the opposite one, depending on the charge: as a result, some parts of the detector will preferably interact with particles of a certain sign, generating detection charge asymmetry, especially for low momentum particles that are heavily bent. In order to help reducing this detector charge asymmetry, an important and unique feature was designed: the possibility of reversing the polarity of the magnet (MagUp or MagDw). The magnet polarity is inverted about every two weeks.

Vertex Locator detector

The VErtex LOcator is a silicon strip vertex detector that surrounds the interaction region at LHCb. The principal task of the VELO is to enable LHCb to trigger on and reconstruct displaced vertices, as well as to play a significant role in the tracking[33]. It provides precise measurement of charged particles trajectories in this region, so that it is possible to precisely:

- measure particles momenta, by comparing the tracks directions reconstructed in the VELO (before the magnet) with those reconstructed in the T stations (after the magnet);
- reconstruct pp interaction vertices (primary vertices) and displaced secondary vertices.

The presence of a displaced secondary vertex is a signature of b- or c-hadrons decays, whose mean flight distance from creation in the primary vertex to the decay is $\mathcal{O}(cm)$. The VELO consists of a series of 42 semicircular silicon modules arranged perpendicularly to the beam axis and spaced in a way that every track in the LHCb acceptance intercepts at least four modules, as shown in Fig. 3.5. They are placed both upstream and downstream

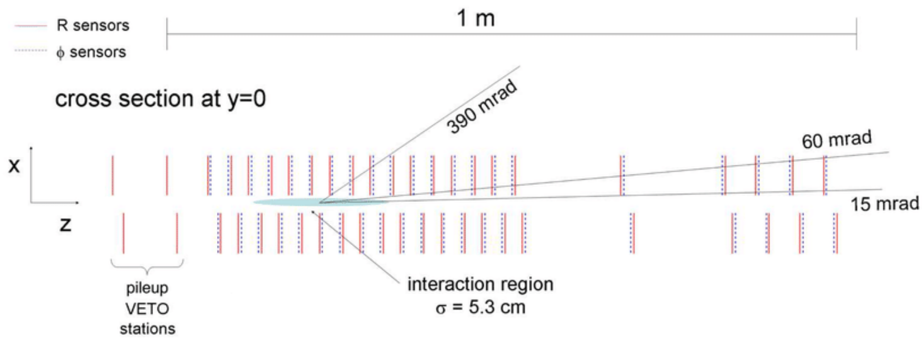

Figure 3.5: *Representation of VELO detector, with a transverse view in the (x, z) plane.*

of the nominal interaction point and they can be bundled in 21 tracking stations. Each tracking station is composed by two modules that slightly overlap. Furthermore, every module is formed by two overlapped sub-modules that independently measure R and ϕ coordinates (see Fig. 3.6). Both R and ϕ sensors have a 300 μm thick sensitive area that covers the region from R = 8.2 mm to R = 41.9 mm. The R sensor consists of concentric semicircular strips, divided in four 45° sector each, to reduce occupancy. The pitch increases linearly from 38 μm at the innermost radius to 101.6 μm at the outermost radius. The ϕ sensor is subdivided in two concentric regions: the inner region consists of 683 strips extending to R = 17.25 mm with a $\sim$ 20° angle to the radial direction, while the outer one covers the remaining region with 1365 strips with a $\sim$ 10° angle to the radial direction. In this way, the pitch increases linearly from the centre, with a discontinuity in passing from the inner to the outer region. A representation of Rϕ geometry of VELO sensors is shown in Fig. 3.6 on the right hand. The whole VELO system is placed inside the LHC vacuum pipe in order to place the sensors as close to the primary interactions as possible. To protect the integrity of the primary LHC vacuum system, the sensors are separated from the beam volume by a 0.3 mm aluminium shield known as "RF-foil". It

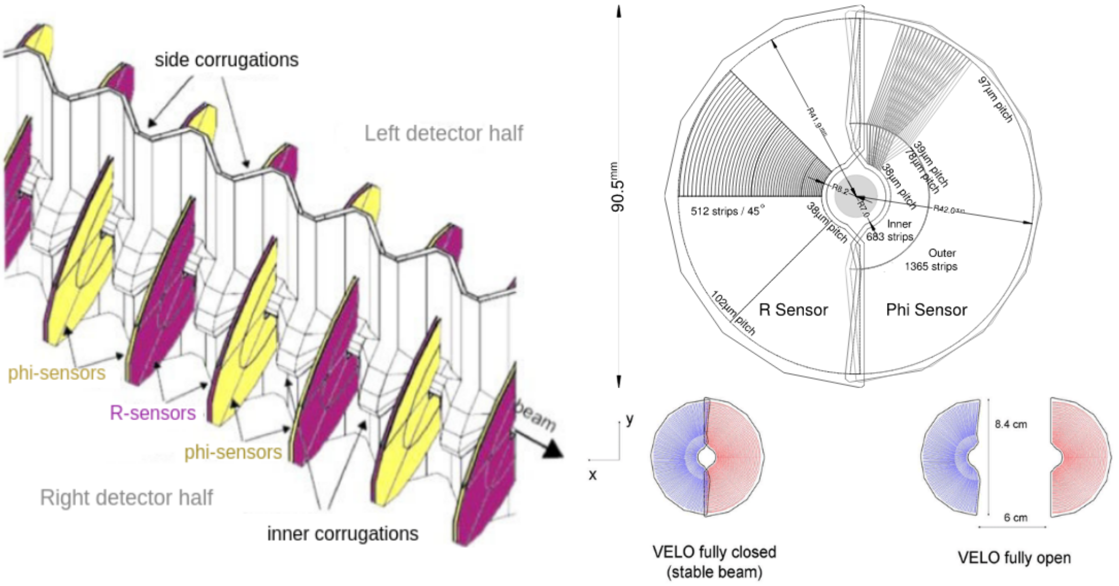

Figure 3.6: *Left: Representation of RF-foils in closed configuration. Right: Rϕ geometry of VELO sensors.*

has a characteristic corrugated shape, as shown in Fig. 3.6 on the left hand, in order to allow for modules overlapping. During the injection procedure at the LHC, the VELO beam-hole is too small to avoid damages to the sensors. Hence, waiting for the beam to become stable, the two halves are retracted by 3 cm.

Tracker Turicensis

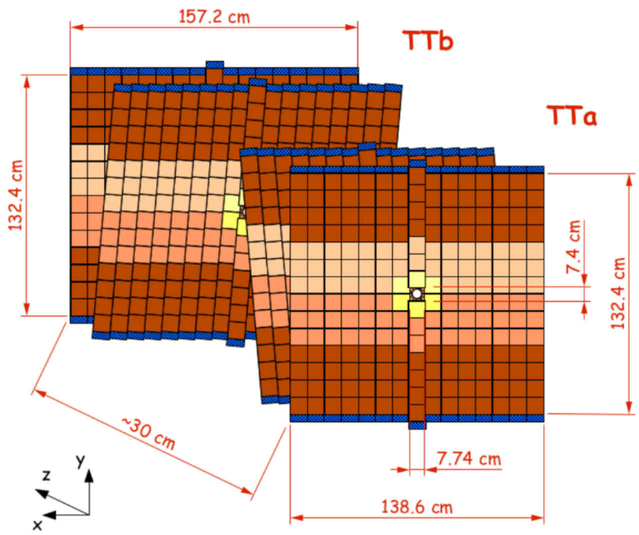

Figure 3.7: *"x-u-v-x" configuration of TT station.*

The Track Turicensis (TT) is a silicon micro-strip detector placed just before the magnet that has two purposes: detect low-momentum particles, that otherwise would be bent out of the acceptance of the experiment by the magnet and thus would not reach stations T1-T3. Then, the TT is important to reconstruct long-lived particles, such as

K_S^0 and Λ. It consists of four 150 cm $\times$ 130 cm layers, corresponding to the full LHCb angular acceptance, grouped in two stations separated by 30 cm along the beam line. These layers are arranged in a "x-u-v-x" pattern, as shown in Fig. 3.7: the first and the last layers consist of vertical strips ("x" configuration), while the second and the third layers are rotated by $\pm$ 5° respect to the vertical ("u" and "v" configuration). This small tilt provides a measurement of y direction, even though with a lower resolution; it is not fundamental for momentum measurements (particles bend in the x direction) but it allows to reduce the ambiguities, in order to reduce the background. Each sensor module is 500 μm thick with a sensitive region of 9.6 cm $\times$ 9.4 cm, carrying 512 readout strips with a pitch of 183 μm.

T stations

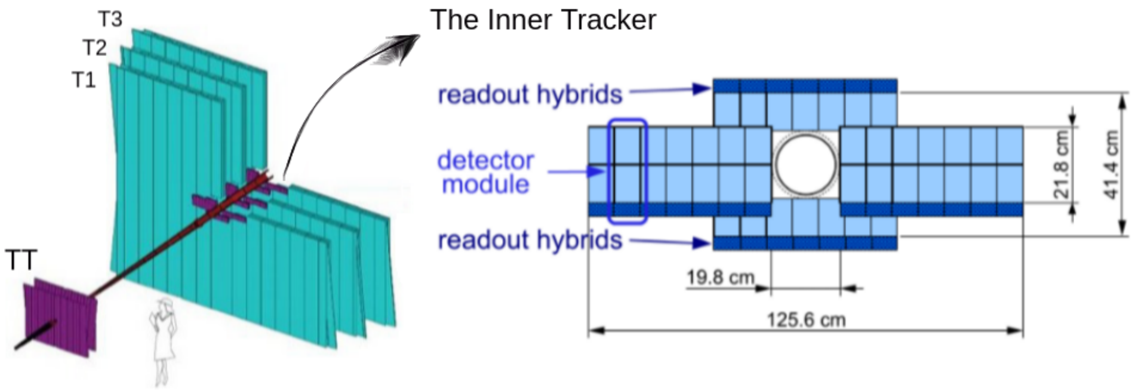

Figure 3.8: *Left: a sketch of the whole T-stations with respect to the TT. Right: layout of one IT layer.*

The T-stations (T1, T2, T3) are three tracking stations placed just downstream of the magnet, in order to measure charged particles momentum. The Fig. 3.8 on the left, show the T-stations with respect to the TT and in particular that the T-stations are made up of two sub-detectors :

- a small - purple colored - **Inner Tracker** (IT), made of silicon micro-strip. It covers the high occupancy region around the beam pipe.
- a much bigger - green colored - **Outer Tracker** (OT), made of straw tubes. It covers the whole LHCb geometrical acceptance with lower occupancy.

Both the sub-detector are made up of four detection planes in the same "x-u-v-x" arrangement used for the TT. The **Inner Tracker** [34] is a silicon micro-strip detector mounted in the inner region of each T-station. It develops in the horizontal direction, as shown on the right hand side of Fig. 3.8, with a cross shape about 125 cm wide and 40 cm high. The silicon micro-strip modules are similar to the TT ones, with the same pitch of 198 μm and a different sensitive region of 7.6 cm $\times$ 11 cm.

Whereas, the **Outer Tracker** [35] is a gaseous ionization detector that covers an area of about 6 m $\times$ 5 m. It consists of 2.4 m long straw tubes with an inner diameter of 4.9 mm, operating as proportional counters. Each detection plane is made up of two rows of staggered drift tubes, see Fig. 3.9. The gas mixture filling the tube is $Ar/CO_2/O_2$ (70%/28.5%/1.5%), which allows to achieve a drift time of 50 ns. The hit efficiency is above 99% for tracks passing close to the centre of a tube.

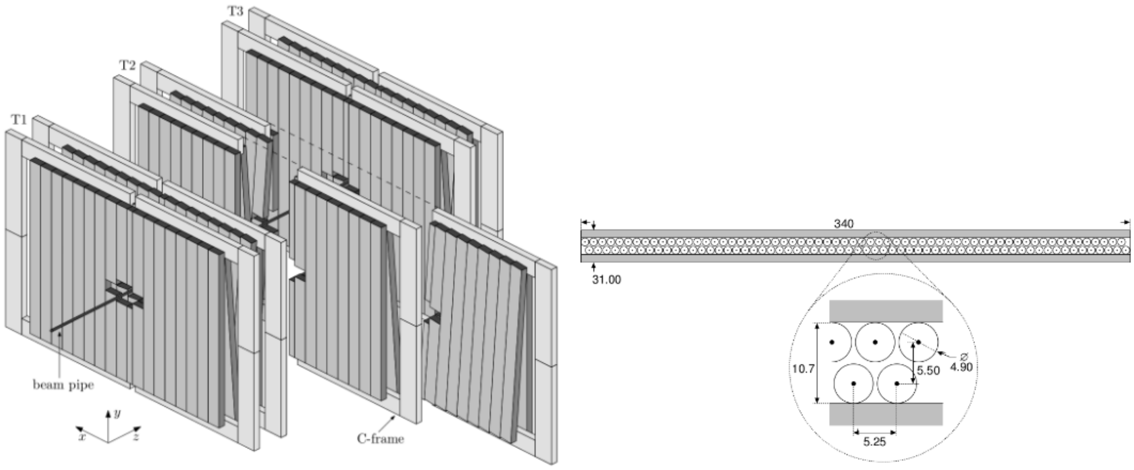

Figure 3.9: *Left: geometry of the OT detector planes. Right: section of a single OT module.*

3.4 Particle identification system

An excellent particle ID performance is vital for LHCb physics in order to reject backgrounds and for the classification of the final states. Cherenkov detectors are able to separate between charged kaon and pions, while calorimeter detectors allow identification of electrons, photons and hadrons. Instead, muons are identified by muon chambers. It follows a detailed explanation of these sub-detectors.

The Ring Cherenkov detectors

The primary role of the RICH system is the identification of charged hadrons (π, K, p). In order to do that, one of the major requirements in a flavour-physics experiment is the reduction of combinatorial background [36]. In fact, many of the interesting decay modes of b- and c-flavoured hadrons involve hadronic multibody final states. The two Cherenkov detectors (RICH1 and RICH2) allow to distinguish charged hadrons in a range from 1 GeV$/c$ to 100 GeV$/c$, exploiting the Cherenkov effect. Consider a particle that crosses a medium (refraction index n) with velocity v. If its velocity is higher than the speed of light in that medium ($v > c/n$) , photons are emitted in a cone with angle θ_C, defined as:

$$\cos\theta_C = \frac{1}{\beta n}, \quad \beta = v/c. \tag{3.3}$$

It follows that Cherenkov light is emitted only if $\beta > 1/n$. In both RICH detectors, a complex system of spherical and plane mirrors reflects the emitted photons outside the LHCb acceptance, where they are collected by a lattice of hybrid photon detectors (HPDs). In this way, HPDs can be shielded from the magnetic field, see Fig. 3.10. Since particles momentum p is known from tracking system, it is possible to find the particle mass from the following relation:

$$\theta_C = \arccos\left(\frac{1}{n}\sqrt{1+\left(\frac{mc}{p}\right)^2}\right) \tag{3.4}$$

In order to achieve the best separation power between pion and kaon mass hypotheses, corresponding to a big difference in Cherenkov angles at high momenta, a small refractive

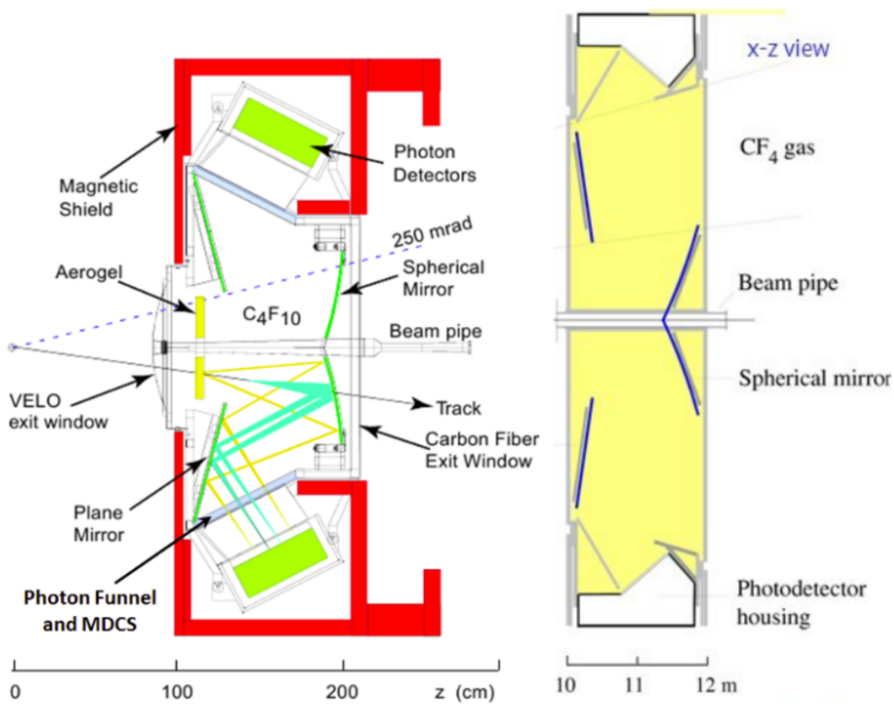

Figure 3.10: *RICH1 geometry on the left hand and RICH2 geometry on the right hand.*

index (approaching to 1) is needed. However, the smaller the refractive index is, the bigger is the threshold momenta under which Cherenkov light is not emitted. Therefore a compromise had to be reached. To cover a large range of momenta, two RICH detectors are used at LHCb, based on two different refractive indices. The RICH1 covers the low momenta range 1-60 GeV/c, by using the aerogel (n = 1.03) and C_4F_{10} (n = 1.0014) radiators, that provide a maximum Cherenkov angles of 242 mrad and 53 mrad respectively. It is placed before the magnet (between VELO and TT) in order to identify the particles that are bent out from the LHCb acceptance by the magnetic field. The RICH2 is placed after T3 station and covers the high momenta range 15-100 GeV/c using CF_4 (n = 1.0005) as radiation medium that produces a maximum Cherenkov radiation of 32 mrad. In Fig. 3.11, it is shown the trend of the Cherenkov angle as a function of particle momentum for different particles and radiators.

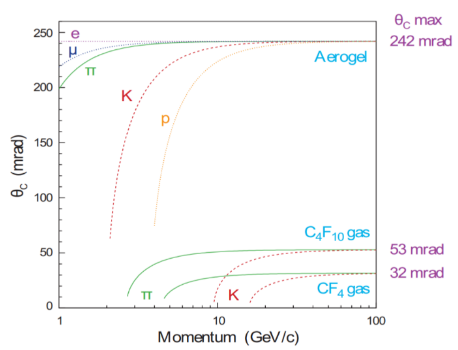

Figure 3.11: *Cherenkov angles as a function of particles momentum for the different radiators used at LHCb.*

Calorimeter detectors

Calorimeter detectors provide fast information for the low level trigger and offer identification of electrons, photons, and hadrons, together with a raw measurement of their energies and positions. The calorimetric system is formed by four sub-detectors:

- the **Scintillator Pad** (SPD).
- the **PreShower** (PS).
- the **Electromagnetic Calorimeter** (ECAL).
- the **Hadron Calorimeter** (HCAL).

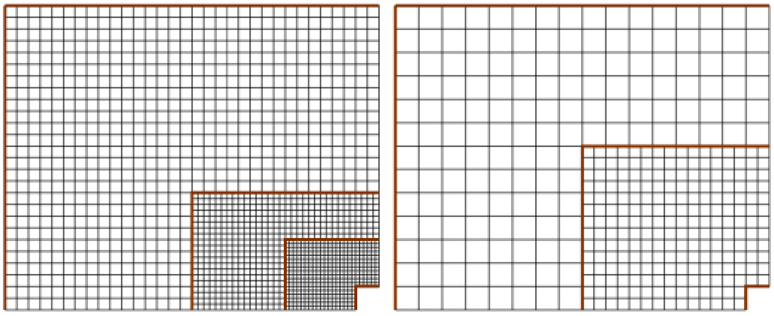

Figure 3.12: *Detectors layout (1/4). Left: ECAL. Right: HCAL.*

They are subdivided in four quadrants that surround the beampipe. Each quadrant has a lateral segmentation in cells of different sizes, depending on the distance from the beam axis. SPD, PS and ECAL have a common layout (Fig. 3.12 on the left hand side). Indeed, they are divided in three sections where the cells have different size: 4×4 cm in the inner region, 6×6 cm in the middle region and 12×12 cm in the outer one. This configuration is useful to cover the increasing occupancy near the beam line. The HCAL shares a similar layout(Fig. 3.12 on the right hand side), but it is divided only into two sections with tiles of 13×13 cm and 26×26 cm respectively. The read-out is common to all these detectors: scintillation light is transmitted to photomultipliers using wavelength shifting fibers.

SPD and PS The SPD is placed in front of the ECAL and the PS is placed after the SPD. In the middle there is a 15 mm lead absorber, corresponding to ~ 2.5 radiation lengths for electrons. They consist in two planes of scintillating pads, used at the low level electron trigger in order to reject background from charged and neutral pions and to improve electron identification. The SPD, just like a tracking detector, reveals only charged particles. Electrons and photons start showering in the lead absorber and produce on the PS a significantly larger signal than pions [37]. Hence electrons are the only particles that produce signals on both the SPD and PS, as visible in Fig. 3.13. SPD is also used at low level trigger to measure the number of tracks per event, in order to put a veto on the too crowded ones.

ECAL The ECAL is made of alternated 4 mm thick scintillators tiles and 2 mm thick lead plates. This thickness corresponds to about 25 radiation lengths, guarantees an almost complete electromagnetic shower containment and provides a good energy resolution of approximately $0.9\% \bigoplus (8\% \div 10\%)/\sqrt{E/\text{GeV}}$ [38].

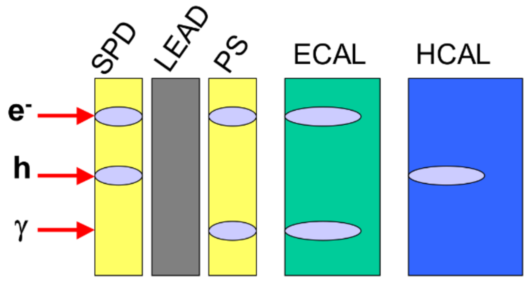

Figure 3.13: *Representation of energy deposit in each sub-detector of the calorimeter system.*

HCAL The HCAL is made of alternate 4 mm thick scintillators tiles sandwiched between 16 mm iron sheets, corresponding to about 5.6 interaction lengths with a resulting resolution of The HCAL resolution is $9\% \bigoplus 69\%/\sqrt{E/\mathrm{GeV}}$ [38]. This value is due to the poor thickness, that does not allow the complete shower containment and hence energy measurement. For this reason the HCAL is exploited only for trigger purposes and not for off-line analysis.

Muon detectors

The muons detector is composed of five stations (M1–M5) of rectangular shape, placed along the beam axis, designed to provide muons identification and fast measurement of their momenta for the low level trigger [39]. A sketch is shown in Fig. 3.14 on the left hand side. Each station consists of two mechanically independent halves, called A

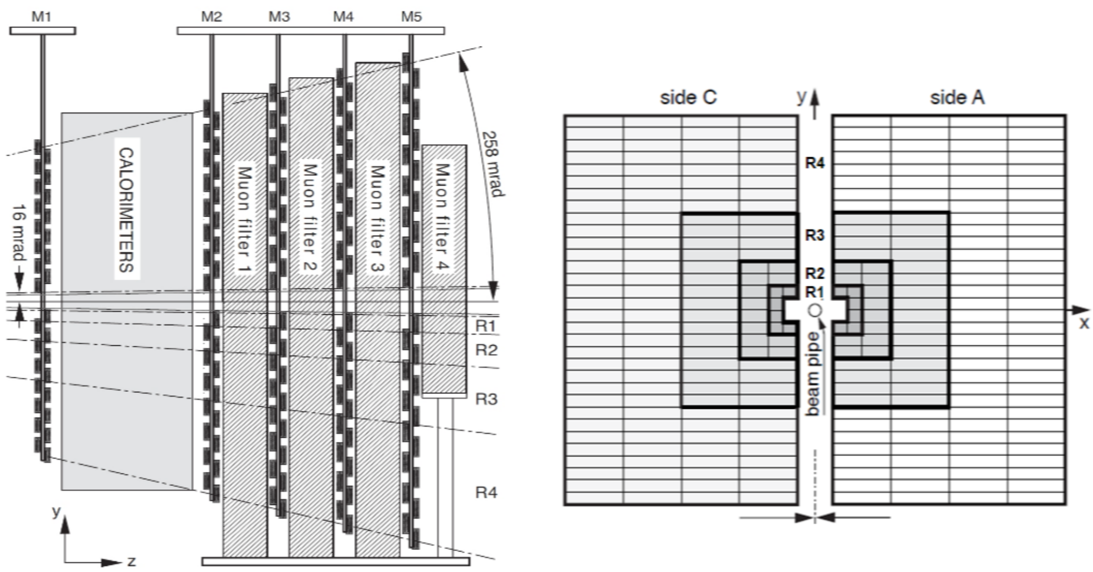

Figure 3.14: *Left: side view of LHCb muon detectors. Right: front view of M1 quadrant.*

and C sides, see Fig. 3.14 on the right hand, that can be horizontally moved in order to access to the beam pipe and to the detector chambers, for installation and maintenance. The first station, M1, is placed before the calorimeter system and it is only used to improve the transverse momentum[2](p_T) measurement in the trigger (the calorimeter

[2]The transeverse momentum of a particle is defined as the sum between the horizontal and vertical components of the momentum, $p_T = p_x + p_y$.

system, with its material budget, introduces errors due to multiple scattering). Stations M2 to M5 are placed downstream the calorimeters and are alternated with 80 cm thick iron absorbers, in order to select penetrating muons. In order to traverse the whole detector, the minimum momentum needed by a muon is about 6 GeV/c, since the total absorbers thickness (including calorimeters) corresponds to approximately 20 interaction lengths. Each station is divided into four segmentated regions R1-R4, whose cells scale in the ratio 1:2:4:8 with the distance from the beam axis. Since the dipole magnet provides bending in the horizontal plane, the logical pad segmentation of muon chambers is finer in the horizontal direction, x, than in the vertical direction, y, in order to allow a good estimate of the momentum. All stations use multiwire proportional chamber detectors, except for the R1 region of the first M1 station that uses triple gas electron multiplier detectors (triple-GEM): a more radiation tolerant detector is necessary because of the high particle density. In the trigger, muon reconstruction is performed by the stand alone muon system that achieves an average transverse momentum resolution of $\sim$ 20%.

3.5 LHCb Trigger

LHCb trigger is projected to efficiently select heavy flavor decays from the overwhelming QCD background from pp interactions [40]. At the nominal LHCb luminosity ($4 \cdot 10^{32}\mathrm{cm}^{-2}\mathrm{s}^{-1}$), over 200k $b\bar{b}$ pairs are produced every second. The charm cross-section is a factor 20 larger than the corresponding beauty cross-section, this means that reducing the output rate through the use of a trigger becomes essential not only for background rejection, but also to distinguish between different signals [41]. The LHC bunch-crossing rate is 40 MHz, however, only a limited rate of events can be written on storage: 5 KHz during Run 1 and 12.5 KHz in Run 2. It is also true that only a small fraction of the total rate is made of interesting events. The reduction of the rate is performed in two trigger level: Level-0 (L0), made of custom hardware trigger, and High Level Trigger (HLT), that run on a dedicated computer farm.

L0-Trigger: hardware trigger

The read-out of some sub-detectors cannot provides events at 40 MHz frequency, hence the task of the L0 trigger is to reduce the events rate to 1 MHz. In order to do this, it must exploit information from calorimeters and muon stations, as these are the only pieces of information available at such a high rate. The Level-0 trigger consists of three independent triggers that run in parallel exploiting the information of these sub-detectors.

L0Hadron It aims to collect b- and c-hadron enriched samples, taking information from the HCAL. Final state particles from such decays have on average higher transverse momenta than particles originated from light quark processes. This property helps in discriminating between signal and background: hadronic showers are identified in 2×2 clusters and their transverse energy is computed as

$$E_T = \sum_1^4 E_i \sin\theta_i \tag{3.5}$$

where E_i is the energy deposit in the i^{th} cell and θ_i is the angle between the z-axis and the nominal interaction point [42]. An event passes the trigger if there is at least one cluster with transverse energy over a certain threshold. This threshold was 3.46 GeV in 2017 but it has been changed over the years. The estimate rate of this trigger is 450 kHz.

L0Photon/Electron It takes information from SPD, PS and ECAL to identify electrons and photons. It selects events with at least one cluster with transverse energy $E_T > 2.47$ GeV if electrons and $E_T > 2.11$GeV if photons[3]. The estimate rate of this trigger is 150 kHz.

L0Muon/Dimuon It takes information from the muon stations and make an estimate of the muons momenta: the track direction is used to estimate the p_T of a muon candidate, assuming that the particle originated from the interaction point and received a single kick from the magnetic field. The trigger decision is based on the two muon candidates with the largest p_T: either the largest p_T must be above the `L0Muon` threshold ($E_T > 1.5$ GeV in 2017), or the product between the two largest p_T values must be above another certain threshold, `L0DiMuon`. The estimate rate of this trigger is 400 kHz.

High Level Trigger: software trigger

Events selected by L0 are transferred to the Event Filter Farm (EFF) where the High Level Trigger (HLT) performs a full reconstruction of the events through a C++ executable that runs in parallel on each processor of the farm. The HLT is divided into two stages, HLT1 and HLT2. The first level of the software trigger (HLT1) performs an inclusive selection, then the events are buffered to disk storage in the online system. This is done for two purposes: events can be processed further and the detector can be calibrated and aligned run-by-run before the HLT2 stage. Once the detector is aligned and calibrated, events are passed to HLT2, where a full event reconstruction is performed. The schematic process of the HLT is shown in Fig. 3.15.

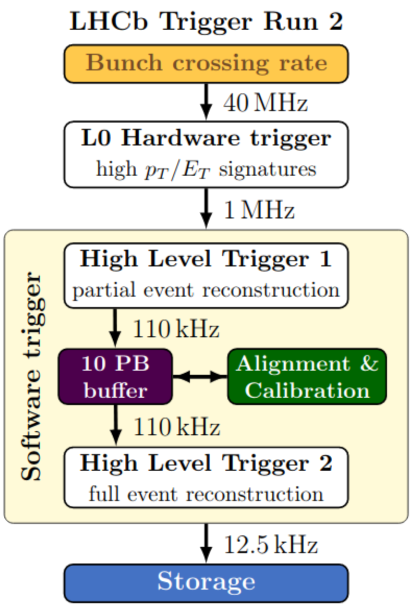

Figure 3.15: *Overview of LHCb trigger system[42].*

[3]Threshold relative to the 2017 data taking period.

HLT1 The HLT1 [42] processes the full 1 MHz event rate from the L0 trigger and performs a partial reconstruction in order to reduce it to about 110 kHz. Thanks to the information from the VELO, TT and T stations, HLT1 reconstructs the trajectories of charged particles with a p_T larger than 500 MeV/c, traversing the full LHCb tracking system (long tracks). Moreover, a precise reconstruction of the PV is performed. Thanks to the clean signature in the LHCb detector, muons identification can be performed already in HLT1, despite the tight timing constraints. An event passes this trigger cut if there is at least a track with good reconstruction quality and both impact parameter and transverse momentum over a certain threshold. Finally, all tracks are fitted in order to obtain the optimal parameter estimate.

HLT2 The HLT2 performs a full event reconstruction that consists of three major steps:

- Charged particles track reconstruction.
- Neutral particles reconstruction.
- Particle identification (PID).

At HLT2 stage the track reconstruction exploits the full information from the tracking sub-detectors, performing additional steps of the pattern recognition which are not possible in HLT1 due to tight time constraints. The HLT2 performs a full reconstruction very similar to the offline one, making few approximations, in order to achieve the requested final output rate. HLT2 is composed of inclusive (b-hadrons) and exclusive (c-hadrons) selections. Signals from c-hadrons are all fully selected by exclusive TURBO [42] trigger lines because around 10% of all 13 TeV pp collisions produce $c\bar{c}$ pairs and it is not possible to write all to offline storage. Exclusive TURBO trigger lines fully reconstruct relevant decays performing a selection of high-purity signals, enabling the candidates saved in the TURBO stream to be directly used by the analysts. Of the 12 kHz in Run 2, about 5 kHz belong to the TURBO stream and in particular also the data used in this analysis.

3.6 Event reconstruction and performances

Track reconstruction

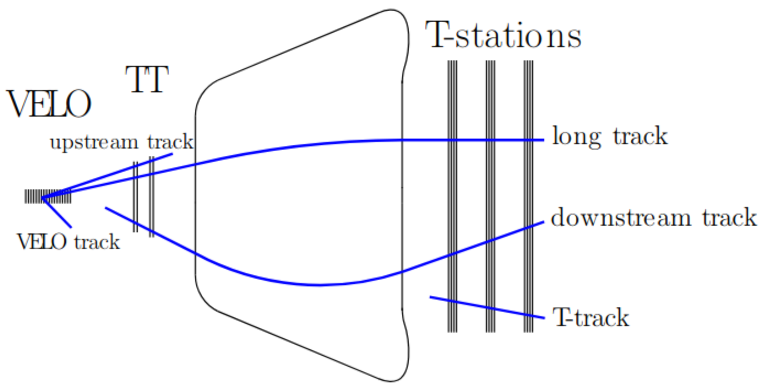

Figure 3.16: *Tracks classification at LHCb depending on the crossed sub-detectors.*

The term track in this kind of analysis stands for the trajectories of charged particles. The first step for the tracks reconstruction is the pattern recognition: hits produced by the same charged particles are identified. Different kinds of tracks can recognised at LHCb depending on the crossed sub-detector (see Fig. 3.16):

- **VELO tracks** are made with only VELO hits. These tracks are used for the primary vertex reconstruction.
- **Upstream tracks** exploit hits in the VELO and TT: low momentum tracks that are swept out by the magnetic field;
- **T tracks use only T-station hits**: exploit hits in the T-stations only.
- **Downstream tracks** are reconstructed exploiting TT and T-stations hits. They are generated by daughters of long-lived particles, such as K^0_S that often decay outside the VELO.
- **Long tracks** are reconstructed with hits from VELO, TT and T-stations; these kind of tracks have the best momentum resolution.

The resolution on long tracks varies from $\sigma_p/p = 0.5\%$ below 20 GeV, to 1% at 200 GeV [42]. For what concerns the primary vertex (PV) resolution, it depends heavily on the number of tracks originating from the vertex.

Particle identification

As seen before, particle identification in LHCb is achieved exploiting different sub-detectors: Cherenkov angle measured in the RICH detectors is combined with the momentum measured by the tracking system to infer the mass of the particle, see Eq. 3.4. The identification starts from the hits in the MUON stations that are searched in different regions as function of the momentum of the muon candidate. Tracks with $p < 3$ GeV cannot be identified as muons: they would not be able to reach the MUON stations. Below a momentum of 6 GeV, the muon identification algorithm requires hits in the first two stations after the calorimeters. Whereas, if $6 < p < 10$ GeV, an additional hit is required in one of the last two stations. Finally, above 10 GeV, hits are required in all the four MUON stations. In order to identify photons, electrons and π^0 candidates the calorimeter system is used, neutral particles are distinguished from charged ones thanks to the presence or absence of tracks in front of the energy deposits. The discrimination between photons and π^0 mesons is performed looking at the shape of the cluster. The particle identification (PID) information is obtained combining all the information from the MUON station, the RICH and the calorimeter system, in order to provide a more powerful identification. Each sub-system gives a likelihood information for a certain particle hypothesis, $\mathcal{L}(X)$. Since pions are the most abundant species produced and detected at LHCb, the particle identification in usually calculated with respect to the pion hypothesis, $\mathcal{L}(\pi)$. The difference between the logarithms of two likelihoods (DLL) with the X and the π hypothesis is computed as $\mathrm{PID}_X \equiv DLL_{X\pi} = log\mathcal{L}(X) - log\mathcal{L}(\pi) = log\left[\frac{\mathcal{L}(X)}{\mathcal{L}(\pi)}\right]$. It immediately follows that the larger the PIDX value is, the more likely is that the the particle belongs to the X species, rather than being a pion.

4

Candidates selection and reconstruction

This chapter describes the topology of the $D^0 \to K^0_S K^\pm \pi^\mp$ decays, and how they are reconstructed and selected within the LHCb experiment. The data sample, in output to the LHCb data acquisition and trigger systems, is presented as the starting point of the analysis work presented in this thesis.

4.1 The data sample: $D^0 \to K^0_S K\pi$ decays

The present study uses the data sample recorded by the LHCb experiment, from 2016 to 2018 (LHC Run 2) at center-of-mass energy $\sqrt{s} = 13$TeV. The total integrated luminosity, during this data taking period, is about ~ 5.6 fb^{-1}: 1.67 fb^{-1} in 2016, 1.71 fb^{-1} in 2017 and 2.19 fb^{-1} in 2018. The subject of this thesis is the study of the $D^0 \to K^0_S K^\pm \pi^\mp$ and $\overline{D}^0 \to K^0_S K^\pm \pi^\mp$ decay channels coming from the events $D^{*+} \to D^0 \pi^+$ and $D^{*-} \to \overline{D}^0 \pi^-$, where the charge of the pion determines the flavour of the D^0, as explained in Sect. 1.6. Since the D^* decays occurs via strong interaction, it is practically instantaneous with respect to the vertex resolution. Hence, the D^0 is considered to be produced in the same place as the D^*. The Q-value[1] of the decay is small ($\sim$ 6 MeV/c) if compared to the pion mass, thus the D^0 and the π are almost collinear to the D^* flight direction in the laboratory frame. This is why the resolution of the D^* vertex is poor. Moreover, the small Q-value makes the pion produced in the D^* decay having small momentum, for this reason it is known as “soft” pion (π_S). The final states are $K_S K^\pm \pi^\mp$, for both the D^0 and $\overline{D}^0$ particles and, depending on the charge of the pion from the D^0 decay, it is possible to distinguish two sub-sets, as explained in Sect. 2.3. If the pion has the same charge of the soft pion the sub-set is called right-sign (RS), instead the wrong-sign (WS) sub-set is the one in which the charge beetween the two pions is different, as one can see from the sketch in Fig. 4.1. Another sub-sample classification is determined by the type of the track of the K^0_S that is a long lived particle compared to the LHCb detector distances and it often decays in a pair of pions ($\sim 70\% BR$) outside the vertex detector. Therefore, long (L) and down (D) sub-samples are distinguished (Sect. 3.6). The L sample stands for events in which the K^0_S is reconstructed through a pair of long tracks, instead

[1] It is defined as the difference between the mass of the mother particle and the sum of the masses of the particles in the final state, hence it is the available kinetic energy of the final state.

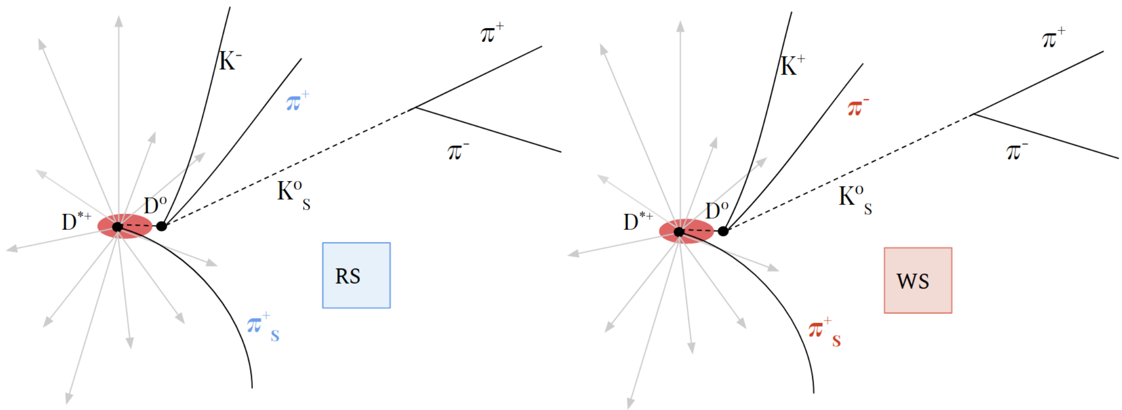

Figure 4.1: *Sketch of the signal decay topology. On the left the two pions labelled in blue has the same electric charge (RS decay). Instead, on the right hand side, the two pions labelled in red has an opposite electric charge (WS decay).*

the D sub-sample stands for the K^0_S reconstructed with a pair of downstream tracks. In particular the L sample has the best quality tracks but it corresponds to only $\sim 1/3$ of the total data sample. Two more subset are determined by the polarization of the magnet of LHCb, because it change during the run, as explained in Sect. 3.3. The magnetic field can follow the y direction (MagUp) or $-y$ direction (MagDown). Therefore the data-set used in this analysis is divided in 24 subsamples: {WS, RS}{L, D}{MagUp, MagDown}{2016, 2017, 2018}

4.2 Nomenclature and tracking variables definitions

It is useful to define the relevant tracking variables used in the present analysis.

Primary Vertex (PV) It is the vectorial position of the reconstructed primary pp interaction. In the cases where it is important to stress the vectorial nature, it will be written $\overrightarrow{PV}$.

Decay Vertex (DV) It is the vectorial position of the reconstructed point where a certain particle X is decayed. In the cases where it is important to stress the vectorial nature, it will be written $\overrightarrow{DV}(X)$. In this analysis, if X is not specified it is referred to the DV of the D^0 particle.

Preudorapidity (η) It is defined as $\eta = -\log(\tan\theta/2)$. It is just another way to parametrize the θ angle with respect to the z-axis. It is widely used in particle physics because, in the limit of ultra-relativistic particles, the pseudorapidity approximates the rapidity, hence it is Lorentz invariant for boosts in the z direction.

$\boldsymbol{\theta_{DIRA}}$ It is the direction angle, i.e. the angle between the momentum of the particle and the displacement vector, defined by the PV and the DV of the particle.

Impact Parameter (IP) Distance of closest approach to a particle trajectory to a given point. D^0 daughters have in general large impact parameters with respect to the PV because of the displaced decay vertex of the D^0 meson. Instead, the IP of the D^0 meson with respect to the PV tends to be close to zero within the experimental uncertainty, in the assumption of "prompt" decays (i.e. coming from the PV).

Impact Parameter Chi square (χ^2_{IP}) Difference between the χ^2 of the primary vertex fit, obtained with and without considering the particle in the fit. If the particle does not come from the PV, the χ^2_{IP} will be generally larger than the one obtained with a prompt particle.

Flight Distance (FD) Distance travelled by a particle from the production point to the DV.

Flight Distance Chi square (χ^2_{FD}) It is the fit χ^2 to distance between PV and DV of the particle, i.e. a measurement of the significance of the displacement vector to be different from zero.

Proper decay time (t) It is computed from the following relation:

$$FD = ct\beta\gamma = \frac{|\overrightarrow{p}|}{m}ct \tag{4.1}$$

where c is the speed of light, $\overrightarrow{p}$ is the particle momentum, m is its mass and t is its proper decay time.

Particle identification (PID$_K$ on X) it is computed through the difference between the logarithm of the likelihoods in the K and the π hypothesis. An high value of PID$_K$ means an high probability for a particle X to be a kaon (see Sect. 3.6).

Track ghost probability ($\mathcal{P}_{ghost}$) It is the probability for a track to be a "ghost"track, i.e. a misidentified track. This quantity is calculated with a Neural Network [43], that combines information from different variables which describe the track reconstruction and global event properties in order to separate ghost tracks, which are spurious combination of hits, from real tracks.

Decay Tree Fitter (DTF) Algorithm used to refit all the candidates offline. The algorithm takes a complete decay chain, parameterizes it in terms of vertex positions, decay lengths and momentum parameters. Then, it fits these parameters simultaneously, taking into account constraints such as measured parameters and 4-momentum conservation at each vertex [44]. In this thesis, when the subscript DTF will be used, it will imply that the constraint on the D^0 and on the soft pion to come from the primary vertex was required.

Δm In this analysis it is the difference between the D^* and the D^0 masses obtained using the DTF algorithm. The Δm distribution has a starting point for the pion mass value (139.57 MeV/c^2). In the difference, part of the uncertainties on the D^0 mass cancels out, allowing Δm to have a much better mass resolution than D^* mass.

Vertex fit χ^2/ndf It is the χ^2 value of the vertex fit, normalized to the degrees of freedom. The fitter takes as input a vector of particles, performs the fit and updates the mother particle [45].

Trigger On Signal (TOS) events that are triggered on the signal decay chain, i.e. one of the particles in the decay chain fires a certain line of the trigger.

Trigger Partially on Signal (TPS) events that are triggered if they are partially contained within the signal decay chain.

Trigger Independent of Signal (TIS) events that are triggered independently of the presence of the signal, i.e. the trigger is fired by other random particles in the events.

4.3 L0 trigger selection

The L0 trigger is designed to select b- and c-hadron events (`L0Hadron`) and its decision is based on the value of the transverse energy of reconstructed clusters, $E_T \geq 3.7$ GeV. This threshold is high with respect to the HLT2 requirement on the transverse momentum of the D^0, $p_T > 1\text{GeV}/c$, because `L0Hadron` is designed to select rare events.
In the present analysis, the `L0Global` (logic `OR` between all the L0 trigger lines) is required to be TIS on the D^* signal. The motivation of this choice is explained in Sect. 5.2. This requirement retains about the 85% of the total amount of collected data.

4.4 HLT1 selection

At the HLT1 level, it is required that at least one of daughter particles fired the `Hlt1TrackMVA` line or, alternatively, that the combination of the two particles, fired the `Hlt1TwoTrackMVA` line. The requirements made by these trigger lines aim to select respectively one or two detached high-momentum good-quality Long tracks, in order to identify B and D meson decays independently from which L0 trigger line fired. The following sub-sections describe the HLT1 trigger requirements in order to assure the good-quality of the tracks. The list of the cuts is summarized in Tab. 4.1.

TrackMVA

The `Hlt1TrackMVA` trigger line selects a single track in the event. In order to ensure its quality:

- Long tracks with a minimum number (9) of hits in the VELO are selected.
- The track fit satisfy a $\chi^2/ndf < 2.5$.
- The $\mathcal{P}_{ghost}(h^{\pm})$ should be less then a certain threshold, where $h^{\pm}$ identifies the $K^{\pm}$ or $\pi^{\pm}$ product of the D^0 decay. The threshold of this cut varied in data acquisition time, from 0.4 to 0.2.
- The momentum $p(h^{\pm})$ is required to be over a certain threshold that varied with the data acquisition time. Most of the data-set were selected with $p(h^{\pm}) > 5$ GeV$/c$.
- The tracks of the $K^{\pm}$ and $\pi^{\mp}$ from the D^0 are required to be displaced with respect to the PV (they must come from the DV of the D^0).

The latter statement is ensured, together with a further request on an higher momenta, though a multivariate cut involving the $p_T(h^{\pm})$ and $\chi^2_{IP}(h^{\pm})$:

$$\begin{gathered}\left\{p_T > 25 \wedge \chi^2_{IP} > 7.4\right\} \\ \vee \\ \left\{[1 < p_T < 25] \wedge \left[\ln \chi^2_{IP} > \ln 7.4 + \frac{1}{(p_T - 1.0)^2} + \alpha\left(1 - \frac{p_T}{25}\right)\right]\right\}\end{gathered} \tag{4.2}$$

where the p_T is expressed in GeV$/c$ and the value of the α parameter has been changed during the data acquisition time. In particular, the values that α assumes and the selected regions on the χ^2_{IP}-p_T plane are reported in Fig. 4.2.

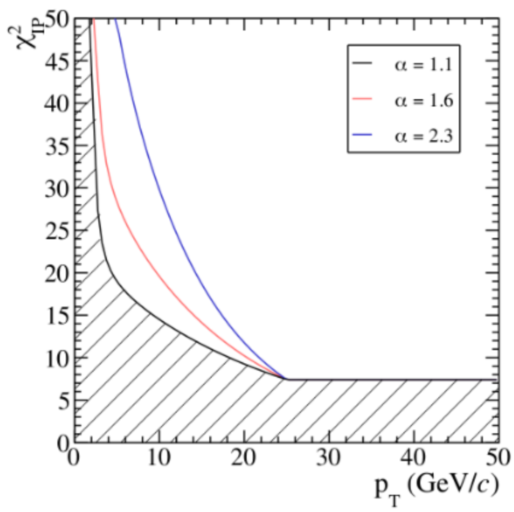

Figure 4.2: *Boundaries of the selected region in the track $\chi^2_{IP} - p_T$ plane for the Hlt1TrackMVA line. The shaded area represents the excluded region with the $\alpha = 1.1$ requirement.*

TwoTrackMVA

The `Hlt1TwoTrackMVA` trigger line is designed to select a combination of two good quality Long tracks. They satisfy the hypothesis of coming from the same DV of a particle significantly displaced from the PV, and to have high transverse momentum once they are combined to form a single particle. The first condition is satisfied thanks to the cut applied on the two tracks vertex fit χ^2 (Vertex fit $\chi^2/ndf < 10$). Instead, the condition on the transverse momentum is enforced considering the output of a multivariate proprietary classifier by Yandex[43] in order to select good quality two-tracks vertex. It takes in input the following variables:

- χ^2 distance between the PV and the two-tracks vertex (a.k.a. χ^2_{FD});
- sum of the p_T of the two tracks, $p_T(h^+) + p_T(h^-)$;
- number of tracks satisfying $\chi^2_{IP} > 16$;
- χ^2 of the vertex fit of the two tracks;

The cut applied on the output of the classifier and the threshold has been varied along the data acquisition. Quality and momentum cuts are the same of the single tracks trigger `Hlt1TrackMVA`. Whereas, the transverse momentum and the χ^2 of the impact parameter have rectangular selections ($p_T > 0.5, 0.6$, depending on the acquisition time and $\chi^2_{IP} > 4$). In addition to those requests on decay products, other constraints on their combinations are added, as illustrated in Tab. 4.1. Among the various the cuts, the corrected mass ($m_{corr}(h^+h^-)$) appears. It is defined as $m_{corr}(h^+h^-) := \sqrt{m^2 + p^2_{Tmiss}} + |p_{Tmiss}|$, where p_{Tmiss} is the missing transverse momentum. This variable is useful for decays with undetected (e.g. out of the acceptance) or undetectable (e.g. semileptonic decays) particles, in order to find a better approximation of the mass of the mother particle [11]. In the $D^0 \to K^0_S K\pi$ case, the corrected mass will be equivalent to the invariant mass, within the experimental resolution. Therefore, the requirement $m_{corr}(h^+h^-) > 1$ GeV/c^2 holds because the D^0 mass (m(D^0)= 1864 MeV/c^2) is greater than the value of the threshold.

Table 4.1: *Summary of the Hlt1 selection requirements. Since some thresholds was varied during the LHC Run 2 data taking, two requirements values can appear in the table. $h^\pm$ stands for the $K^\pm$ or $\pi^\pm$ from the D^0 decay.*

Candidate	Variable	HLT1		Units
		TrackMVA	TwoTrackMVA	
$h^\pm$	track χ^2/ndf	< 2.5	< 2.5	-
	$\mathcal{P}_{ghost}$	$< 0.4, 0.2$	$< 0.4, 0.2$	-
	p	$> 3, 5$	$> 3, 5$	GeV/c
	p_T	see Eq. 5.4	$> 0.5, 0.6$	GeV/c
	χ^2_{IP}	see Eq. 5.4	> 4	-
D^0	$\eta(\overrightarrow{DV} - \overrightarrow{PV})$	-	$\in [2, 5]$	-
	$m_{corr}(h^+h^-)$	-	> 1	GeV/c^2
	Output of the classifier	-	$> 0.95, 0.97$	-
	p_T	-	> 2	GeV/c
	Vertexfit χ^2/ndf	-	< 10	-
	$\cos\theta_{DIRA}$	-	> 0	-

4.5 HLT2 selection

The Hlt2 selection criteria are listed in Tab. 4.2. The particles that pass these selection are later combined to form a D^0. At this stage, the aim of the trigger is to select two pair of tracks which made a good vertex, far from the PV ($\chi^2_{IP} > 36^L$). Then the two particles are identified as pions or kaons according to the PID_K (< 5 for the pions and > 5 for the kaons). If the pair of particles is identified as the daughter pions of the K^0_S, it is required an invariant mass compatible with that of the K^0_S. The invariant mass of the D^0, $m(K^0_S K\pi)$, reconstructed using the K^0_S, K and π particles, has to be within a window around the nominal D^0 mass (1863.83 MeV/c^2). Requirements on the quality of the D^0 track are listed in Tab. 4.2, such as the χ^2 of the fit to the D^0 and K^0_S vertex ($\chi^2/ndf < 20$ and < 30, respectively) and a constrain on the D^0 to come from the PV ($\theta_{DIRA} < 34.6$ mrad). Furthermore, some requirements on the p and p_T of the soft pions are applied in order to reject the background. For what concerns the D^*, reconstructed through the four tracks combination (π_s, K^0_S, K, π), the vertex fit is required to be less than 10 (Vertex fit $\chi^2/ndf(D^*)$) and the reconstructed invariant mass, m($K^0_S K\pi\pi_s$), has to be in a range around the known D^* mass (2010.27 MeV/c^2). The latter requirement is imposed using the Δm, in order to exploit its better invariant mass resolution.

The final distributions obtained applying the HLT2 requirements are shown in Fig. 4.3, where the D^0 invariant mass distribution is displayed on the left hand side, while that one of Δm invariant mass on the right hand side. Although, the trigger system requires

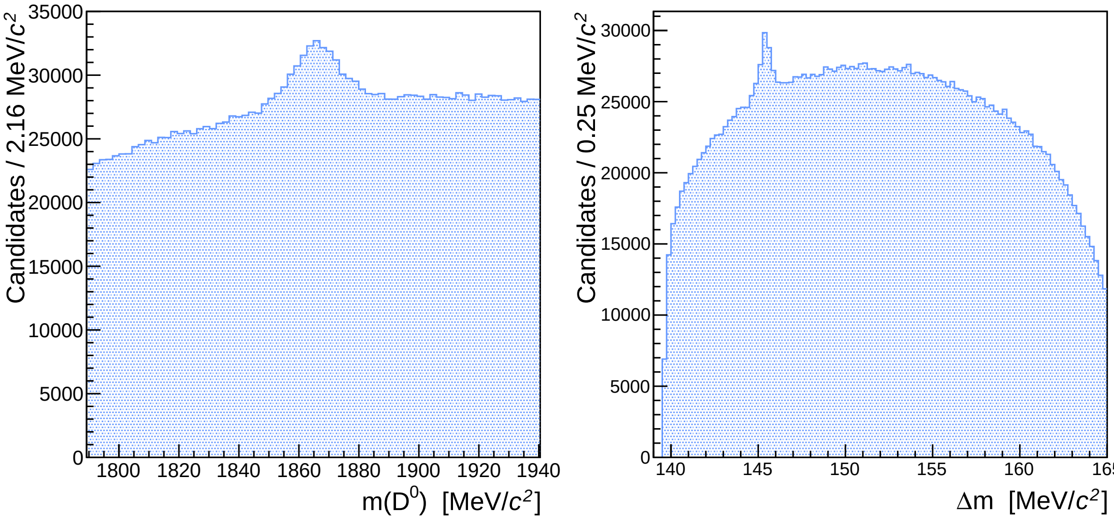

Figure 4.3: *The D^0 mass and Δm plots respectively on the left and on the right hand side. Distributions obtained after the trigger selections. 1/10 of the WS, magnet down, Long, 2016 sample is used.*

already very stringent criteria, the purity of the sample is not so good to allow a physics analysis. A further process of optimization of the selection is, therefore, necessary. This is the main subject of the next chapter.

Table 4.2: *Hlt2 selection requirements. $h^{\pm}$ stands for the charged particles from the D^0 decay, the K and π. The superscripts L or D specify the type of track to which the requirement is applied. The superscripts '16, '17 and '18 stand for the year in which a certain threshold is chosen. If it is not specified any kind of superscript, the requirement is on both the types of tracks and the threshold is the same all over the data taking period.*

Candidate	Variable	HLT2 Requirement	Units
$\pi^{\pm}$ of K^0_S	Track χ^2/ndf	$< 3^L$	-
		$< 4^D$	-
	χ^2_{IP}	$> 36^L$	-
	p	$> 3^D$	GeV/c
	p_T	$> 175^D$	MeV/c
K^0_S	$\lvert m(\pi^+\pi^-) - m^{PDG}_{K^0_S}\rvert$	$< 35^L$	MeV/c^2
		$< 64^D$	MeV/c^2
	Vertex-fit χ^2/ndf	< 30	-
	Decay time wrt primary vertex	$> 2^L$	ps
		$> 0.5^D$	ps
	z position of the vertex	$[-0.1,0.5]^L$	m
		$[0.4, 2.275]^D$	m
$h^{\pm}$ of D^0	Track χ^2/ndf	< 3	-
	$\mathcal{P}_{ghost}$	< 0.4	-
	p	> 1	GeV/c
	p_T	> 200	MeV/c
	IP χ^2	> 4	-
	PID$_K$	< 5 $\pi^{\pm}$	-
		> 5 $K^{\pm}$	-
D^0	Mass	[1.765, 1.965]	GeV/c^2
	Vertex-fit χ^2 /ndf	< 20	-
	p_T	> 1.8	GeV/c^2
	θ_{DIRA}	< 34.6	mrad
	Decay time	> 0.1	ps
	Flight-distance χ^2	< 20	-
π_s	Track χ^2/ndf	< 3	-
	$\mathcal{P}_{ghost}$	$< 0.4^{'16}, 0.25^{'17,'18}$	-
	p	> 1	GeV/c
	p_T	$> 100^{'16}, 200^{'17,'18}$	MeV/c
D^*	Vertex-fit χ^2/ndf	< 10	-
	Δ m	[135, 165]	MeV/c^2

5

Offline selection optimization

This chapter describes the final set of offline requirements, and how they are chosen in order to maximize the statistical sensitivity of the A_{CP} measurement. Finally, the signal yields for the $D^0 \to K_S^0 K^\pm \pi^\mp$ RS and WS data samples are determined.

5.1 Introduction

In order to perform a reliable cancellation between signal ($D^0 \to K_S^0 K\pi$) and calibration ($D^0 \to K_S^0 \pi\pi$) modes (Sec. 2.3), it is essential to equalize the kinematics of the two data samples, applying, when it is possible, the same offline selection, in order to avoid the onset of spurious asymmetries. It is also important to account for the kinematics of the two-body decay modes, $D^0 \to K^-\pi^+$ and $D^0 \to \pi^+\pi^-$, that are necessary to determine the nuisance asymmetry term $A_D(K\pi)$.

With this aim, an accurate selection of Level-0 and HLT1 trigger requirements is chosen at first. Further cuts are applied to reject the main backgrounds and equalize different HLT2 trigger requirements among the signal and the calibration samples ("baseline cuts"). Finally, all the thresholds are optimized, in order to improve the statistical uncertainty on the A_{CP} measurement. Hence, this chapter focuses on :

- the choice of the Level-0 and HLT1 trigger decisions, and of the baseline cuts;
- the reduction of the statistical uncertainty on the measurement of interest, A_{CP}, through an optimization process.

Once the offline selection is determined, the rejection of the multiple candidates is performed. All those events where more than one soft pion is associated to the same D^0 candidate, are removed from the final sample. Finally, both the RS and WS signal yields are determined. A very similar offline selection is then applied to the $D^0 \to K_S^0 \pi\pi$, $D^0 \to K\pi$ and $D^0 \to \pi\pi$ control modes.

5.2 Trigger requirements

The data sample displayed at the end of the previous chapter, is the inclusive output of the trigger system, with no further offline requirements. However, as explained above,

Table 5.1: *Data fraction after trigger decisions.*

Requirements	Data Fraction
1 `L0Global` TIS on D^*	$\sim 85\%$
2 `HLT1TwoTrackMVA` TPS on $(K \wedge \pi) \vee$ `HLT1TrackMVA` TOS on $(K \vee \pi)$	$\sim 73\%$
1 $\wedge$ **2**	$\sim 62\%$

the analysis relies on the cancellation of nuisance asymmetries among different data samples, the $D^0 \to K^0_S K\pi$ as signal decays, and $D^0 \to K^0_S \pi\pi$, $D^0 \to K\pi$ and $D^0 \to \pi\pi$ as calibration decay modes. Therefore, it is crucial to equalize trigger requirements in order to avoid to have spurious detection asymmetries in some samples, and not in other data samples. For this reason the final choice of Level-0 and HLT1 requirements is inspired to the principle that the soft pion and the K^0_S decay products do not have to enter the trigger decision.

Table 5.1 summarizes the trigger decisions and the remaining data fractions. At Level-0 the `L0Global` (logic `OR` between all the `L0` triggers lines) is required to be TIS on D^* signal. After this requirement, the 85% of the total sample is kept. This is a conservative choice, since in principle one may consider also to use the `L0Hadron` TOS decision on the pair $K\pi$. However, this adds possible complications due to the presence of multiple trigger decisions with different kinematics, especially in the comparison with the two-body calibration decay modes. The Hlt1 selection, instead, acts on the pair $K\pi$. It requires the TPS of the `TwoTrackMVA` on the K and on the π from the D^0 decay. The logic AND between the TPS K and the TPS π requirements is applied, in order to ensure that the two particles that fire the line are the daughters of the D^0 meson. Moreover, it requires the TOS of the `TrackMVA` on the K and on the π from the D^0 decay, in particular the logic OR between the TOS K and the TOS π is required. Finally, the logic OR between the `TwoTrackMVA` and the `TrackMVA` requirements is chosen, in order to save as much as possible candidates where the Hlt1 trigger lines are fired because of the K and π D^0 daughters. Trigger decisions involving the K^0_S decay products are not chosen, in order to minimize possible differences with the $D^0 \to K\pi$ and $D^0 \to \pi\pi$ decay modes.

The comparison between the samples where the trigger requirements are applied and the previous case without any requirements on trigger decisions (see Fig. 4.3), is shown in Fig. 5.1. The $m(D^0)$ distribution is on the left hand side, whereas on the right there is the Δm distribution. In order to quantify the purity of the sample we calculate the value of the figure of merit $S/\sqrt{S+B}$ under the signal peak[1], for the invariant Δm mass distribution where the trigger decision is applied. The value returns to be 27.43.

5.3 Baseline selection

Some further requirements are applied in order to reduce the main physics backgrounds and to equalize kinematics of signal and calibration samples. The cuts are summarized in Tab. 5.2 and a brief description and justification are given below.

***D^0* lifetime and *D^0* IP χ^2:** It suppresses the contamination of secondary $B \to D^* X$ decays, i.e. the D^* decay candidates not coming from the interaction point. These are standard cuts in LHCb for this type of decays.

[1]This figure of merit will be precisely defined in Sec. 5.4.

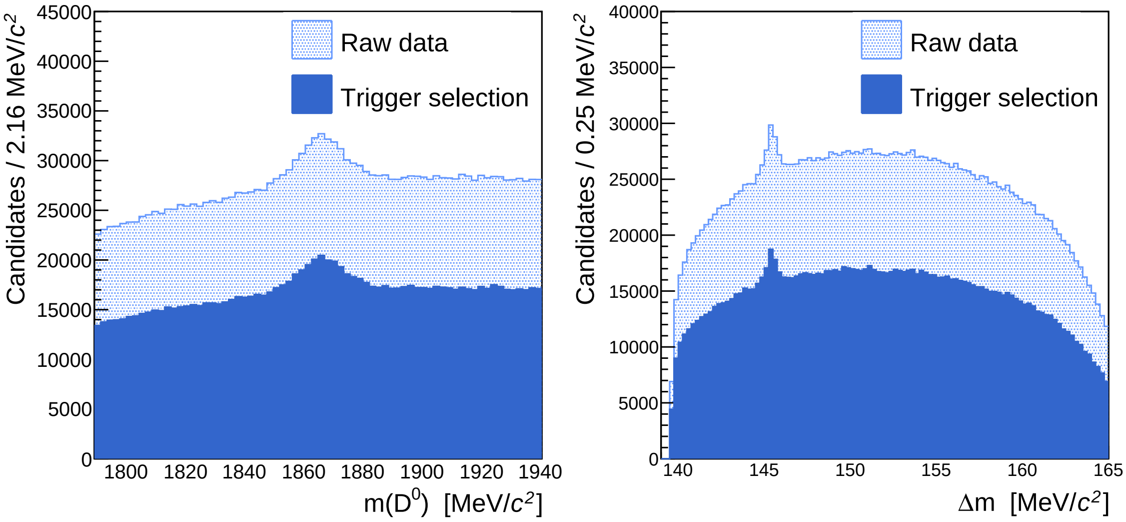

Figure 5.1: *The invariant D^0-mass and the invariant Δm-mass distributions are displayed on the left and on the right, respectively. Comparison between the initial sample and the sample after the application of the offline trigger decisions. It is used just 1/10 of the WS, magnet down, Long, 2016 sample.*

Table 5.2: *Baseline cuts.*

Candidate	Variable	Requirement	Units
D^0	Lifetime wrt best PV	$[0.3, 8]\tau$	-
	χ^2_{IP}	< 9	-
$K^\pm\pi^\mp$ of D^0	PID_K	$< -5\ \pi^\pm$	-
	p	> 5	GeV/c
	p_T	> 800	MeV/c
	η	$[2, 4.2]$	-
K^0_S	mass	$[485, 510]$	MeV/c^2
	$\log(\chi^2_{FD})$ wrt origin vertex	> 5	-
$\pi^\pm$ of K^0_S	η	$[2, 4.2]$	-
π_s	p_T	> 200	MeV/c
	$\mathcal{P}_{ghost}$	< 0.25	-

PID$_K$ on $\pi^\pm$ This is used in the two-body samples to reduce the contamination of reconstructed D^0 candidates where one (or two) decay product is misidentified. It also used in the three-body decay modes in order to equalize all the samples.

p, p_T of the D^0 daughters $K^\pm\pi^\mp$ The two-body control modes have tighter cuts at Hlt2 ($p > 5000$ MeV$/c$ and $p_T > 800$ MeV$/c$) with respect to the three-body decay modes, because the momentum of the involved particles are usually higher. Therefore, these requirements are equalized between signal and calibration modes. This results in a drop of the signal events of about 15%.

η of the tracks $\pi^\pm$ from the K^0_S and $K^\pm\pi^\mp$ from the D^0 These cuts are applied in order to reduce the detection asymmetry due to the interactions with the detector material. Figure 5.2 shows the amount of material in the tracking system, given in terms of hadronic interaction lengths (λ_I) versus η.

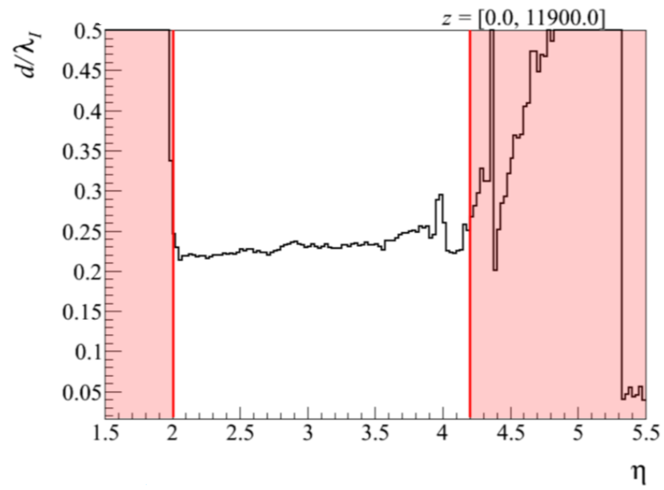

Figure 5.2: *Distance in hadronic interaction length, λ_I versus η [46]. The peak at $\eta = 4.38$ comes from the 25 mrad conical beam pipe inside RICH1. The red shaded areas represent the excluded region.*

K^0_S mass The invariant K^0_S-mass is required to belong to an interval of 2σ around the nominal m(K^0_S) value. This requirement suppresses the combinatorial background in the invariant K^0_S mass spectrum.

K^0_S flight distance χ^2 This requirement is useful to suppress the background given by the decay $D^0 \to K^-\pi^+\pi^+\pi^-$, where the invariant mass of a $\pi^+\pi^-$ pair is close to the nominal value of K^0_S mass, as shown in Fig. 5.3.

p_T and $\mathcal{P}_{GHOST}$ of π_s These cuts are necessary to equalize the HLT2 selection over all data taking years (2016-2018).

The resulting data sample, after the application of the baseline selection, is shown in Fig. 5.4. The comparison with the sample obtained after the trigger requirements is also displayed. Also in this case, it is possible to quantify the purity of the sample

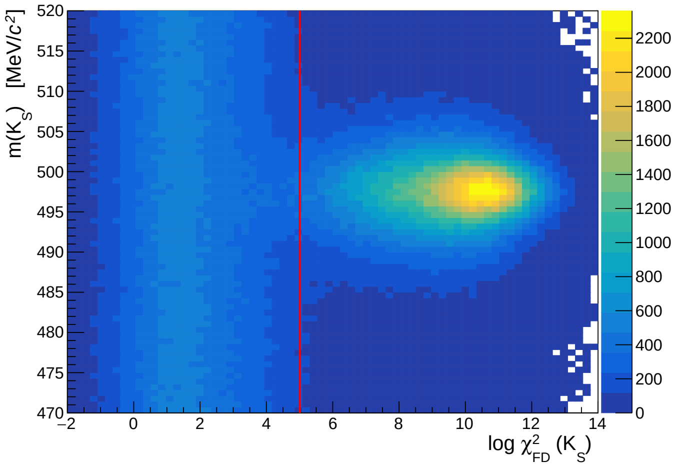

Figure 5.3: *2D distribution of the $m(K^0_S)$ and $\log \chi^2_{FD}(K^0_S)$. The vertical red line stands for the cut $\log \chi^2_{FD}(K^0_S) > 5$.*

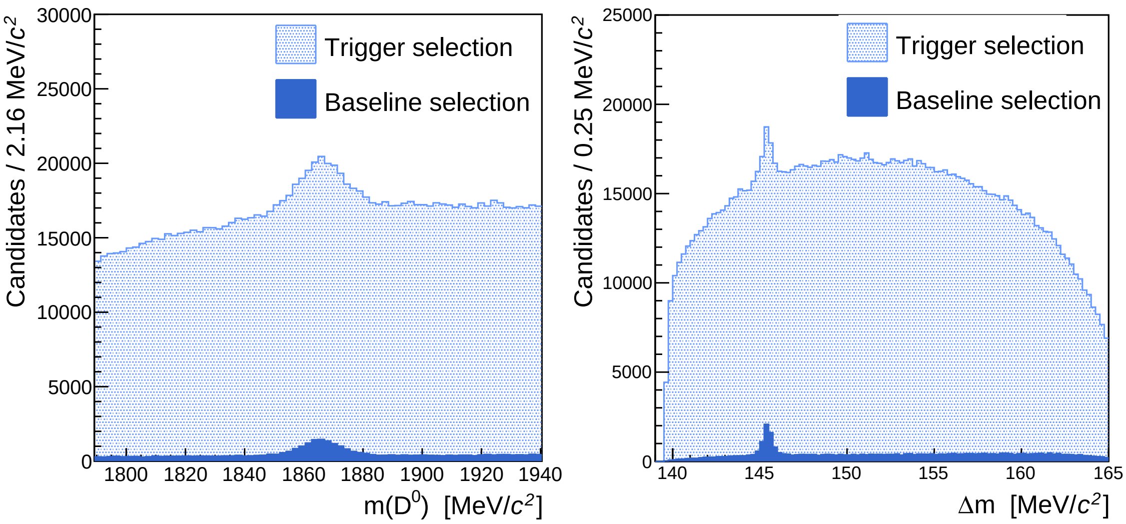

Figure 5.4: *The distribution of the invariant D^0-mass and Δm-mass are shown on the left and on the right, respectively. Comparison between the sample obtained after the only application of trigger requirements and the additional application of the baseline selection is also shown. It is used 1/10 of the WS, magnet down, Long, 2016 sample.*

by calculating the value of the figure of merit $S/\sqrt{S+B}$ under the signal peak for the invariant Δm mass distribution. The value returns to be equal to 55.92, to be compared with the previous value obtained without the application of the baseline requirements 27.43.

The baseline selection largely increases the purity of the sample, however it can be further improved by exploiting the separation power of the invariant masses, that has not been used so far. Hence, selecting a 3σ region from the mean value of the D^0 invariant mass distribution ($m(D^0) \in [1832.43, 1897.23]$ MeV$/c^2$, see Sect. 5.4), it is possible to increase the $S/\sqrt{S+B}$ value for the D^*-tagged signal candidates. Figure 5.5 shows the

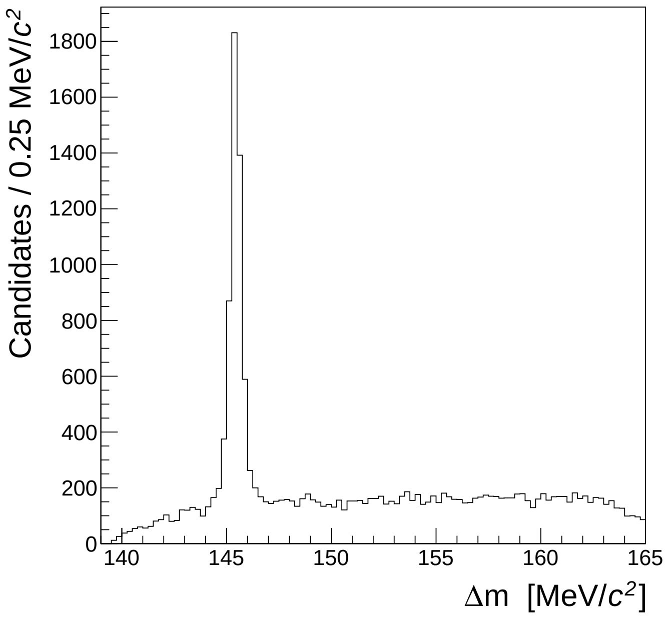

Figure 5.5: *The distribution of the Δm invariant mass is shown. The baseline selection and the additional requirement $m(D^0) \in [1832.43, 1897.23]$ are applied.*

invariant Δm mass after the application of this further requirement. The $S/\sqrt{S+B}$ value moves from 55.92 to 60.59, by increasing by a factor of 1.08.

5.4 Selection optimization: the general strategy

In order to further improve the statistical uncertainty on the A_{CP} measurement, the offline selection can be further optimized. The optimal cuts configuration can be found using the standard score function $\mathcal{R}$,

$$\mathcal{R} = \frac{S}{\sqrt{S+B}}, \tag{5.1}$$

where S and B are the number of reconstructed signal and background candidates, respectively [2]. The score function $\mathcal{R}$ is linked to the statistical uncertainty on the A_{CP} measurement, in particular the maximum value of $\mathcal{R}$ corresponds to the minimum statistical uncertainty. The optimal approach would be to simultaneously study many variables at the same time to account for the correlations. Therefore, one would desire to

[2] The regions where S and B are counted are defined in detail in the next section.

scan a space with a very high number of dimensions: "n" observables (x_1, x_2, ..., x_n) and "m" bins for each variable. This translates into a total number of m^n fits to the Δm mass, in order to evaluate S and B for each configuration. However, if m and n are not small, this computation can be very intensive both from CPU and memory usage. Standard computer resources, of a commercial workstation, are usually not enough to finely scan a multi-dimensional space, too much information needs to be stored. In addition, a fit to the invariant mass for all the cut combinations is not very practical, because of the large number of fits and the necessity to check that all the fit procedure successfully converge. For these reasons a code based on simple *counts* has been developed in this thesis. It can optimize a space with a maximum of 8 different observables, scanning each dimension with customised steps (10 bins for each observable), for a total of 10^8 configurations of cuts.

The optimization process of this thesis is divided in 2 main sequential steps, called Stage 1 and Stage 2, in order to cover a space with a number of dimension much larger than 8. This is possible thanks to the appropriate factorization of all the spaces in smaller sub-spaces, that can be considered independent in the optimization procedure. The two stages exploit the same figure of merit, although they use a different definition of S and B. A schematization of regions used to compute S and B are shown in Fig. 5.6.

- **Stage 1, D^0 mass optimization:** the starting sample is the one where the trigger decisions and the baseline requirements are applied (Fig. 5.4). The value of $\mathcal{R}$ is computed using the $m(D^0)$ distribution, applying a cut around the Δm peak. Moreover, only variables related to the D^0 and to the D^0 daughters are allowed as input. This first stage aims at reducing the combinatorial background in the $m(D^0)$ distribution. As it is shown in Fig. 5.6, the background regions (marked in red) are located outside the D^0 and Δm peaks (the so called sidebands). The signal region (marked in green) is composed by events falling within the D^0 and Δm peaks.

- **Stage 2, Δm optimization:** the starting sample is the one obtained after the Stage 1 optimization. This time, the figure of merit $\mathcal{R}$ is computed using the Δm distribution. The cut around the Δm signal peak is removed and a cut around the m(D^0) signal peak is applied . Only variables related to the D^* and π_s are allowed as input. The second stage aims at reducing the background of the D^0 candidates that do not come from a real D^* decay. As it is shown in Fig. 5.6, the background region (marked in red) is located in the right sideband of the Δm signal peak. The signal region (marked in green) is composed by events falling within the D^0 and Δm peak.

The optimization algorithm, at the beginning of both steps, needs to know two inputs: the number of observables to be optimized and the domain of each variable. In addition, the number of bin for the scan of each observable, is required. At this point, 2 n-dimensional histograms are filled, one with signal events (h_S^X) and another one with background events (h_B^X). The superscript X is replaced by D^0 or by Δm in the Stage 1 or Stage 2, respectively. It stands for the mass distribution in which the S and B regions are defined. The number of dimensions is determined by the number of input variables. When the h_S^X and h_B^X histograms are filled, the cumulant distribution for both of them is built to quantify the number of signal and background candidates passing the cut of interest. In this way each bin univocally corresponds to a precise combination of cuts. Finally, using the two histograms, the value of $\mathcal{R}$ is computed for each combination of cuts (bins). The optimization process is applied to a small sub-sample of the available data collected during 2016, corresponding to 2/5*{WS, RS}{L, D}{MagDown}{2016}. In the following section, the computation of the figure of merit $\mathcal{R}$ for both the stages is described in detail.

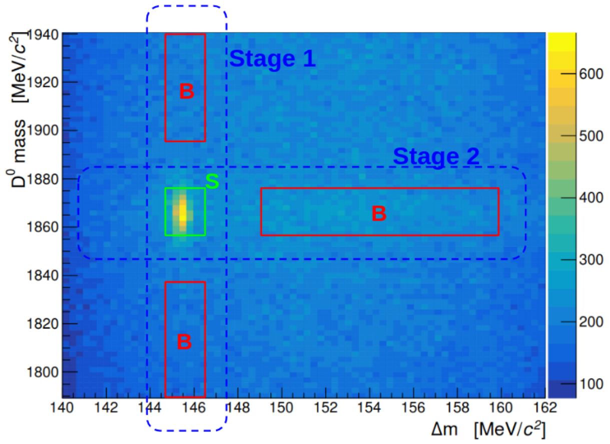

Figure 5.6: *2D distribution of $m(D^0)$ and Δm invariant masses. The red and green regions represent the background and the signal regions, respectively.*

The determination the figure of merit

Stage 1, D^0 mass optimization: At this stage, the figure of merit $\mathcal{R}$ is computed using the D^0 mass distribution, applying a cut around the Δm peak ($\Delta m \in [144.625, 146.125]$ MeV$/c^2$, a symmetrical range around the modal value of the distribution in order to retain the 95% of the signal). Three different regions are identified:

- **Bl**, background region on the left of the peak: $[\mu - 7\sigma,\, \mu - 5\sigma]_{D^0_M}$,
- **Br**, background region on the right of the peak: $[\mu + 5\sigma,\, \mu + 7\sigma]_{D^0_M}$,
- **SB**, region within the m(D^0) peak: $[\mu - \sigma,\, \mu + \sigma]_{D^0_M}$. In this region both signal and background events are present,

where $\mu_{D^0_M}$ = 1864.83 MeV$/c^2$ and $\sigma_{D^0_M}$ = 10.8 MeV$/c^2$. The three regions are illustrated in Fig. 5.7 on the left hand side. The blue shaded areas are the **Bl** and **Br** regions, whereas, the green shaded area is the **SB** region. Using these regions, it is now possible to fill the 3 histograms ($h^{D^0}_{Bl}$, $h^{D^0}_{Br}$ and $h^{D^0}_{SB}$) with the events belonging to the relative mass regions. Since the $h^{D^0}_{SB}$ histogram includes both signal and background candidates, it is necessary to subtract the background in order to obtain an histogram ($h^{D^0}_{S}$) with only signal candidates. In order to do that, it is sufficient to create two new histogram as

$$h^{D^0}_{B} := \frac{h^{D^0}_{Br} + h^{D^0}_{Bl}}{2}, \tag{5.2}$$

$$h^{D^0}_{S} := h^{D^0}_{SB} - h^{D^0}_{B}. \tag{5.3}$$

where the shape of the background is assumed to be linear. At this point, it is possible to compute the value of the figure of merit $\mathcal{R}$ for each bin[3] and find the combination of cuts that gives the highest value of $\mathcal{R}$. It is computed using Eq. 5.1 for each bin, where S will be replaced by the bins content of the $h^{D^0}_{S}$ histogram, while B will be replaced by the bins content of the $h^{D^0}_{B}$ histogram.

[3]Each bin corresponds to a combination of cuts.

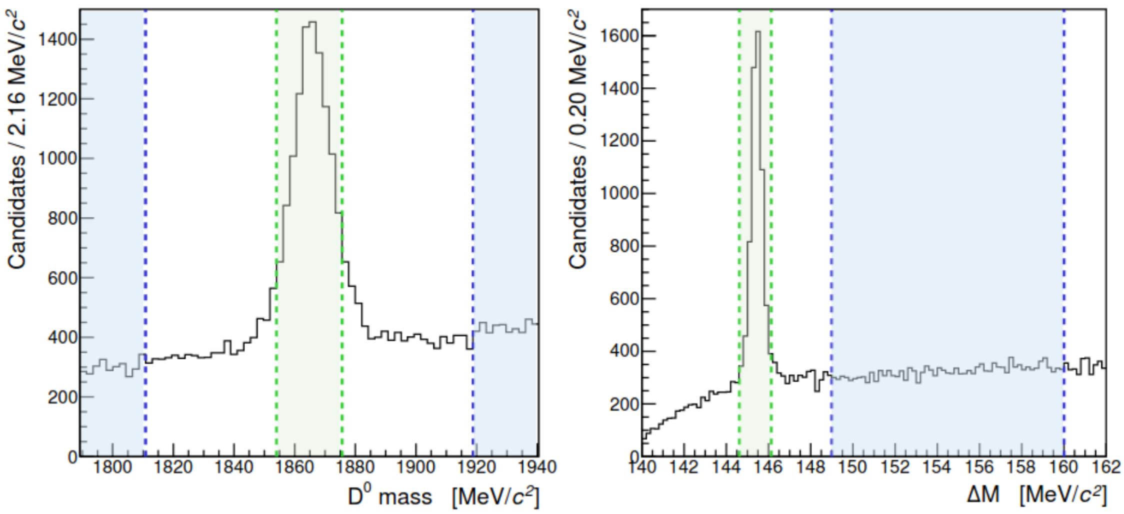

Figure 5.7: *Left: Distribution of the invariant $m(D^0)$ mass. Right: distribution of the invariant Δm mass. Trigger requirements and baseline selections are applied. The blue shaded areas stand for the backgrounds regions, while the green shaded areas stand for the signal regions used in the optimization process. It is used the 1/10 of the WS, magnet down, Long, 2016 sample.*

Stage 2, Δm optimization: The figure of merit $\mathcal{R}$ is now determined using the distribution of the Δm invariant mass, applying this time a cut around the D^0 mass peak ($m(D^0) \in [1832.43, 1897.23]$ MeV$/c^2$, about $\pm 3\sigma$ from the mean value of the D^0 invariant mass distribution, μ_{D^0}). Two regions are now defined as:

- **Br**, background region on the right of the Δm signal peak: $\Delta m \in [149, 160]$ MeV$/c^2$,
- **SB**, region under the Δm signal peak: $\Delta m \in [144.625, 146.125]$ MeV$/c^2$, symmetrical range around the modal value of the distribution in order to maintain the 95% of the signal. In this region, both signal and background are present.

The two regions are illustrated in Fig. 5.7 on the right: the blue shaded area is the **Br** region, while the green shaded area is the **SB** region. Using these two regions it is possible to fill the relative histograms ($h^{\Delta m}_{Br}$ and $h^{\Delta m}_{SB}$). Since the $h^{\Delta m}_{SB}$ histogram includes both signal and background events, it is necessary to fit the Δm distribution in order to subtract the background with the correct normalization factor. The distribution obtained after application of the selection resulted from stage 1 is fitted for this aim, and the normalization coefficient is assume to be the same for all the explored combinations of cuts. The fit function is described in detail in Sect. 5.7. The integral of the background p.d.f. in both the above-mentioned regions is computed, and the ratio between the two integrals ($\int_{SB} f_{bkg} d\Delta m / \int_{Br} f_{bkg} d\Delta m$) gives the scale factor, f_S. It allows to determine $h^{\Delta m}_S$ and $h^{\Delta m}_B$ histograms bin by bin, defined as

$$\begin{aligned} h^{\Delta m}_B &= f_S \cdot h^{\Delta m}_{Br}, \\ h^{\Delta m}_S &= h^{\Delta m}_{SB} - h^{\Delta m}_B. \end{aligned} \tag{5.4}$$

As said before, it is now possible to determine the value of the score function $\mathcal{R}$ in each bin, namely for each combination of cuts. The bin corresponding to the highest value of the figure of merit provides the optimal combination of cuts.

The next two sections explain in detail the two stages, and show the results of the optimization process.

Stage 1: $D^0 \to K_s^0 K\pi$ variables

The optimization process uses the sample selected by applying the following requirements

- trigger decisions,
- baseline selection,
- $\Delta m \in [144.625, 146.125]$ MeV/c^2.

The latter is important to suppress the background given by D^0 candidates associated to the random soft pion (combinatorial background). Only variables related to D^0 or D^0 daughters are chosen as input of the optimization algorithm, at this stage. The number of available variables is higher than 8, the maximum number of input variables that the optimization algorithm can simultaneously process. Therefore, the whole amount of variables is factorized in sub-spaces (with number of observables (dimensions) lower than 8), that can be considered independent with a good level of approximation. The optimization is performed independently on each sub-space, and a *posteriori* the accuracy of such an approximation is checked.

The optimization process in **Stage 1** is divided in the following steps:

i. Scan of the K_S and K_S daughters variables - *(6 dimensions)*.

ii. Scan of the kinematic variables of K and π from the D^0- *(7 dimensions)*.

iii. Scan of the quality tracks variables of K and π from the D^0- *(4 dimensions)*.

iv. Scan of the D^0 variables - *(5 dimensions)*.

The results of these individual steps are reported in Tab. 5.3, where the *total range* indicates the interval that includes all the domain of the variable, while the *final range* indicates the interval used by the optimization algorithm to refine the position of the optimal configuration. The algorithm is able to scan 10 bins for each observable at a time.

Stage 2: $D^{*+} \to D^0\pi^+$ variables

At this stage, the optimization process uses the sample selected by applying the following requirements:

- trigger decisions,
- baseline selection,
- requirements obtained from the Stage 1: $p_T(K_S) > 200$ MeV/c and $p_T(D^0) > 2520$ MeV/c.
- $m(D^0) \in [1832.43, 1897.23]$ MeV/c^2.

The Stage 2 is divided in two sub-steps:

i. scan of D^* and π_S variables - *(8 dimensions)*,

ii. re-optimization of "sensible" variables, *i.e.* only the output variables of the optimization algorithm among the two stages, are used as the new inputs and simultaneously re-optimized to account for possible correlations.

Table 5.3: *Result of the Stage 1 optimization process. *Trigger Cut. **Baseline cut.*

Candidate	Variable	Range (n.bin 10) *Total*	*Final*	Result	Units
K_S^0	p	$[3, 180]$	$[5, 100]$	-	GeV/c
	p_T	$[0, 8000]$	$[0, 500]$	> 200	MeV/c
	Vertex fit χ^2/ndf	$[0, 30^*]$	$[0, 30^*]$	-	-
$\pi^\pm$ of K_S^0	Track χ^2/ndf	$[0, 3^*]$	$[0, 3^*]$	-	-
	$\cos\theta_{\pi\pi}$	$[0.97, 1]$	$[0.97, 1]$	-	-
$K^\pm\pi^\mp$ of D^0	p	$[5^*, 140]$	$[5^*, 100]$ $\pi^\mp$	-	GeV/c
		$[5^*, 140]$	$[5^*, 100]$ $K^\pm$	-	GeV/c
	p_T	$[800^*, 9000]$	$[800^*, 4000]$ $\pi^\mp$	-	MeV/c
		$[800^*, 9000]$	$[800^*, 4000]$ $K^\pm$	-	MeV/c
	χ^2_{IP}	$[4^*, 10000]$	$[4^*, 500]$ $\pi^\mp$	-	-
		$[4^*, 10000]$	$[4^*, 500]$ $K^\pm$	-	-
	PID_K	$[-100, 5^*]$	$[-15, 5^*]$ $\pi^\mp$	-	-
		$[5^*, 100]$	$[5^*, 20]$ $K^\pm$	-	-
	$\cos\theta_{K\pi}$	$[0.98, 1]$	$[0.99, 1]$	-	-
	Track χ^2/ndf	$[0, 3^*]$	$[0, 3^*]$ $\pi^\mp$	-	-
		$[0, 3^*]$	$[0, 3^*]$ $K^\pm$	-	-
	$\mathcal{P}_{GHOST}$	$[0, 0.4^*]$	$[0, 0.4^*]$ $\pi^\mp$	-	-
		$[0, 0.4^*]$	$[0, 0.4^*]$ $K^\pm$	-	-
D^0	p	$[15, 350]$	$[20, 200]$	-	GeV/c
	p_T	$[1.8^*, 16]$	$[1.8^*, 3]$	> 2.52	GeV/c
	Vertex fit χ^2/ndf	$[0, 20^*]$	$[0, 20^*]$	-	-
	χ^2_{FD}	$[0, 400]$	$[0, 100]$	-	-
	FD	$[0, 1000]$	$[0, 200]$	-	mm
	χ^2_{IP}	-	$[0, 9^{**}]$	-	-

Before running the latter step, the requirements resulting from the first stage are removed in order to check the accuracy of factorization between the different sub-spaces and between stage 1 and 2 . If the factorization is accurate, a similar output is expected. The resulting requirements of the first step are listed in Tab.5.4, while the results of the second step are shown in Tab. 5.5.

Table 5.4: *Result of the Stage 2 (step i) optimization. *Trigger requirement.*

Candidate	Variable	Range *Total*	Range *Final*	Requirements	Units
D^*	$DTF\chi^2$	$[0, 5000]$	$[10, 50]$	-	-
	DTF Vertex fit χ^2/ndf	$[0, 500]$	$[0, 10]$	-	-
π_S	Track χ^2/ndf	$[0, 3^*]$	$[0, 3^*]$	-	-
	PID_e	$[-15, 15]$	$[-5, 10]$	< 5.5	-
	χ^2_{IP}	$[0, 120]$	$[0, 100]$	< 40	-
	PID_K	$[-40, 30]$	$[-30, 20]$	-	-
	$\mathcal{P}_{Ghost}$	$[0, 0.25^*]$	$[0, 0.25^*]$	-	-
	p_T	$[100, 1100]$	$[200, 1000]$	-	MeV$/c$

Table 5.5: *Result of the Stage 2 (step ii) optimization.*

Candidate	Variable	Range (n.bin 10) *Final*	Requirements	Units
K_S	p_T	$[100, 600]$	> 350	MeV$/c$
D^0	p_T	$[2, 3]$	> 2.5	GeV$/c$
π_S	PID_e	$[-5, 6]$	< 4.9	-
	χ^2_{IP}	$[0, 100]$	< 40	-

The final result of the optimization process (Stage 1 plus Stage 2) returns a value for the figure of merit of $\mathcal{R} = 60.96$, applying the full selection with optimized cuts shown in Tab. 5.5. This values has to be compared with the value determined after the application of the baseline selection of $\mathcal{R} = 60.59$ (see Fig. 5.5). It can be noted that the optimization process does not bring any significant improvement of the score function value, and this is mainly due to the fact that the baseline selection, along with the trigger requirements, are already a set of very stringent requirements. Any further tighter requirement would allow to reduce the background but with a non negligible loss of signal decays. However, this accounts only for the statistical component of the final uncertainty, neglecting any possible contribution from systematic uncertainty. In any case, the purity of the final sample is increased by a factor of about $60.96/27.43 = 2.2$ by comparing the initial data sample collected using only the trigger decisions (Sect. 5.2) and that one obtained with the application of the baseline and optimized requirements.

It is also worth noting that the results reported in Tab. 5.5 are very similar to the results obtained performing separately Stage 1 and Stage 2, where observables relative to the D^0 candidates and to its decays products are optimized independently from the those relative to the D^* candidates, Tab. 5.4. The values of $\mathcal{R}$, computed in the two configurations are indeed very similar, $\mathcal{R} = 60.83$ from step *i*, and $\mathcal{R} = 60.96$ from step *ii*. The configuration resulting from step *ii* is chosen as final selection. Figure 5.8 shows the final distributions of both the D^0 and Δm invariant masses, after the application of optimized requirements.

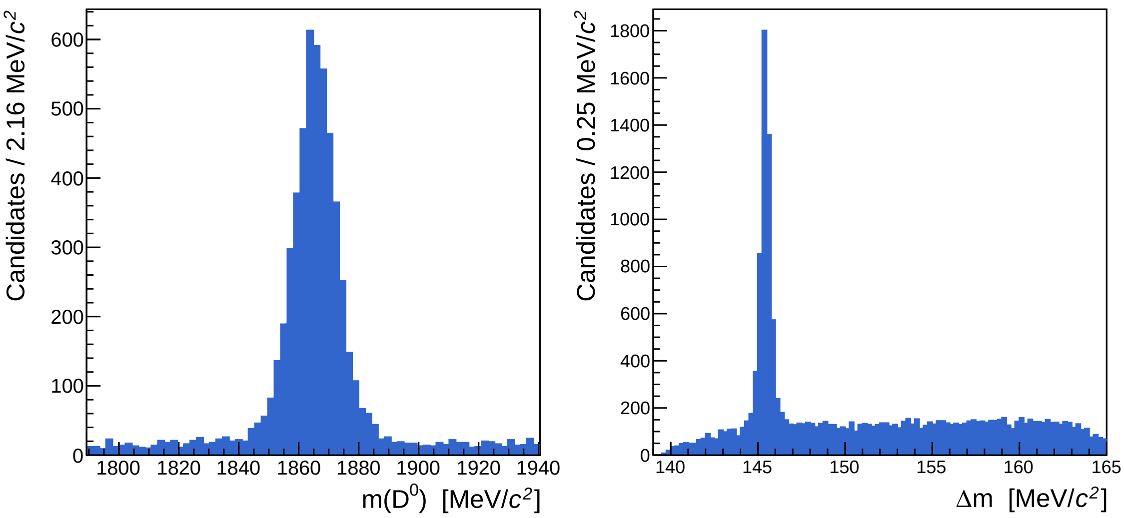

Figure 5.8: *Distribution of the invariant Δm mass after the application of the final selection. Sample:* 1/10*{*WS*}{*L, D*}{*MagDown*}{*2016*}.

The untagged $D^0 \to K^0_s K^\pm \pi^\mp$ decays

During the work of this thesis, using the optimization algorithm developed in the previous sections, the possibility to perform the analysis using the *untagged* sample of $D^0 \to K^0_S K^\pm \pi^\mp$ decays is also explored. As explained in Sect. 2.1, this would allow to largely increase the statistics, using D^0 candidates with no information of flavour at production, namely without the reconstruction of the $D^{*+} \to D^0 \pi^+$ strong decay chain. Unfortunately, there is no trigger line dedicated to this sample in LHCb and only *tagged* decays have been saved on permanent storage, so far. It would be very interesting to optimize the selection of such decays in order to reduce the size of the sample to be saved, with the aim of drastically increasing the purity already at trigger level. This would certainly allow the implementation of a dedicated trigger line during the LHCb-Upgrade in Run 3 and Run 4.

As mentioned before, these decays are not available in LHCb, however, it is possible to select a sample of pure *untagged* decays by looking at real D^0 decays populating the Δm sideband $[149, 160]$ MeV/c^2. The study performed using these decays is an important result of the work described in this thesis. However, to avoid a very long digression here, the selection optimization and final results for these decays are reported in Appendix A. In this case, without the great discrimination power of the Δm observable, the final selection, given by the optimization algorithm, largely increase the purity of the final sample, paving the way for the implementation of a future trigger line in the Upgrade era, specifically dedicated to the untagged sample.

5.5 Further offline requirements

The optimization algorithm searches for the cut combination that gives the highest value of $\mathcal{R}$, accounting only for the statistical component of the final A_{CP} uncertainty. However, possible contributions from systematic effects could play a role. For instance, one may afford a little degradation of the statistical power in order to significantly reduce the background level, and therefore possible contributions from systematics. For this reason some variables with high separation power, between signal and background, are further studied: such as the vertex fit $\chi^2/ndf(D^0)$ and DTF Vertex fit $\chi^2/ndf(D^*)$. The optimization algorithm does not tight the thresholds of these variables, but from studies performed in a similar analysis, involving the $D^0 \to K_S\pi\pi$ decays [47], they are known the have a good separation power. Their distributions for the signal and the background are displayed and compared in Fig. 5.9.

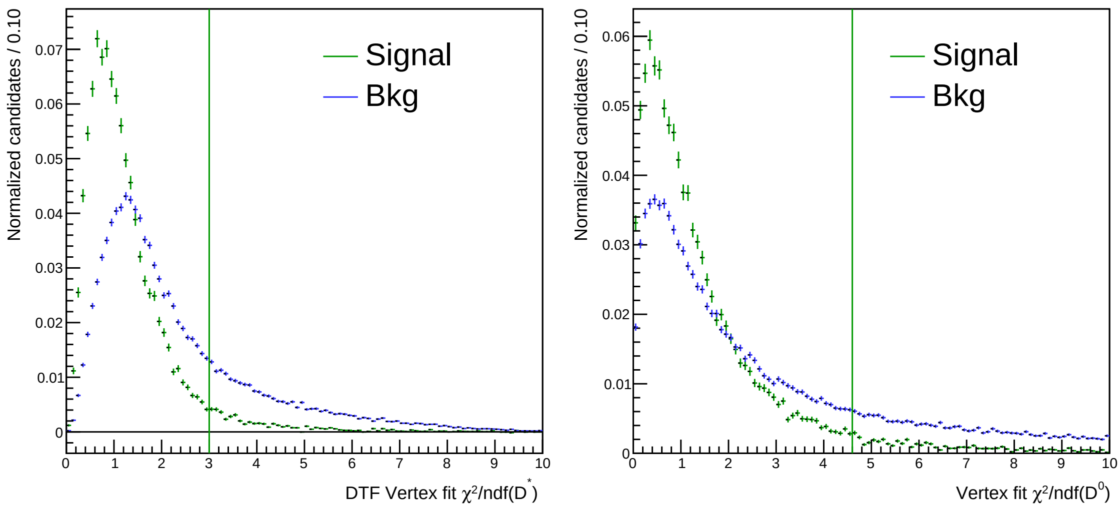

Figure 5.9: *Distribution of the signal (green points) and background (blue points) of the DTF Vertex fit $\chi^2/ndf(D^*)$ on the left, and of Vertex fit $\chi^2/ndf(D^0)$ on the right. The green vertical lines show the thresholds of the applied cuts, corresponding to the 95% fraction of the signal.*

The green vertical lines indicate the cuts, chosen keeping the 95% of the signal: DTF Vertex fit $\chi^2/ndf(D^*) < 3$ and Vertex fit $\chi^2/ndf(D^0) < 4.6$. The quantity $\mathcal{R}$ decreases from $\mathcal{R} = 60.96$ to $\mathcal{R} = 59.57$. This change does not affect significantly the uncertainty on the A_{CP} measurement. The effects on the two cuts are shown in Fig. 5.10 where the $m(D^0)$ and Δm distributions are shown on the left and right hand side, respectively. The light blue histograms are obtained applying the cuts resulting from the optimization algorithm. The dark blue shaded histograms have the two new extra cuts. Finally, the whole optimization process is run one more time keeping these two additional requirements among the baseline selection. A similar and consistent result is obtained. For this reason, we have decided to maintain the same thresholds previously determined. A list of the final offline selection is reported in Tab. 5.6. While, the summary of the Hlt2 requirements, baseline and offline selections, is reported in Tab. 5.8, at the end of the chapter.

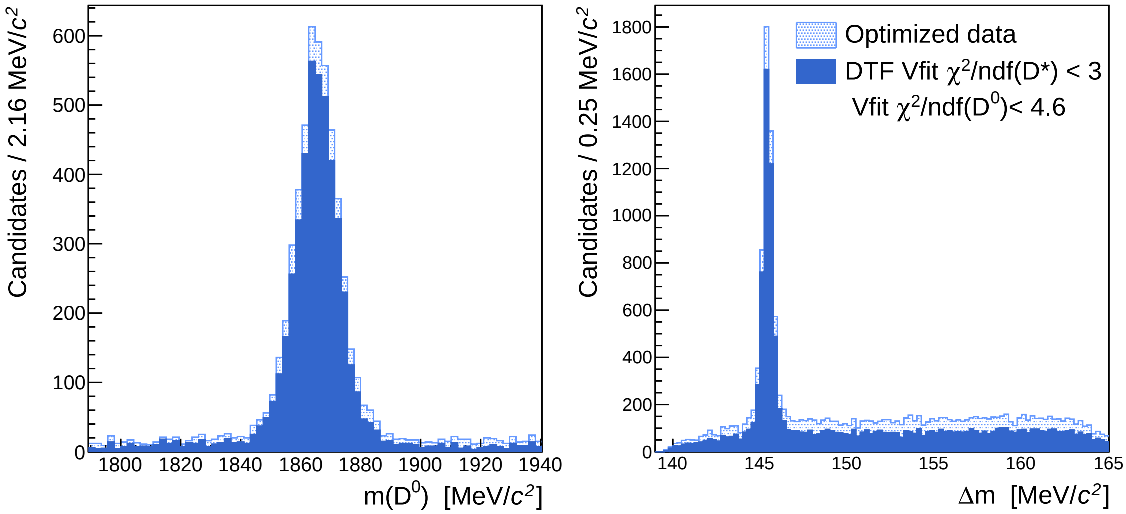

Figure 5.10: *The D^0 mass and Δm plots respectively on the left and on the right of the picture. Comparison between the starting sample (black line) and the sample given by the optimization selection with the extra cuts written in the legend (blue colored). Sample:* $2/5^*\{WS, RS\}\{L, D\}\{MagDown\}\{2016\}$.

Table 5.6: *Offline selection.*

Candidate	Variable	Requirements	Units
K_S	p_T	> 350	MeV/c
D^0	p_T Vertex fit χ^2/ndf	> 2500 < 4.6	MeV/c -
D^*	DTF Vertex fit χ^2/ndf	< 3	-
π_S	PID_e χ^2_{IP}	< 4.9 < 40	-

5.6 Multiple candidates rejection

A D^0 candidate is considered as a multiple candidate when it is associated with more than one soft pion. They are fake candidates that is better to remove from the sample. Before applying any requirements, the percentage of multiple candidates was $\sim$ 22%. After the selection, this fraction drops to $\sim$ 7%. In order to avoid a bias due to the presence of multiple candidates, just one D^0 candidate, randomly chosen, is kept. The distribution of the multiple candidates, normalized to the total number of events, is shown in Fig. 5.11 as an example, for the {RS}{L}{MagDown}{2016} sub-sample. Since

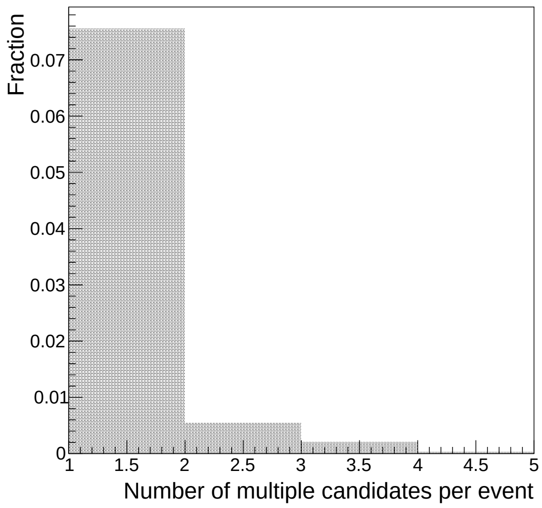

Figure 5.11: *Fraction of events in function of the number of multiple candidates per event.*

the whole sample is divided in two sub-sample, WS and RS decays, as described in Sect. 4.1, it may happens that a $D^0 \to K^0_S K^- \pi^+$ is associated to a $\pi_s{}^-$ and classified as a WS decay, $\overline{D}^0 \to K^0_S K^- \pi^+$, and vice versa. Therefore, it is necessary to check the fraction of multiple candidates in common to the RS and WS sub-samples. This is done after the application of the final selection and it is found that $\sim$ 4% of the total (RS + WS) events are multiple candidates, but just the 0.2% is located in the Δm peak. Since this fraction is very small, possible systematic effects on the final measurements are neglected for the moment. The rejection of the multiple candidates is done for all the 24 sub-set used in the present analysis.

5.7 Determination of the yields

It is now possible to find the signal yields, *i.e.* the total number of reconstructed signal candidates all over the data taking periods. The following section describes the signal and background p.d.f. used to perform the fit to the invariant Δm mass.

Signal model

The signal probability density function (pdf) reads

$$\begin{aligned}\mathcal{P}_{sgn}(\Delta m|\boldsymbol{\theta_{sgn}}) =& f_J \cdot \mathcal{J}(\Delta m|m_{D^*} + \mu_J, \sigma_J, \delta_J, \gamma_J) + \\ & (1 - f_J) f_{G1} \cdot \mathcal{G}(\Delta m|m_{D^*} + \mu_{G1}, \sigma_{G1}) + \\ & (1 - f_J)(1 - f_{G1}) f_{G2} \cdot \mathcal{G}(\Delta m|m_{D^*} \mu_{G2}, \sigma_{G2}) + \\ & (1 - f_J)(1 - f_{G1})(1 - f_{G2}) \cdot \mathcal{G}(\Delta m|m_{D^*} + \mu_{G3}, \sigma_{G3})\end{aligned}$$

Where the $\mathcal{J}$ stands for the Johnson function[48]:

$$\mathcal{J}(x|\mu, \sigma, \delta, \gamma) = \frac{\exp\{-\frac{1}{2}[\gamma + \delta \sinh^{-1}(\frac{x-\mu}{\sigma})]^2\}}{\sqrt{1 + (\frac{x-\mu}{\sigma})^2}} \tag{5.5}$$

and $\mathcal{G}$ stands for the Gauss funcion:

$$\mathcal{G}(x|\mu, \sigma) = \frac{1}{\sigma\sqrt{2\pi}} \exp\left\{-\frac{(x-\mu)^2}{2\sigma^2}\right\} \tag{5.6}$$

The parameter $\boldsymbol{\theta_{sgn}}$ includes the relative fraction between the Johnson and Gauss functions (f_J), the relative fraction of each Gauss function (f_{Gi}, $i = 1, 2, 3$), the shift from the D^* mass of the Johnson and Gauss functions (μ_J, μ_{Gi}), the width of the distributions (σ_J, σ_{Gi}) and finally the parameters linked to the asymmetric tails of the Johnson function (δ_J, γ_J).

Combinatorial background model

The combinatorial background is due to a random associations of a pion with a genuine D^0 decay and it is modeled using a simplified two-body phase-space model:

$$\mathcal{P}_{bkg}(\Delta m|\boldsymbol{\theta_{bkg}}) = \frac{1}{\mathcal{N}_B(\boldsymbol{\theta_{bkg}})}[(m - m_0)^{1/2} + \alpha(m - m_0)^{3/2} + \beta(m - m_0)^{5/2}] \tag{5.7}$$

where $m_0 = m_\pi \approx 139.6$ MeV$/c^2$ is the threshold value and $\mathcal{N}_B$ is the normalization factor. The parameter $\boldsymbol{\theta_{bkg}}$ include the shape parameters α and β.

Fit method

The total probability density function is the following:

$$\mathcal{P}(\Delta m) = N_{sgn}\mathcal{P}_{sgn}(\Delta m|\boldsymbol{\theta_{sgn}}) + N_{bkg}\mathcal{P}_{bkg}(\Delta m|\boldsymbol{\theta_{bkg}}) \tag{5.8}$$

where each function is defined for masses greater than the threshold value and is properly normalized in the fit range, which extends from 140 MeV$/c^2$ to 162 MeV$/c^2$. The total yields for the RS and WS samples are reported in Tab. 5.7, where they are compared with the ones of the Run 1 analysis [8]. One can see that the amount of data relative to the Run 2 is larger, in particular the signal yields/fb^{-1} is increased by about a factor of 4.9. The Fig. 5.12 shows the Δm distribution, where the total fit function is applied. The same fit procedure is applied to the all samples. The signal yields are listed in App. B, in Tab. B.1 for the WS sample and Tab. B.2 for the RS sample, with the respective fitted distributions. The total yield is increased by a factor of 9 with respect to that one of Run 1 analysis, much higher than the factor expected from the only increase of the integrated

Table 5.7: *Comparison of the Run 2 and Run 1 yields. In 2011, only LL K_S candidates were available.*

	Run1 ($3fb^{-1}$)	Run2 ($5.6fb^{-1}$)
RS	113k	1044k
WS	76k	718k

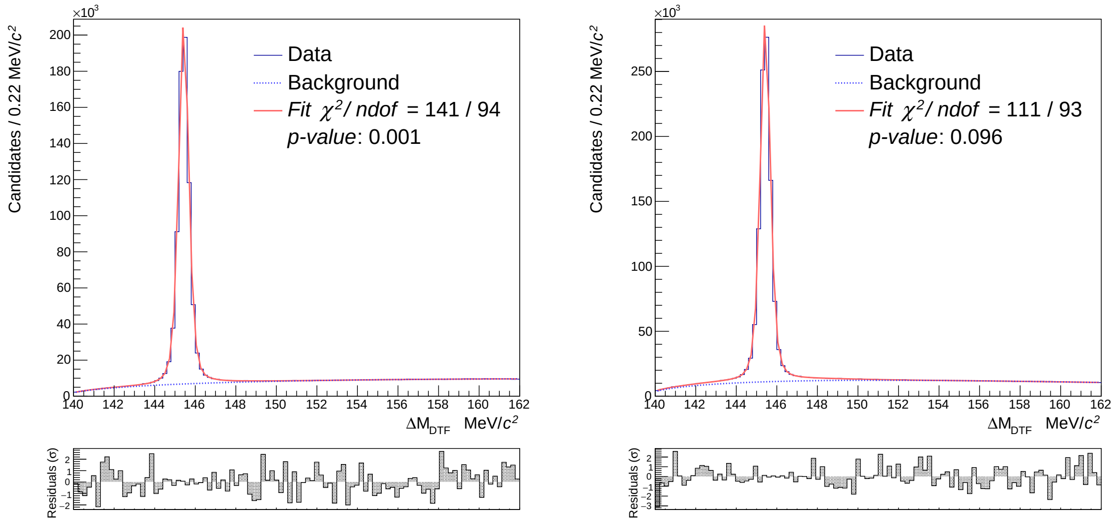

Figure 5.12: *Δm distribution after the application of all requirements reported in Tab. 5.8. The total WS sample is plotted on the left, while the total RS sample is plotted on the right. Normalized pulls are displayed in the inset.*

luminosity. This is mainly due to the optimized trigger system and to the increase of charm production cross section at the new center-of-mass energy $\sqrt{s} = 13$ TeV. Therefore, now it is possible to explore the region with a level of accuracy of per mil for such decay modes.

The next chapter presents the measurement of the $\Delta A_{CP}^{RS(WS)}$ observable, where the $D^0 \to K_S^0\pi\pi$ control mode is used. The offline selection, optimized for the signal sample, is also applied to the $D^0 \to K_S^0\pi\pi$ calibration decay mode. The number of reconstructed candidates of this mode, about 12 M, is much higher than that one of the signal mode, even though a sub-optimal cuts configuration is applied. Hence, the statistical uncertainty on the A_{CP} measurement will be fully dominated by the uncertainty on the yield of the signal modes.

Table 5.8: *Summary of the Hlt2 and Offline selections. $h^{\pm}$ stands for the charged particles from the D^0 decay, the K and π. The superscripts L or D specify the type of track to which the requirement is applied. The superscripts '16, '17 and '18 stand for the year in which a certain threshold is chosen. If it is not specified any kind of superscript, the requirement is on both the types of tracks and the threshold is the same all over the data taking periods.*

Candidate	Variable	Requirements Hlt2	Offline	Units
$\pi^{\pm}$ of K_S^0	Track χ^2/ndf	$< 3^L$	-	
		$< 4^D$	-	-
	IP χ^2	$< 3^L$	-	-
	p	$> 3^D$	-	GeV/c
	p_T	$> 175^D$	-	MeV/c
	η	-	$[2, 4.2]$	-
K_S^0	$\lvert m(\pi^+\pi^-) - m_{K_S^0}^{PDG} \rvert$	$< 35^L$	-	MeV/c^2
		$< 64^D$	-	MeV/c^2
	Vertex-fit χ^2/ndf	< 30	-	-
	Decay time wrt primary vertex	$> 2^L$	-	ps
		$> 0.5^D$	-	ps
	z position of the vertex	[-0.1,0.5]^L	-	m
		[0.4, 2.275]^D	-	m
	mass	-	[485,510]	MeV/c^2
	$\log(\chi^2_{FD})$ wrt origin vertex	-	> 5	-
	p_T	-	> 350	MeV/c
$h^{\pm}$ of D^0	Track χ^2/ndf	< 3	-	
	$\mathcal{P}_{ghost}$	< 0.4	-	-
	p	> 1	> 5	GeV/c
	p_T	> 200	> 800	MeV/c
	IP χ^2	> 4	-	-
	$DLL_{K\pi}$	< 5 $\pi^{\pm}$	-	-
		> 5 $K^{\pm}$	-	-
	$DLL_{K\pi}$	-	< -5 $\pi^{\pm}$	-
	η	-	$[2, 4.2]$	-
D^0	Mass	$[1.765, 1.965]$	-	GeV/c^2
	Vertex-fit χ^2 /ndf	< 20	< 4.6	-
	p_T	> 1.8	> 2.5	GeV/c^2
	Direction angle	< 34.6	-	mrad
	Lifetime wrt best PV	$> 0.25\tau$	$[0.3, 8]\tau$	-
	Flight-distance χ^2	> 20	-	-
	χ^2_{IP}	-	< 9	-
π_s	Track χ^2/ndf	< 3	-	-
	$\mathcal{P}_{ghost}$	$< 0.4^{'16}$	< 0.25	-
		$< 0.25^{'17,'18}$		
	p	> 1	-	GeV/c
	p_T	$> 100^{'16}$	> 200	MeV/c
		$> 200^{'17,'18}$		
	PID_e	-	< 4.9	-
	χ^2_{IP}	-	< 40	-
D^*	Vertex-fit χ^2/ndf	< 10	-	-
	Δ m	$[135, 165]$	-	MeV/c^2
	DTF Vertex fit χ^2/ndf	-	< 3	-

6 Measurement of ΔA_{raw} observable

This chapter describes the measurement of the $\Delta A_{CP}^{RS(WS)}$ observable, namely the difference between the time-dependent "raw" asymmetries of the $D^0 \to K_S^0 K^\pm \pi^\mp$ signal mode and the $D^0 \to K_S^0 \pi^+\pi^-$ calibration mode. This is necessary to remove the nuisance detection and production asymmetries. A particular attention is given to the removal of the detection asymmetries due to the reconstruction of the neutral kaon.

6.1 Introduction

This chapter describes the cancellation mechanism used to cancel out the most relevant nuisance asymmetries by means the difference of the raw asymmetries between signal and control modes. The idea is to exploit the well-known ΔA_{CP} mechanism [3] to remove the detection asymmetries of the neutral kaon, the detection $A_D(\pi_s)$ and the production $A_P(D^*)$ terms. A brief recap of the strategy is given, in order to simplify the reading. The raw *CP* asymmetries of the signal[1] and control modes read:

$$\begin{aligned} A_{raw}^{RS}(D^{*+} \to [K_S^0 K^-\pi^+]\pi_s{}^+) \approx\ & A_P(D^{*+}) + A_{CP}^{RS}(D^0 \to K_S^0 K^-\pi^+) + \\ & + A_D(K\pi) + A_D^{K\pi}(K^0) + A_D(\pi_s{}^+), \end{aligned} \tag{6.1}$$

$$\begin{aligned} A_{raw}^{\pi\pi}(D^{*+} \to [K_S^0 \pi^+\pi^-]\pi_s{}^+) \approx\ & A_{CP}(D^0 \to K_S^0 \pi^+\pi^-) + A_P(D^{*+}) + \\ & + A_D(\pi_s{}^+) + A_D(\pi^+\pi^-) + A_D^{\pi\pi}(K^0), \end{aligned} \tag{6.2}$$

where each term is described in detail in Sect. 2.3. What survives the difference is the following :

$$\begin{aligned} \Delta A_{raw}^{RS} =& A_{raw}^{RS}(D^{*+} \to [K_S^0 K^-\pi^+]\pi_s{}^+) - A_{raw}^{\pi\pi}(D^{*+} \to [K_S^0 \pi^-\pi^+]\pi_s{}^+) \approx \\ & A_{CP}^{RS}(D^0 \to K_S^0 K\pi) + A_D(K\pi) - A_D(\pi\pi) + A_D^{K\pi}(K^0) - A_D^{\pi\pi}(K^0), \end{aligned} \tag{6.3}$$

neglecting the physics quantity $A_{CP}(D^0 \to K_S^0\pi^+\pi^-)$, because it is much smaller than the achievable uncertainty (see Sect. 2.3). The $A_D(\pi_s)$ and $A_P(D^*)$ terms cancel out in the difference, as long as the kinematics of the decay $D^* \to D^0\pi_s$ is the same between signal and control samples. In order to do that a re-weighting procedure is applied, in particular the distributions of the $p(D^0)$, $p_T(D^0)$ and $p_T(\pi_s)$ variables of the control decay mode are

[1] The equations for the RS data sample are only displayed, while those for the WS samples are reported in Eq. 2.40.

re-weighted to be equal to those of the signal decay mode. The re-weighting procedure will be described in Sect. 6.4. For what concerns the detection asymmetries of the neutral kaons ($A_D^{K\pi}(K^0)$ and $A_D^{\pi\pi}(K^0)$), it is not possible to assume a priori that the two terms are equal. They can be cancelled out by exploiting a time-dependent procedure, in fact the K^0 detection asymmetry varies as function of the K_S^0 proper decay time. In particular $A_D^{K\pi}(K^0)$ and $A_D^{\pi\pi}(K^0)$ have a very nearly-linear trend[2] and they are null for $t = 0$. Therefore, we can exploit the fact that the difference between two approximately linear similar functions can be further expanded, at first order, as a linear function, with an excellent level of precision. The time dependent $A_{raw}^{RS(WS)}(t)$ and $A_{raw}^{\pi\pi}(t)$ are computed in order to perform the $\Delta A_{raw}^{RS(WS)}(t)$ difference between the signal and the control modes as a function of the decay time. Hence, this observable is fitted to a linear function, where the $\Delta A_{raw}^{RS(WS)}(t = 0)$ is the parameter of interest. In this way the contribution due to the detection asymmetry $A_D(\pi_s)$ and due to the production asymmetry $A_P(D^*)$ cancel out in each bin of decay time, while the contribution due to the neutral kaon asymmetry $A_D(K^0)$ disappears at $t = 0$.

6.2 K_S^0 proper decay-time bins

The K_S^0 mesons are reconstructed in the symmetric final state $\pi^+\pi^-$ ($\mathcal{B}(K_S^0 \to \pi^+\pi^-) \sim 70\%$) and, as explained in Sect. 2.3, it is one of the two mass eigenstates of the neutral kaon system, K^0 and $\overline{K}^0$. Despite its name the K_S^0 mesons have a rather long lifetime compared to the LHCb scale, indeed only a third of the reconstructed decays occurs inside the VELO. These K_S^0 are reconstructed with two Long tracks. Those which decay between VELO and TT are reconstructed with two Downstream tracks. In Fig. 6.1, the distribution of the reconstructed decay time for Long and Downstream K_S^0 is reported. It is possible

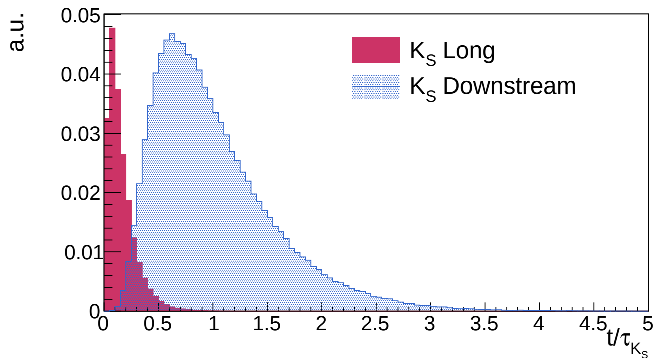

Figure 6.1: *Distributions of the proper decay time of the Long K_S^0 (purple) and Downstream K_S^0 (light blue). The decay time is given in terms of the K_S^0 lifetime $\tau_{K_S^0}$. {2016} sample.*

to notice that the Long K_S^0 distribution ends before to reach one K_S^0 mean lifetime ($\tau_{K_S^0}$), instead the Downstream K_S^0 distribution has a tail up to $\sim 3.5\tau_{K_S^0}$. Since interference between different processes (absorption in matter and *CP* violation) are not negligible for long K_S^0 decay time values, as shown in Fig. 2.9, the behaviour of the detection asymmetry $A_D(K^0)$ becomes largely not linear. Hence, the region between $[0, 2.5]\tau_{K_S^0}$ will

[2]This is clearly (see Fig. 2.9) a very good approximation for small values of the decay time ($t/\tau(K_S^0) \ll 1$). However data shows this is a very good approximation up to values of $t/\tau(K_S^0) \approx 2.5$

be used for the $\Delta A^{RS(WS)}_{raw}(t)$ time-dependent measurement. The behaviour of $A_D(K^0)$ can be approximated as linear in this range of K^0_S decay time, with great accuracy, and interference effects can be kept under control. It is worth noting that this assumption, for the individual raw time-dependent asymmetries, is not crucial for the determination of $\Delta A^{RS(WS)}_{raw}(t=0)$ parameter: the difference between two very similar functions can be further expanded, at first order in the parameters difference, as a linear function. This is particularly true in our case because we expect that $A^{\pi\pi}_D(K^0) \approx A^{RS}_D(K^0) \approx -A^{WS}_D(K^0)$, because contributions from doubly-Cabibbo-suppressed decays are small. In addition, linearity of individual raw asymmetries can be experimentally verified using data itself at very high precision, for instance using the abundant sample of $D^0 \to K^0_S\pi^+\pi^-$ decays.

The decay time distribution for Long K^0_S is totally contained into the selected range, and just the 2% of the Downstream data is discarded. The Long and Downstream samples are studied separately in this thesis, they are divided in 6 bins between $[0,1]\tau_{K^0_S}$ and 12 bins between $[0,2.5]\tau_{K^0_S}$, respectively. The bin size is selected in order to contain about the same amount of data. Table 6.1 shows the ranges of each K^0_S proper decay-time bin, for both the Long (L) and Downstream (D) samples.

bin	L $t/\tau_{K^0_S}$	bin	D $t/\tau_{K^0_S}$	bin	D $t/\tau_{K^0_S}$
0	[0, 0.05]	6	[0, 0.39]	12	[0.87, 0.98]
1	[0.05, 0.08]	7	[0.39, 0.50]	13	[0.98, 1.10]
2	[0.08, 0.12]	8	[0.50, 0.59]	14	[1.10, 1.26]
3	[0.12, 0.17]	9	[0.59, 0.68]	15	[1.26, 1.48]
4	[0.17, 0.25]	10	[0.68, 0.77]	16	[1.48, 1.80]
5	[0.25, 1.00]	11	[0.77, 0.87]	17	[1.80, 2.50]

Table 6.1: *Definition of the decay-time bins, in units of K^0_S lifetime $\tau_{K^0_S}$, for the Long (L) and Downstream (D) K^0_S samples.*

6.3 Removal of the combinatorial background

In order to measure the raw asymmetries of the decay channels of interest, the number of D^0 and $\overline{D}^0$ reconstructed candidates are counted. This is done through a count of the number of weighted entries of the histograms, in the Δm region [144.625, 146, 125] MeV/c^2. In this way, the determination of the raw asymmetries is independent as much as possible from the empirical choice of the signal and background p.d.f.s. In order to count only signal candidates, the combinatorial background in the invariant Δm mass is removed, by means a classic procedure of sideband subtraction. Hence, a fit to each sample is performed, in order to compute the scale factor (f_S), defined as the ratio of the background area under the Δm signal region to the background area in the Δm sideband (see for instance Fig. 6.2). The opposite of the scale factor is used to weight ($w^s = -f_s$) the candidates belonging to the sideband region ([149, 160] MeV/c^2), while no weight is applied to the candidates in the Δm signal region ([144.625, 146.125] MeV/c^2). Different scale factors are determined for the Δm distribution of the RS, WS and $D^0 \to K^0_S\pi\pi$ samples, for different years of data taking, and for L and D K^0_S ({RS, WS, $D^0 \to K^0_S\pi\pi$}{L, D}{2016, 2017, 2018}), for a total of 18 fits.

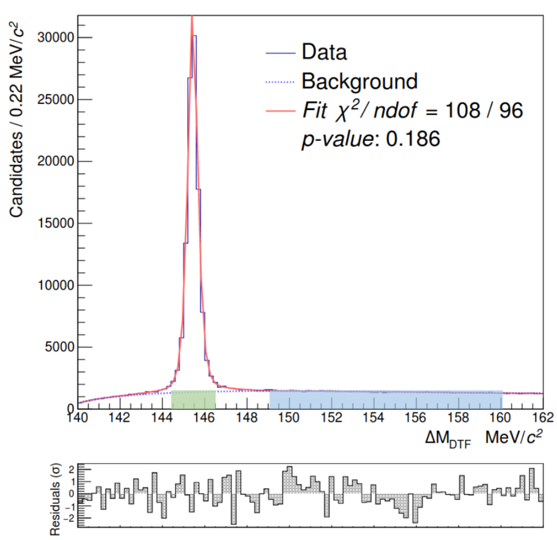

Figure 6.2: *Invariant Δm distribution, where the total pdf is shown as a red line. The shaded regions are used to extract the scale factor (f_S), in order to subtract the background. Normalized residuals are displayed in the inset.*

6.4 Re-weighting procedure

After the removal of the background component, it is important to equalize the kinematics of the $D^{*+} \to D^0 \pi_s{}^+$ decay between the signal and calibration mode, in order to perform a reliable cancellation of the $A_P(D^*)$ and $A_D(\pi_s)$ terms, as explained in Sect. 6.1. It is worth noting that we expect very similar kinematics between the two modes, therefore, the impact of the re-weighting is by construction small, as in the famous ΔA_{CP} measurement in the two-body decays [3], hence it does not lead to a significant loss of the calibration mode data sample. We have studied the kinematic variables of the D^0 meson and of the π_s, in particular the time-integrated p, p_T and ϕ distributions of the D^0 and π_s are shown in Fig. 6.3, before any re-weighting procedure. The kinematics of the $D^0 \to K^0_S \pi\pi$ calibration mode is equalized to that one of the $D^0 \to K^0_S K\pi$ signal mode, in order to remove any possible difference. A binned re-weighting procedure is performed in the three-dimensional ($p(D^0)$,$p_T(D^0)$,$p_T(\pi_s)$) space, using 15 bins with $p(D^0)$ between 20 GeV/c and 180 GeV/c, 15 bins with $p_T(D^0)$ between 3 GeV/c and 13 GeV/c and 30 bins with $p_T(\pi_s)$ between 200 MeV/c and 900 MeV/c. The weights w^r are determined from the ratio of two three-dimensional histograms

$$w^r(p(D^0), p_T(D^0), p_T(\pi_s)) = \frac{n_{K^0_S K\pi}(p(D^0), p_T(D^0), p_T(\pi_s))}{n_{K^0_S \pi\pi}(p(D^0), p_T(D^0), p_T(\pi_s))}, \tag{6.4}$$

where $n_{K^0_S K\pi}$ and $n_{K^0_S \pi\pi}$ are the binned distributions of the number of reconstructed candidates for the signal and the calibration mode, respectively.

Figure 6.4 shows the distributions after the re-weighting procedure. Since the difference between the raw asymmetries A_{raw} is performed in each bin of K^0_S proper decay time, it is important to check that the re-weighting rule, determined by averaging over the K^0_S proper decay time, properly works in each decay time bin. In App. C.1 the same distributions of Fig. 6.4 are displayed for the L K^0_S sample for each decay-time bin, showing an excellent agreement. Same results are obtained for the D K^0_S sample.

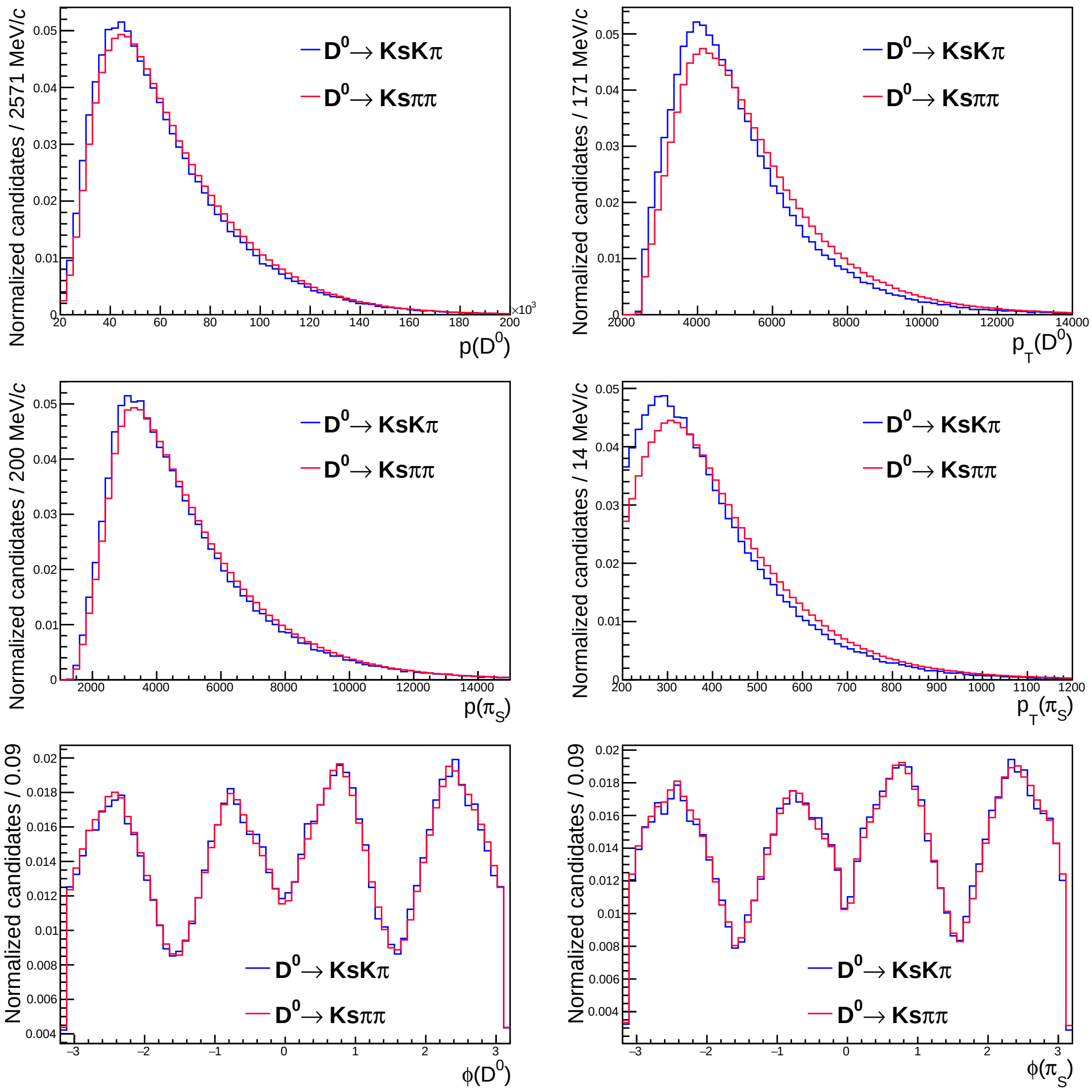

Figure 6.3: *Comparison of the time-integrated normalized variables between the $D^0 \to K^0_S K\pi$ WS signal mode and $D^0 \to K^0_S \pi\pi$ calibration mode, before the re-weighting procedure. {2016}{Long} samples.*

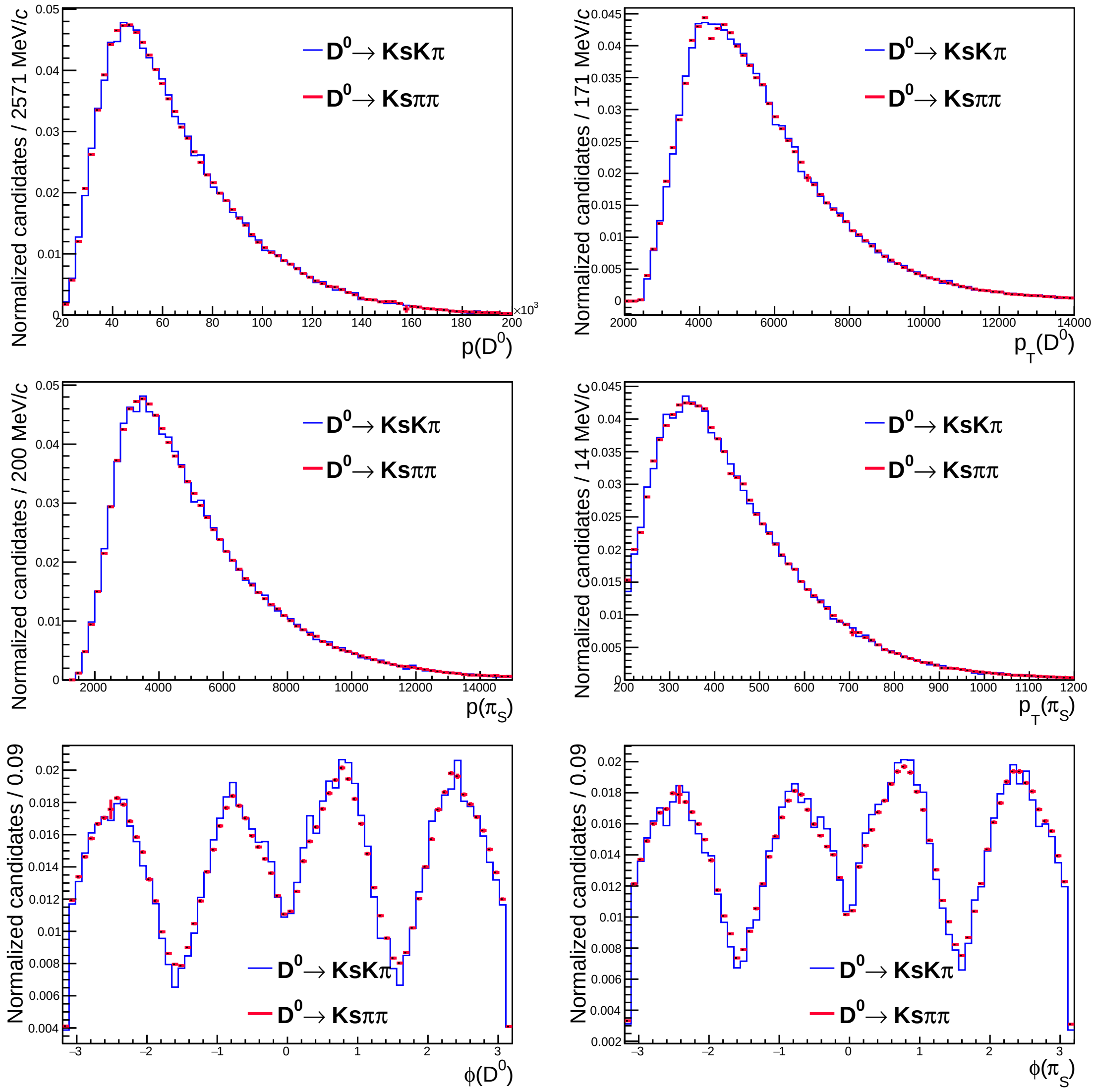

Figure 6.4: *Comparison of the time-integrated normalized variables between the $D^0 \to K^0_S K\pi$ WS signal mode and $D^0 \to K^0_S \pi\pi$ calibration mode, after the re-weighting procedure. {2016}{Long} samples.*

In addition to the variables related to the D^0 and the soft pion kinematics, the App. C.1 also reports the comparison for extra variables providing information about the kinematics of the $K\pi$ and $\pi\pi$ pairs, for the signal and calibration mode, respectively. In order to describe the kinematics of the pair, h_1^+, h_2^-, where h stands for pions or kaons, the following variables are defined

$$A_p := \frac{p_1 - p_2}{p_1 + p_2}, \tag{6.5}$$

$$A_\eta := \frac{\eta_1 - \eta_2}{\eta_1 + \eta_2}, \tag{6.6}$$

$$p_{TOT} := p_1 + p_2, \tag{6.7}$$

$$\eta_{TOT} := \eta_1 + \eta_2, \tag{6.8}$$

where p_1 and p_2 (η_1 and η_2) refer to the 3D momentum (pseudo-rapidity) of the h_1^+ and h_2^- particles, respectively. This is just a re-parameterization of the common variables $(p_1, p_2, \eta_1, \eta_2)$ where any possible dependence on the azimuthal angles (ϕ_1, ϕ_2) is neglected assuming LHCb to be perfectly symmetric under rotation around the z axis (beam axis). The A_p and A_η variables are the charged asymmetries of the momentum and of the pseudo-rapidity of the pair, and are by construction almost independent of p_{tot} and η_{tot} variables. Since the two pairs of interest ($K\pi$ and $\pi\pi$) are different, it is expected that A_p and A_η have different distributions between the signal and calibration modes. Instead, the p_{TOT} and η_{TOT} variables are expected to be equalized, after the re-weighting procedure, because they are strictly correlated to the momentum of the D^0 candidate. This re-parameterization is introduced to allow a simpler equalization of the kinematics of the $K\pi$ pair of the $D^0 \to K_S^0 K\pi$ signal decays to that one of the two-body $D^0 \to K\pi$ decays, in order to measure the $A_D(K\pi)$. The determination of this term is, however, in progress, and it is not covered in this thesis work[3].

The distributions displayed in App. C are equalized between signal and control mode, in each bin of K_S^0 proper decay time, except for the distributions of A_p and A_η, as expected. This procedure ensures that the production asymmetry $A_P(D^*)$ and the detection asymmetry $A_D(\pi_s)$ cancel out in each proper decay-time bin, allowing a reliable determination of the difference of raw asymmetries.

6.5 Measurement of the raw asymmetries

The raw asymmetry is determined using the Eq. 2.33, and it can be written as

$$A_{raw} = \frac{N(D^0) - N(\overline{D}^0)}{N(D^0) + N(\overline{D}^0)}, \tag{6.9}$$

where $N(D^0)$ and $N(\overline{D}^0)$ are the numbers of D^0 and $\overline{D}^0$ reconstructed candidates, respectively. After the removal of the combinatorial background and after the re-weighting of the two kinematics, the number of D^0 ($\overline{D}^0$) candidates can be determined through a count of the weighted histograms, in the Δm signal region $[144.625, 146.125]$ MeV$/c^2$. Since each event (i) is associated to a total weight (w_i) [4], the value of $N(D^0)$ and $N(\overline{D}^0)$

[3] Details on $A_D(K\pi)$ are also reported on Chapt. 8.

[4] w_i is determined as the product between the weights of the background subtraction (w_i^s) and of the re-weighting procedure (w_i^r). The latter weights are different from the unity only for the $D^0 \to K_S^0 \pi\pi$ calibration mode.

are

$$N(x) = \sum_i w_i(x), \tag{6.10}$$

where x stands for D^0 and $\overline{D}^0$. Assuming $N(x)$ as a sum of weighted Poisson counts, the statistical uncertainty can be computed as [49]

$$\delta N(x) = \sqrt{\sum_i w_i^2(x)}. \tag{6.11}$$

Applying the standard error propagation equation to Eq. 6.9, the final statistical uncertainty on the raw asymmetry A_{raw} (δA_{raw}) is computed as

$$\delta A_{raw} = \sqrt{\sum_x \left(\frac{\partial A_{raw}}{\partial N(x)} \delta N(x) \right)^2}. \tag{6.12}$$

In order to perform a time-dependent analysis, A_{raw} is measured in each K_S^0 proper decay-time bin separately, both for the signal modes ($D^0 \to K_S^0 K\pi$ RS or WS decays) and the calibration mode ($D^0 \to K_S^0 \pi\pi$). Each measured value of the raw asymmetry is associated to the average value, $\langle t \rangle$, of the proper decay time of each bin.

The results shown in this thesis are blinded, in order to avoid the *experimenter's bias*, *i.e.* the unintended influence on a measurement towards prior results or theoretical expectations [50]. Therefore, two different unknown (constant over time) uniform random numbers are added to the $A_{raw}^{RS}(t)$ and to $A_{raw}^{WS}(t)$, respectively. This allows to blind the two individual measurements of ΔA_{raw}, both for WS and RS decays, but also their difference[5]. The raw asymmetry for the calibration mode is, instead, not blinded.

Figure 6.5 shows the measured raw asymmetries as a function of the proper decay time, for the full LHCb Run 2 data sample, for RS (A_{raw}^{RS}, blue), WS (A_{raw}^{WS}, red) signal decays and for the $D^0 \to K_S^0 \pi\pi$ decays ($A_{raw}^{\pi\pi}$, green). Bins for Long and Down K_S^0 data

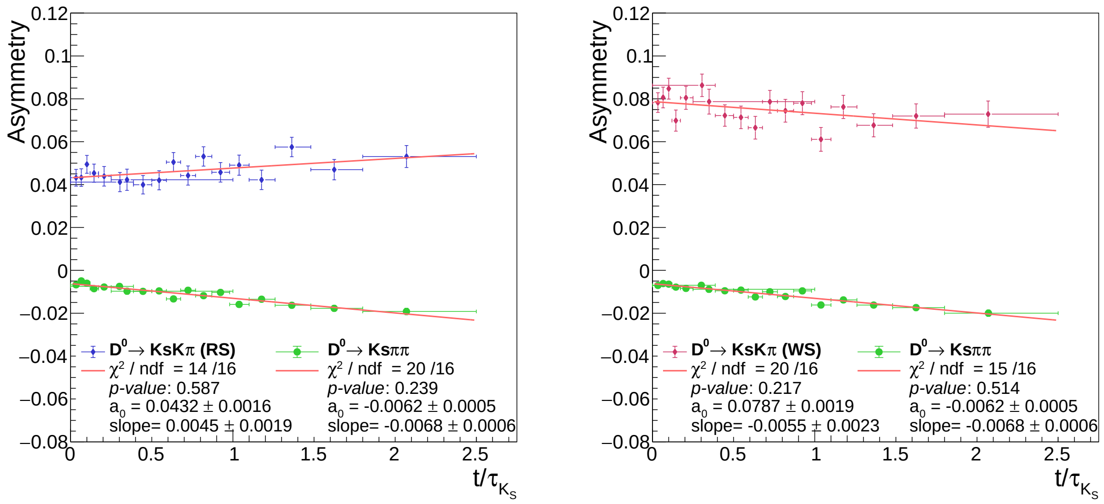

Figure 6.5: *Left: Blinded results of the $A_{raw}^{RS}(t)$ compered with the $A_{raw}^{\pi\pi}(t)$. Right: Blinded results of the $A_{raw}^{WS}(t)$ compered with the $A_{raw}^{\pi\pi}(t)$. A linear fit to data returns the coefficient a_0, corresponding to the $A_{raw}(t=0)$, and the slope. The full Run 2 data sample is used.*

sample are reported and fitted all together to a linear function. A minimum χ^2 fit is

[5] In the vicinity of the K^{*0} resonance one expects that $A_{CP}(RS) = -A_{CP}(WS)$.

performed and uncertainties on $\langle t \rangle$ values, for each bin, are small and are neglected in the minimization.

The raw asymmetry as function of the K^0_S decay time is also measured for all the sub-samples {WS, RS, $\pi\pi$}{2016, 2017, 2018} separately. The results are shown in App. C.2, while the slope and the intercept values returned from each fit, are listed in Tab. 6.2. The agreement with data is very good, as one can see from the χ^2/ndf

Table 6.2: *Blinded results for $A^{RS,WS,\pi\pi}_{raw}$ as a function of K^0_S proper decay time. A linear fit to data returns the coefficient a_0, corresponding to the $A_{raw}(t=0)$ and the slope.*

		$K^0_S K\pi$ (RS) $\times 10^{-3}$	$K^0_S K\pi$ (WS) $\times 10^{-3}$	$K^0_S \pi\pi$ $\times 10^{-3}$
2016	a_0	41.6 ± 3.2	86.3 ± 3.7	-6.0 ± 1.0
	slope	6.6 ± 3.8	-11.4 ± 4.5	-6.9 ± 1.2
	χ^2/ndf	$14/16$	$24/16$	$19/16$
2017	a_0	44.7 ± 2.9	74.6 ± 3.4	-7.0 ± 0.9
	slope	-0.6 ± 3.5	-3.3 ± 4.1	-5.4 ± 1.1
	χ^2/ndf	$10/16$	$16/16$	$22/16$
2018	a_0	43.0 ± 2.8	76.7 ± 3.3	-5.6 ± 0.9
	slope	7.7 ± 3.4	-2.9 ± 3.9	-8.2 ± 1.0
	χ^2/ndf	$25/16$	$19/16$	$14/16$
TOTAL	a_0	43.2 ± 1.6	78.7 ± 1.9	-6.2 ± 0.5
	slope	4.5 ± 1.9	-5.5 ± 2.3	-6.8 ± 0.6
	χ^2/ndf	$14/16$	$20/16$	$15/16$

values. In particular the linear fit to the calibration mode, with a total statistics of about 12 M of $D^0 \to K^0_S \pi\pi$ decays, confirms that the behaviour of the $A_D(K^0)$ can be assumed linear as function of proper decay time up to $2.5\tau_{K^0_S}$, with an excellent level of accuracy. Moreover, a confirmation of the relation in Eq. 2.38 is given by the observed specular behavior between the RS and WS samples. In fact, the $A^{RS}_{raw}(t)$ sample has positive slope equal to $(4.5 \pm 1.9) \times 10^{-3}$, while the $A^{WS}_{raw}(t)$ displays a negative slope equal to $(-5.5 \pm 2.3) \times 10^{-3}$. The two slopes are equal and opposite within the error, hence the approximation

$$A^{RS}_D(K^0) \approx -A^{WS}_D(K^0) \tag{6.13}$$

is validated using data with an excellent level of accuracy. It is also worth noting that the slope of $A^{WS}_{raw}(t)$ returns to be compatible with the slope of the calibration mode, equal to $A^{\pi\pi}_{raw}(t) = (-6.8 \pm 0.6) \times 10^{-3}$ confirming that

$$A^{WS}_D(K^0) \approx A^{\pi\pi}_D(K^0), \tag{6.14}$$

also in this case with an excellent level of accuracy. In conclusion data supports the validity of the following relation

$$A^{\pi\pi}_D(K^0) \approx A^{WS}_D(K^0) \approx -A^{RS}_D(K^0), \tag{6.15}$$

within the available statistical power.

6.6 Measurement of ΔA_{raw}

The difference of the two raw asymmetries, $\Delta A^{RS(WS)}_{raw}(t)$, are shown in Fig. 6.6 for both RS and WS signal samples. They are fitted to a linear function and the returned p-values

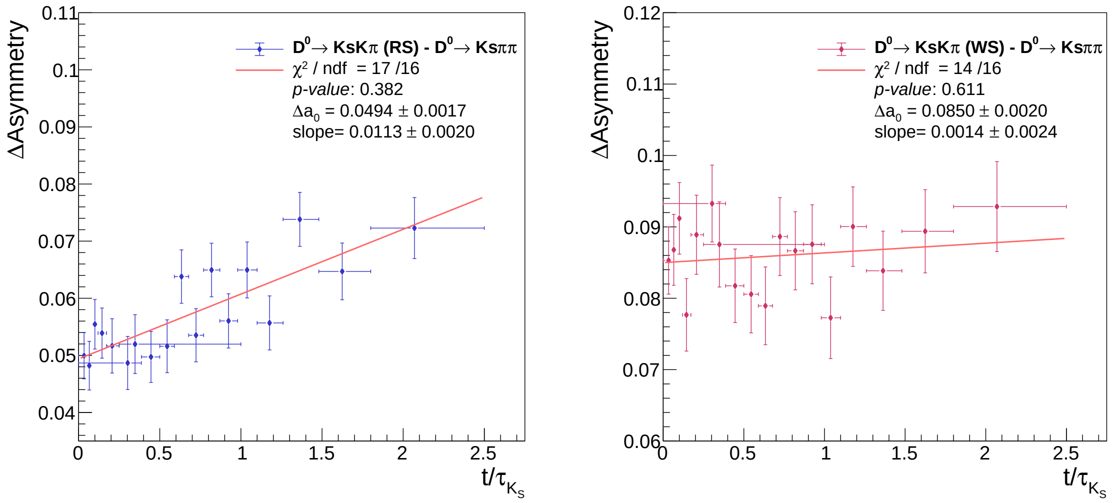

Figure 6.6: *Left: blinded results for ΔA^{RS}_{raw} as a function of K^0_S proper decay time. Right: blinded results for ΔA^{WS}_{raw} as a function of K^0_S proper decay time. A linear fit to data returns the coefficient Δa_0, corresponding to the $\Delta A_{raw}(t=0)$, and the slope. The full Run 2 data sample is used.*

show a very good agreement with the model. The values of $\Delta A^{RS(WS)}_{raw}(t)$ are measured for all the available years of data taking, as shown in App. C.3. The slope and the intercept values returned from each linear fit are reported in Tab. 6.3, separately for the RS and WS signal samples. The statistical uncertainty on the $\Delta A_{raw}(t=0)$ measurement is of 1.7×10^{-3} using the full RS sample and 2.0×10^{-3} using the full WS sample.

The value of the slope returned from the fit to the $\Delta A^{WS}_{raw}(t)$ is consistent with zero, as expected from the linear fits to the individual raw asymmetries. This means that, at this level of precision, no deviations are observed from the following approximation

$$A^{\pi\pi}_D(K^0) \approx A^{WS}_D(K^0). \tag{6.16}$$

Hence, considering also Eq. 6.13, follows that

$$A^{\pi\pi}_D(K^0) \approx -A^{RS}_D(K^0), \tag{6.17}$$

therefore one expects that the slope of ΔA^{RS}_{raw}, $(11.3 \pm 2.0) \times 10^{-3}$ from Tab. 6.3, has to be approximately equal to about two times the opposite of the slope of the raw asymmetry $A^{\pi\pi}_{raw}$, $(-6.8 \pm 0.6) \times 10^{-3}$ from Tab. 6.2. Also in this case, this is confirmed by the data at a good level of precision.

Table 6.3: *Blinded results for $\Delta A_{raw}^{RS,WS}$ as a function of K_S^0 proper decay time. A constant fit to data returns the coefficient Δa_0, corresponding to the $\Delta A_{raw}(t=0)$ and the slope.*

		linear fit	
		$K_S^0 K\pi$ (RS) $\times 10^{-3}$	$K_S^0 K\pi$ (WS) $\times 10^{-3}$
2016	Δa_0	47.2 ± 3.3	92.5 ± 3.9
	slope	12.8 ± 4.0	-4.8 ± 4.7
	χ^2/ndf	$12/16$	$23/16$
2017	Δa_0	51.5 ± 3.1	81.7 ± 3.5
	slope	5.1 ± 3.7	2.1 ± 4.2
	χ^2/ndf	$16/16$	$13/16$
2018	Δa_0	48.8 ± 3.0	82.2 ± 3.4
	slope	15.8 ± 3.5	5.4 ± 4.0
	χ^2/ndf	$23/16$	$16/16$
TOTAL	Δa_0	49.4 ± 1.7	85.0 ± 2.0
	slope	11.3 ± 2.0	1.4 ± 2.4
	χ^2/ndf	$17/16$	$14/16$

6.7 Possible enhancement of ΔA_{raw} sensitivity

As mentioned above, data confirms the validity of the relation in Eq. 6.15

$$A_D^{\pi\pi}(K^0) \approx A_D^{WS}(K^0) \approx -A_D^{RS}(K^0). \tag{6.18}$$

Therefore, it is possible to enhance the sensitivity of the measurement of ΔA_{raw}, both for RS and WS signal decays, fitting the data to a constant values. For the WS signal sample this is straightforward, since one assumes that $A_D^{\pi\pi}(K^0) = A_D^{WS}(K^0)$, and the linear behaviour of the two individual raw asymmetries cancels out in the difference. For the RS, instead, it is necessary to reverse the sign of the slope of the raw asymmetry of the calibration mode, keeping the same value for the intercept coefficient. Thus, an axial symmetry transformation of the data points of the calibration mode around the measured value of $A_{raw}^{\pi\pi}(t=0)$, is performed. Figure 6.7 shows the reversed $A_{raw}^{\pi\pi}(t)$ data (green) and those for the signal RS decays, the same as in Fig. 6.5, on the left hand side.

It is now possible to determine the difference of the two raw asymmetries, between the $A_{raw}^{RS}(t)$ and the reversed $A_{raw}^{\pi\pi}(t)$. The resulting data are fitted to a constant function. Table 6.4 reports the final results together with the χ^2/ndf for each fit, over all years for RS and WS signal decays, separately. Figure 6.8 shows the fit to the full RS and WS $\Delta A_{raw}(t)$, as an example. The agreement of the data with the constant model is satisfactory as one can infer from both the returned χ^2 and the p-values. The same figures, separately for each year, can be found in App. C.3.

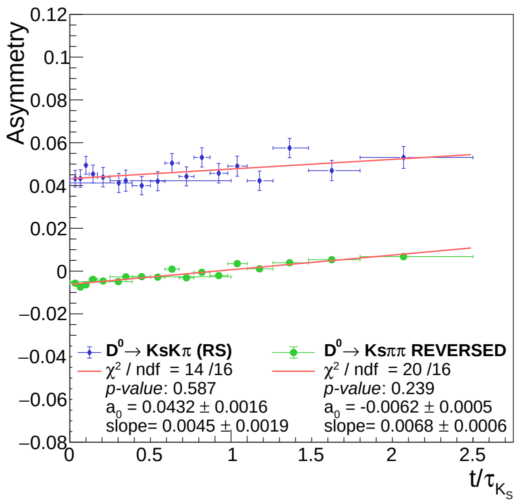

Figure 6.7: *Blinded $A^{RS}_{raw}(t)$ compared with the $A^{\pi\pi}_{raw}(t)$. The data points of the calibration mode are reversed according the assumption $A^{\pi\pi}_D(K^0) = -A^{RS}_D(K^0)$ as described in the text. A linear fit is superimposed to determine the coefficient a_0 ($A_{raw}(t=0)$) and the slope for both decay modes.*

The approximation of Eq. 6.18 allows to enhance the precision on the measurement of the observable $\Delta A^{RS(WS)}_{raw}$. The statistical uncertainty on the measurement of ΔA^{RS}_{raw} moves from 1.7×10^{-3} to 1.1×10^{-3}, while the statistical uncertainty on ΔA^{WS}_{raw} moves from 2.0×10^{-3} to 1.3×10^{-3}. These are very promising results allowing to search for *CP*

Table 6.4: *Blinded results for $\Delta A^{RS,WS}_{raw}$ as a function of K^0_S proper decay time. A constant fit to data returns the coefficient Δa_0, corresponding to the $\Delta A_{raw}(t=0)$ and the slope. The $A^{\pi\pi}_{raw}(t)$ is reversed before to perform the difference with the $A^{RS}_{raw}(t)$, as described in the text.*

		constant fit	
		$K^0_S K\pi$ (RS) $\times 10^{-3}$ REVERSED	$K^0_S K\pi$ (WS) $\times 10^{-3}$
2016	Δa_0	47.4 ± 2.2	89.5 ± 2.5
	χ^2/ndf	$16/17$	$24/17$
2017	Δa_0	47.3 ± 2.0	83.0 ± 2.3
	χ^2/ndf	$9/17$	$14/17$
2018	Δa_0	48.8 ± 1.9	85.7 ± 2.2
	χ^2/ndf	$23/17$	$18/17$
TOTAL	Δa_0	47.9 ± 1.1	85.9 ± 1.3
	χ^2/ndf	$13/17$	$14/17$

violation over the full Dalitz plot with an accuracy at the per mil level, both for RS and WS signal decays. It is worth noting that the systematic uncertainty, probably much smaller than the current statistical uncertainty, must be assessed on the assumption, $A^{\pi\pi}_D(K^0) \approx A^{WS}_D(K^0) \approx -A^{RS}_D(K^0)$, to obtain such an enhancement. It requires detailed studies to quantify the size of the suppressed processes that could break the approximation. This is

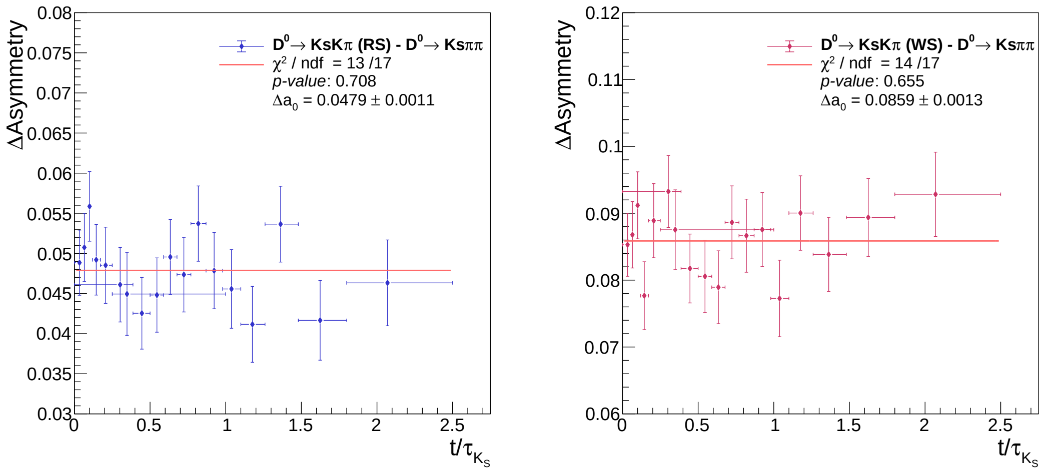

Figure 6.8: *Left: blinded results for ΔA^{RS}_{raw} as a function of K^0_S proper decay time. Right: blinded results for ΔA^{WS}_{raw} as a function of K^0_S proper decay time. A linear fit to data returns the coefficient Δa_0, corresponding to the $\Delta A_{raw}(t=0)$, and the slope. The $A^{\pi\pi}_{raw}(t)$ is reversed before to perform the difference with the $A^{RS}_{raw}(t)$, as described in the text.*

beyond the scope of this thesis.

The last ingredient to extract A_{CP} for RS and WS decays, from the ΔA_{raw} measurements, is the measurement of the detection asymmetry $A_D(K\pi) = A^{RS}_D(K\pi) \approx -A^{WS}_D(K\pi)$. As explained in the Sect. 2.3, this term can be determined using a similar ΔA_{raw} cancellation mechanism between $D^0 \to K^-\pi^+$ and $D^0 \to \pi^+\pi^-$, after an appropriate re-weighting of the kinematics of the $K\pi$ pair. In particular the two-body $D^0 \to K\pi$ decays is re-weighted to the $D^0 \to K^0_S K\pi$ decays. The size of this term is of about 1%, as it can be seen from Ref. [51]. At the current level of precision this term can be assumed to be independent of the specific K^0_S proper decay-time bin, and, therefore, it is just a simple translation of the measured ΔA_{raw}. The variations of the kinematics of the $K\pi$ pair as a function of the different time bins can be considered as a second order effect. However, a systematic uncertainty, due to this approximation, is briefly discussed in Sect 8.1.

7 Measurement of ΔA_{raw} in the vicinity of the K^{*0}

This chapter describes the measurement of $\Delta A_{raw}^{RS(WS)}$ in the vicinity of the $K^*(892)^0$ resonance. The fist part of the chapter is focused on how the DP region around the $K^{*0} \to K\pi$ resonance is selected. Then, the blind measurement ΔA_{raw} is presented. The same method developed for the measurement integrated over the full DP is used.

7.1 Selection of the region around the K^{*0} resonance

This section describes how a restricted region, enriched with $K^*(892)^0 \to K^+\pi^-$ decays, is selected. Figure 7.1 shows the Dalitz distributions of the $D^0 \to K^0_S K^-\pi^+$ RS (on the left) and $D^0 \to K^0_S K^+\pi^-$ WS (on the right) signal decays, after the removal of the Δm combinatorial background. The offline selection is unchanged, with respect to that one used for the analysis of the full Dalitz plot, as reported in Tab. 5.8. Figures 7.2 and 7.3 show, instead, the projections of the 2D distributions along the two axes of the Dalitz plots, both for the RS and WS signal decays. The intermediate $K^*(892)^0 \to K^+\pi^-$ resonance is visible as a destructive interference at low values of $m^2(K^-\pi^+)$ in the RS decays, while an evident peaking structure is visible in the WS decays, at the same value of $m^2(K^+\pi^-) \approx (892)^2$ MeV$^2/c^4$. It is also possible to recognize others intermediate resonances, contributing to the $D^0 \to K^0_S K\pi$ decay channel (see Sect. 2.2), such as the $K^*(892)\pm \to K^0_S\pi^\pm$ at low values of $m^2(K^0_S\pi^\pm)$, in both RS and WS decays.

In order to select a region enriched of $K^{*0} \to K\pi$ decays, the signal peak visible in the WS sample is used. A 2σ region around the peak is chosen, as shown on the left hand side of Fig. 7.4. Furthermore, a veto requirement for the abundant $K^{*\pm} \to K^0_S\pi^\pm$ is implemented, in order to remove those decays from the final data sample. The selected $m^2(K^0_S\pi^-)$ vetoed region is shown in Fig. 7.4, on the right side, between the two vertical lines. Thus, the requirements used to select an enriched sample with $K^{*0} \to K\pi$ decays are the following:

- $m^2(K^+\pi^-) \in [716, 860] \times 10^3$ MeV$^2/c^4$
- $m^2(K^0_S\pi^-) > 850 \times 10^3$ MeV$^2/c^4$ `OR` $m^2(K^0_S\pi^-) < 600 \times 10^3$ MeV$^2/c^4$.

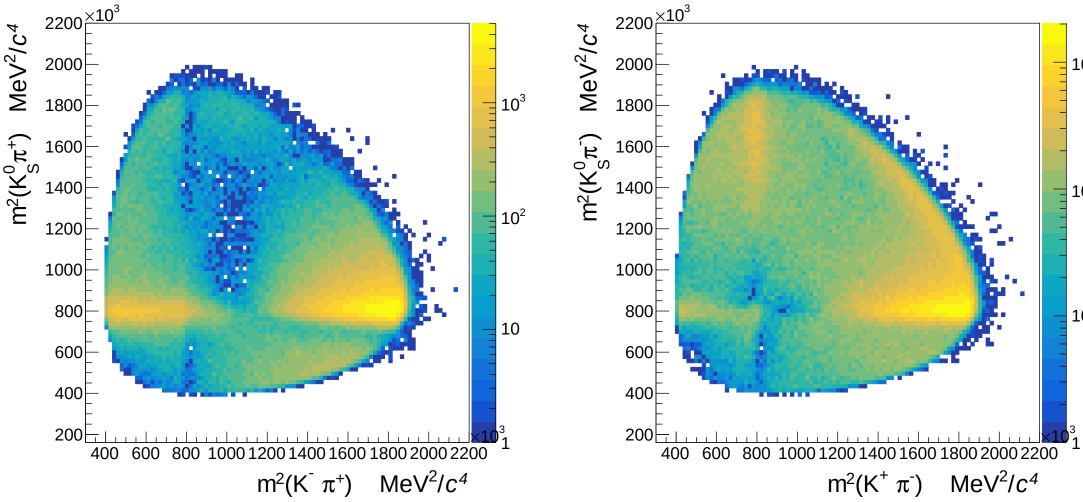

Figure 7.1: *Left: DP distribution of the $D^0 \to K^0_S K^- \pi^+$ decay channel (RS). Right: DP of the $D^0 \to K^0_S K^+ \pi^-$ decay channel (WS).*

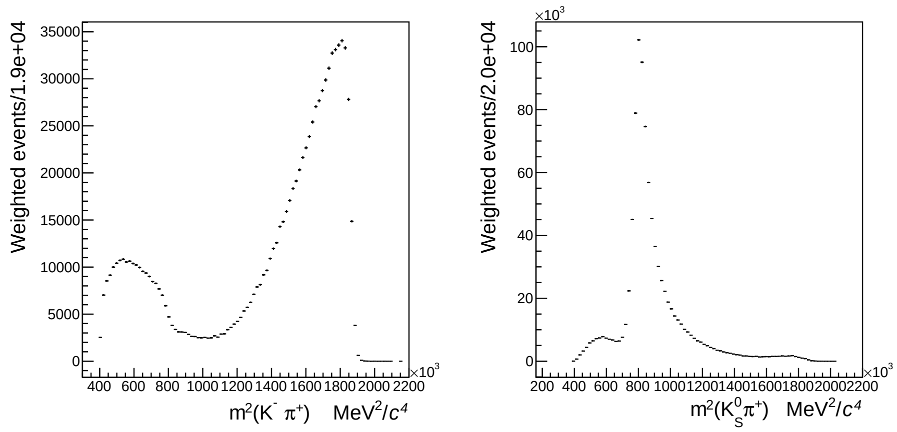

Figure 7.2: *Projections of the RS Dalitz plot.*

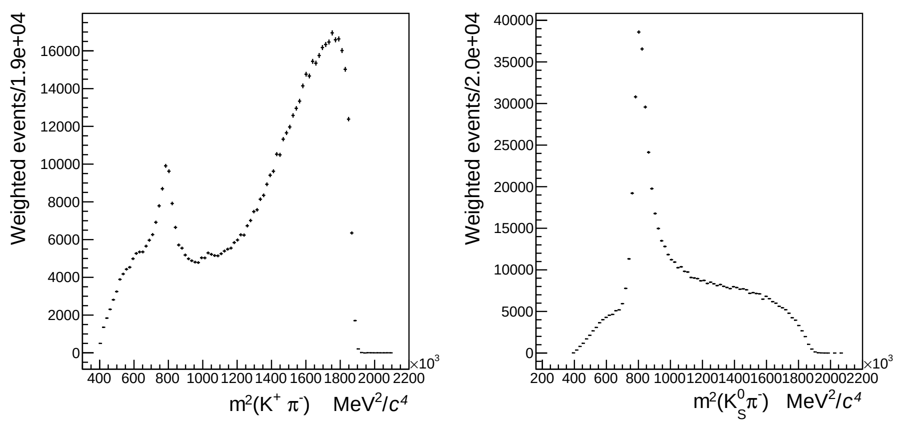

Figure 7.3: *Projections of the WS Dalitz plot.*

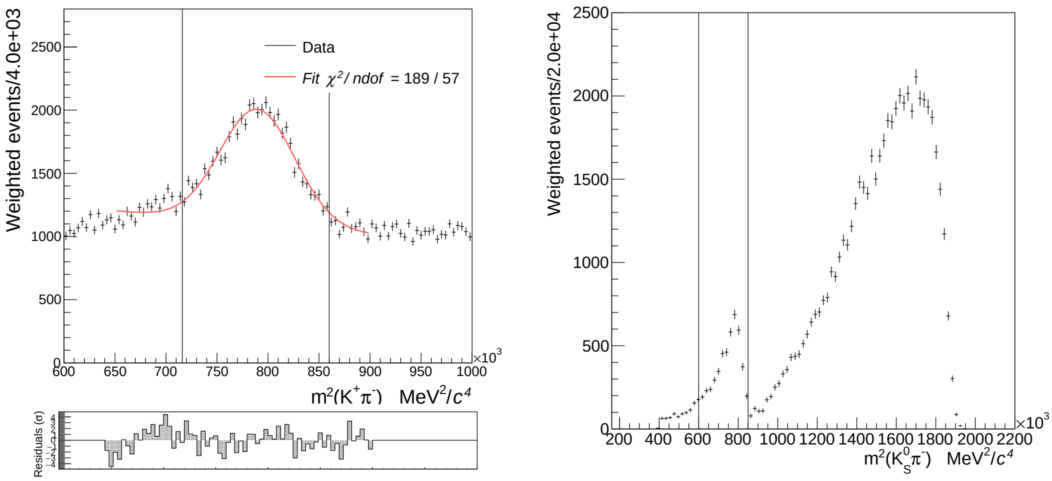

Figure 7.4: *Left: Projection of the DP of WS signal decays in the restricted range* $m^2(K^+\pi^-) \in [600, 1000] \times 10^3$. *The* $K^{*0} \to K\pi$ *mass peak is fitted to a Gaussian function plus a linear background. The two vertical lines enclose the* 2σ *region around the peak. Normalized residuals are displayed in the insets. Right: projection of the DP of WS signal decays in the* $m^2(K^0_S\pi^-)$ *distribution, where the requirement* $m^2(K^+\pi^-) \in [716, 860] \times 10^3$ *MeV*$^2/c^4$ *is applied. The two vertical lines enclose the* $m(K^0_S\pi^-)$ *vetoed region.*

It is now possible to determine the signal yields in a region enriched with $D^0 \to \overline{K}^0 K^{*0} \to K^0_S K^+\pi^-$ and $D^0 \to K^0\overline{K}^{*0} \to K^0_S K^-\pi^+$ decays. The numbers of the total reconstructed RS and WS signal decays are reported in Tab. 7.1. They are obtained by fitting the invariant Δm mass distribution, as shown in Fig. 7.5.

Table 7.1: *Signal yields of the* $D^0 \to K^0_S K\pi$ *decays in the selected region enriched of* $K^{*0} \to K\pi$ *decays.*

	K^{*0}	full Dalitz
RS	22k	1044k
WS	61.5k	718k

The method used to measure the $\Delta A_{CP}^{RS(WS)}$ observable in the vicinity of the $K^{*0} \to K\pi$ resonance is the same of that one used for the analysis of the full DP, as described in Chapt. 6. Hence, firstly the combinatorial background is removed by means a Δm sideband subtraction (as described in Sect. 6.3). Furthermore, the kinematic distribution, of the 3D space $p(D^0)$, $p_T(D^0)$ and $p_T(\pi_s)$, of the $D^* \to D^0\pi_s \to [K^0_S\pi\pi]\pi_s$ decay mode is re-weighted to that of the $D^* \to D^0\pi_s \to [K^0_S K\pi]\pi_s$ decay mode, in order to allow a reliable cancellation of the $A_P(D^*)$ and $A_D(\pi_s)$ asymmetry terms. The weighting rule previously determined, used for the full DP domain, returned to be accurate also in the restricted region around the $K^{*0} \to K\pi$ resonance, as shown in Fig. 7.6.

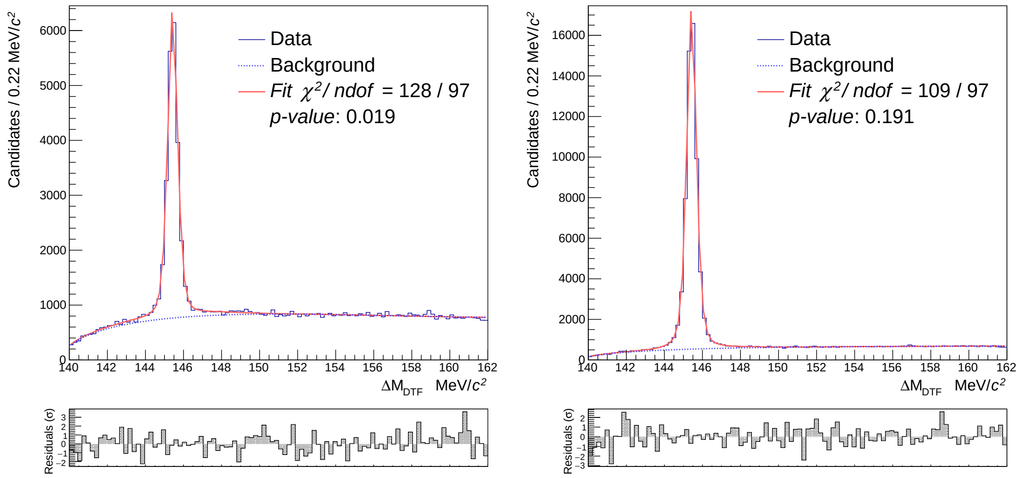

Figure 7.5: *Invariant Δm mass distributions for D^0 candidates selected in the restricted $K^{*0} \to k\pi$ region. Left: RS decays distribution. Right: WS decays distributions. The result of the fit is superimposed.*

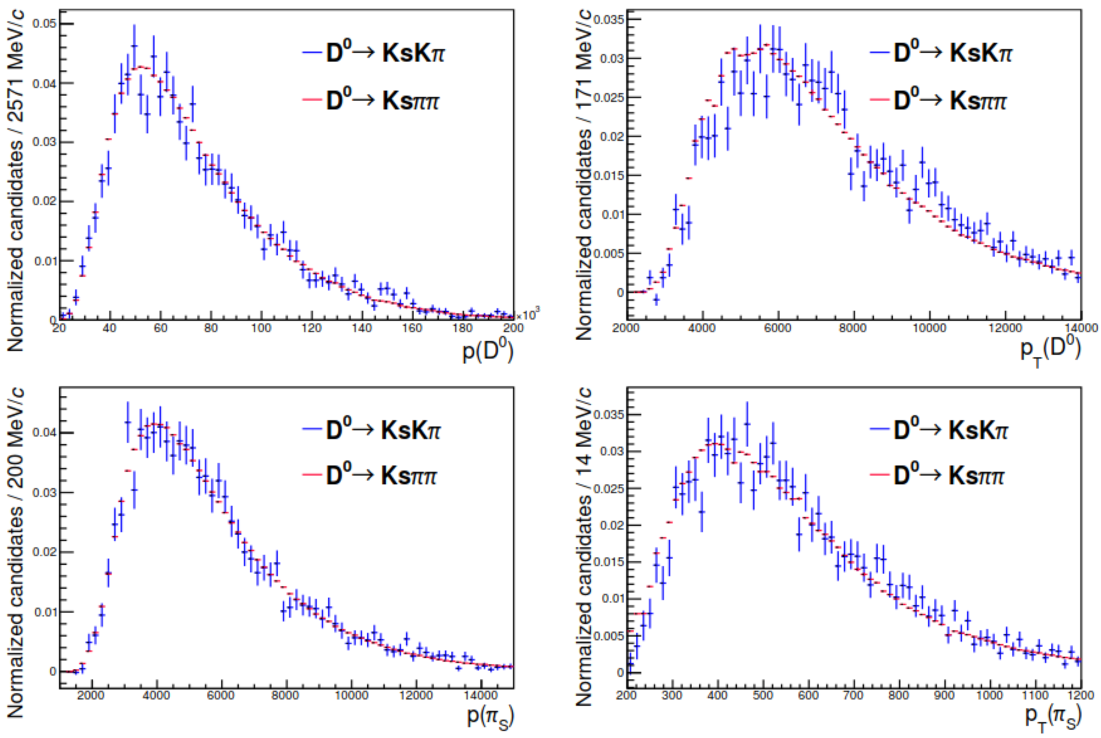

Figure 7.6: *Comparison between the $D^0 \to K^0_S K\pi$ (blue) and re-weighted $D^0 \to K^0_S\pi\pi$ (red) kinematic distributions. The selection around the K^{*0} is applied to the $D^0 \to K^0_S K\pi$ sample. {2018}{D} samples.*

7.2 Time-dependent raw *CP* asymmetries

The same procedure described in Sect. 6.5 is applied in order to determine $A_{raw}^{RS(WS)}$ using the data samples enriched with the presence of $K^{*0} \to K\pi$ decays. Hence, the number of D^0 ($\overline{D}^0$) candidates is measured by means a simple count of the weighted histograms, in the Δm signal region, $\Delta m \in [144.625, 146.125]$ MeV$/c^2$. In order to perform the time-dependent analysis, A_{raw} is measured in each K_S^0 proper decay-time bin. The bin definitions is the same as that one used for the time-dependent measurement over the full DP. Each measured value of the raw asymmetry is associated to the average value of the proper decay time of each bin, $\langle t \rangle$. The results are blinded in order to avoid the experimenter's bias, as explained in Sect. 6.5. Figure 7.7 shows the measured raw asymmetries as a function of the proper decay time for the full LHCb Run 2 data sample. In particular, the RS (A_{raw}^{RS}, blue), WS (A_{raw}^{WS}, red), and $D^0 \to K_S^0\pi\pi$ ($A_{raw}^{\pi\pi}$, green) decay modes are reported. Bins for Long and Downstream K_S^0 data samples are reported and fitted all together to a linear function. As described in the previous chapter, this is a minimum χ^2 fit where uncertainties on $\langle t \rangle$ values, for each bin, can be safely neglected in the minimization. The raw asymmetry as a function of the K_S^0 decay time is also

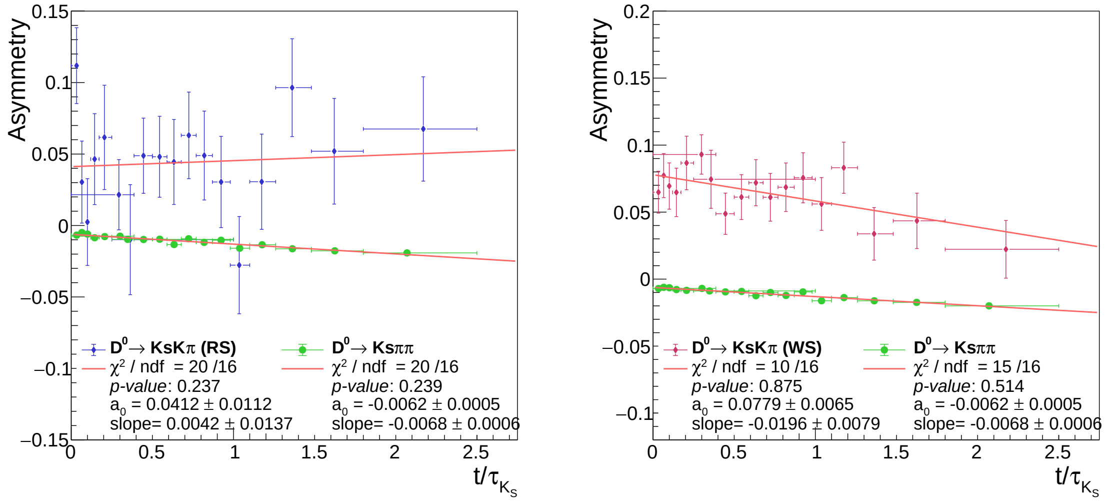

Figure 7.7: *Left: Blinded results of the $A_{raw}^{RS}(t)$ compered with the $A_{raw}^{\pi\pi}(t)$. Right: Blinded results of the $A_{raw}^{WS}(t)$ compered with the $A_{raw}^{\pi\pi}(t)$. A linear fit to data returns the coefficient a_0, corresponding to the $A_{raw}(t=0)$, and the slope. The full Run 2 data sample is used. The RS and WS data samples are selected in a restricted region around the $K^{*0} \to K\pi$ resonance.*

measured for all the sub-samples {WS, RS, $\pi\pi$}{2016, 2017, 2018}, separately. The results of the fits are summarized in Tab. 7.2.

Table 7.2: *Blinded results for $A_{raw}^{RS,WS,\pi\pi}$ as a function of K_S^0 proper decay time in the K^{*0} restricted region. A linear fit to data returns the coefficient a_0, corresponding to the $A_{raw}(t=0)$ and the slope.*

		$K_S^0 K\pi$ (RS) $\times 10^{-3}$	$K_S^0 K\pi$ (WS) $\times 10^{-3}$	$K_S^0 \pi\pi$ $\times 10^{-3}$
2016	a_0	57.1 ± 23.9	80.4 ± 12.6	-6.0 ± 1.0
	slope	-3.8 ± 31.4	-31.3 ± 15.9	-6.9 ± 1.2
	χ^2/ndf	23/16	23/16	19/16
2017	a_0	49.9 ± 22.0	70.5 ± 11.5	-7.0 ± 0.9
	slope	-25.3 ± 28.4	-13.8 ± 14.0	-5.4 ± 1.1
	χ^2/ndf	13/16	20/16	22/16
2018	a_0	26.1 ± 21.0	82.5 ± 11.0	-5.6 ± 0.9
	slope	31.1 ± 26.5	-16.1 ± 13.4	-8.2 ± 1.0
	χ^2/ndf	13/16	11/16	14/16
TOTAL	a_0	41.2 ± 11.2	77.9 ± 6.5	-6.2 ± 0.5
	slope	4.2 ± 13.7	-19.6 ± 7.9	-6.8 ± 0.6
	χ^2/ndf	20/16	10/16	15/16

7.3 Measurement of the $\Delta A_{raw}^{RS(WS)}$ in the vicinity of the $K^{*0} \to K\pi$ resonance

The difference of the two raw asymmetries, ΔA_{raw}, are shown in Fig. 7.8, for the total RS and WS samples, on the left and right hand, respectively. They are fitted to a linear function and the returned p-values show a very good agreement between data and linear model. The $\Delta A_{raw}^{RS(WS)}(t)$ is measured for all the available years of data taking, and the fit results are reported in Tab. 7.3 for the RS and WS samples. As expected, the statistical uncertainty on the $\Delta A_{raw}(t=0)$ measurements, in this restricted region, is lesser than that obtained with the analysis of the full DP, in particular it moves from 1.7×10^{-3} to 11.2×10^{-3} using the RS sample, while it moves from 2.0×10^{-3} to 6.5×10^{-3} using the WS sample.

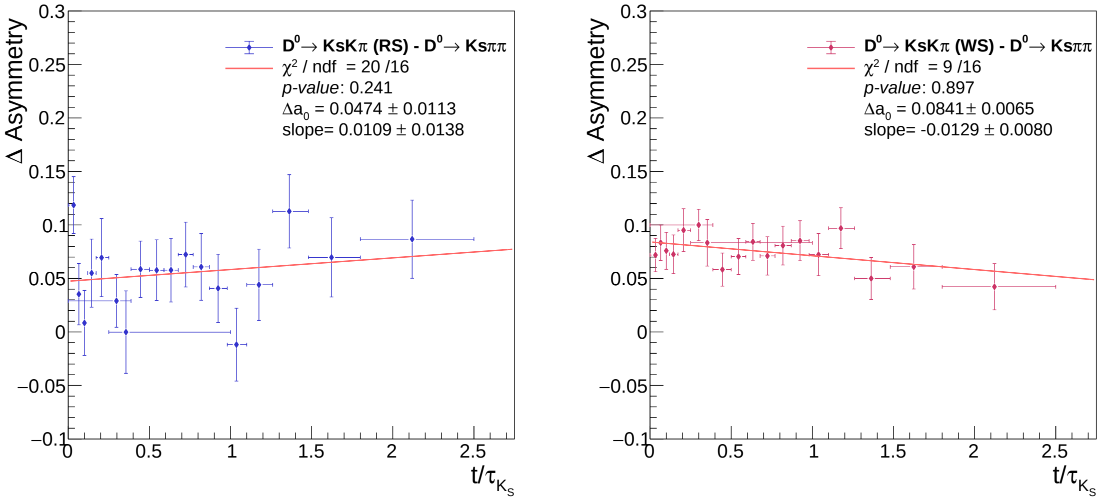

Figure 7.8: *Left: blinded results for ΔA^{RS}_{raw} as a function of K^0_S proper decay time. Right: blinded results for ΔA^{WS}_{raw} as a function of K^0_S proper decay time. A linear fit to data returns the coefficient Δa_0, corresponding to the $\Delta A_{raw}(t=0)$, and the slope. The full Run 2 data sample is used. The RS and WS data samples are selected in a restricted region around the $K^{*0} \to K\pi$ resonance.*

Table 7.3: *Blinded results for $\Delta A^{RS,WS}_{raw}$ as a function of K^0_S proper decay time in a restricted region around the $K^{*0} \to K\pi$ resonance. A constant fit to data returns the coefficient Δa_0, corresponding to the $\Delta A_{raw}(t=0)$ and the slope.*

		linear fit	
		$K^0_S K\pi$ (RS) $\times 10^{-3}$	$K^0_S K\pi$ (WS) $\times 10^{-3}$
2016	Δa_0	64.0 ± 24.0	87.2 ± 12.7
	slope	1.6 ± 31.8	-25.4 ± 16.1
	χ^2/ndf	$23/16$	$23/16$
2017	Δa_0	56.7 ± 22.1	77.1 ± 11.6
	slope	-19.3 ± 28.7	-8.2 ± 14.2
	χ^2/ndf	$13/16$	$19/16$
2018	Δa_0	31.4 ± 21.2	88.0 ± 11.1
	slope	40.0 ± 26.7	-8.0 ± 13.6
	χ^2/ndf	$12/16$	$11/16$
TOTAL	Δa_0	47.4 ± 11.3	84.1 ± 6.5
	slope	10.9 ± 13.8	-12.9 ± 8.0
	χ^2/ndf	$20/16$	$9/16$

7.4 Possible enhancement of sensitivity in ΔA_{raw}

As done for the analysis of the full DP, it is possible to exploit the relation of Eq. 6.18, to reverse the slope of the $A^{\pi\pi}_{raw}(t)$ to compute the difference of raw asymmetry, ΔA^{RS}_{raw}, for the RS sample. For the WS data sample no reversal is applied to the calibration sample. Figure 7.9 shows the reversed raw asymmetry $A^{\pi\pi}_{raw}$ (green) for the calibration mode, along with the raw asymmetry of the RS signal decays (the same as in Fig. 7.7, on the left hand side).

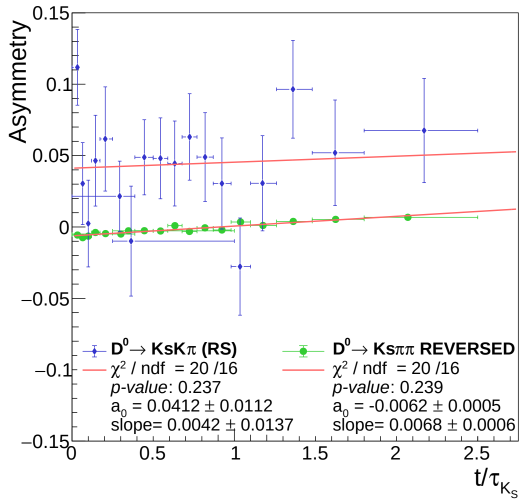

Figure 7.9: *Blinded $A^{RS}_{raw}(t)$ (blue data) as a function of K^0_S proper decay time, in the K^{*0} restricted region. The result for the reversed $A^{\pi\pi}_{raw}$ data is also superimposed (green data). A linear fit to data returns the coefficient a_0, corresponding to the $A^{RS,WS,\pi\pi}_{raw}(t=0)$.*

It is now possible to perform the difference between the $A^{RS}_{raw}(t)$ and the reversed $A^{\pi\pi}_{raw}(t)$ raw asymmetries. The resulting data are fitted to a constant function. Both the coefficients are reported in Tab. 7.4, together with the χ^2/ndf for each fit, over all years for RS and WS signal decays, separately. Figure 7.10 illustrates the fits to the full RS and WS $\Delta A_{raw}(t)$, as an example. The agreement of the data with the constant model is satisfactory as one can infer from both the returned χ^2 and p-values. The uncertainty on the ΔA^{RS}_{raw} measurement moves from 11.2×10^{-3} to 7.3×10^{-3}, for the RS sample. While, the uncertainty on the measurement of ΔA^{WS}_{raw} moves from 6.5×10^{-3} to 4.2×10^{-3}. The fact that the approximation of Eq. 6.18 is valid at an higher level of accuracy, as seen by performing the analysis over the full DP, it certainly allows its exploitation in this case, where the statistical uncertainties are larger than those obtained over the whole phase space. In other words, any systematic uncertainty, associated to the usage of this approximation, will have a smaller impact with respect to the measurement performed over the whole phase space.

Table 7.4: *Blinded results for $\Delta A_{raw}^{RS,WS}$ as a function of K_S^0 proper decay time in a restricted region around the $K^{*0} \to K\pi$ resonance. A constant fit to data returns the coefficient Δa_0, corresponding to the $\Delta A_{raw}(t=0)$. The $A_{raw}^{\pi\pi}(t)$ is reversed before to perform the difference with the $A_{raw}^{RS}(t)$, as described in the text.*

		constant fit	
		$K_S K\pi$ (RS) $\times 10^{-3}$ REVERSED	$K_S K\pi$ (WS) $\times 10^{-3}$
2016	Δa_0	56.7 ± 16.0	72.1 ± 8.3
	χ^2/ndf	$23/17$	$25/17$
2017	Δa_0	38.7 ± 14.4	72.0 ± 7.5
	χ^2/ndf	$14/17$	$19/17$
2018	Δa_0	46.1 ± 13.7	83.0 ± 7.2
	χ^2/ndf	$14/17$	$11/17$
TOTAL	Δa_0	45.8 ± 7.3	76.1 ± 4.2
	χ^2/ndf	$20/17$	$12/17$

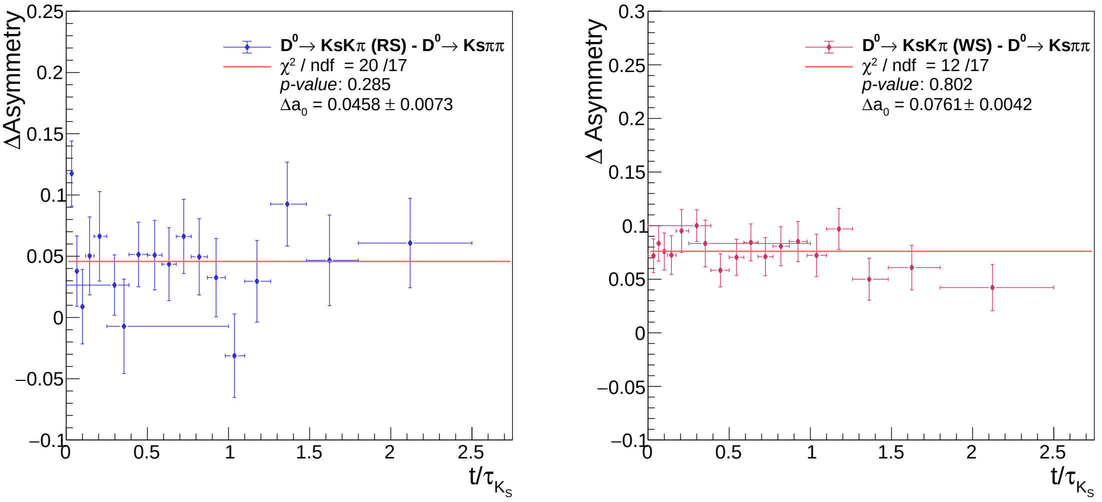

Figure 7.10: *Left: blinded results for ΔA_{raw}^{RS} as a function of K_S^0 proper decay time. Right: blinded results for ΔA_{raw}^{WS} as a function of K_S^0 proper decay time. A linear fit to data returns the coefficient Δa_0, corresponding to the $\Delta A_{raw}(t=0)$, and the slope. The $A_{raw}^{\pi\pi}(t)$ is reversed before to perform the difference with the $A_{raw}^{RS}(t)$, as described in the text. The RS and WS data samples are selected in a restricted region enhances of K^{*0} decays.*

8 Systematic uncertainties and conclusions

A brief overview of the possible dominant sources of systematic uncertainties is presented in this chapter. The final results are also presented, along with the conclusions of this thesis work.

8.1 Systematic uncertainties

The new analysis methodology developed in this thesis allows to explore precision up to the per mil level for the analysis over the all Dalitz plot and below the per cent level in the restricted region in the vicinity of the intermediate $K^*(982)^0 \to K\pi$ resonance. Although there was not enough time to make an accurate study of all possible systematic uncertainties and to make a precise determination of the $A_D(K\pi)$ asymmetry term, it is very important to briefly highlight the main sources of systematic uncertainties. The method is based on the very robust ΔA_{raw} cancellation mechanism[1] and, therefore, all uncertainties are expected to be smaller than the statistical uncertainties. Similarities with the measurement described in Ref. [3] are evident.

The fit model The knowledge of the signal and background mass models is the first source of systematic uncertainty that is considered. The p.d.f.s used in this thesis to determine the normalization factor f_s in order to remove the combinarorial background are empirical function. Hence, in order to evaluate the associated systematic uncertainty, it is necessary to repeat the fit using other different empirical models. The difference between the baseline results and those from some alternative fit models gives the value of such an uncertainty. We know that this kind of uncertainties are usually very small when the difference between similar decay channels is performed. From the studies performed in Ref.[3], it is evaluated to be $\mathcal{O}(10^{-4})$, one order of magnitude less than our statistical uncertainty.

Physics backgrounds The presence of different physical backgrounds between signal and calibration mode might generate spurious asymmetries that do not cancel out in the difference. The following list shows the main sources of physics backgrounds that might contribute to the signal and calibrations modes.

[1] Actually, it is a double ΔA_{raw} difference.

- The background of the $\boldsymbol{D^0 \to K_S^0 K\pi}$ decay channel receives contributions from the decays $D^0 \to K_S^0\pi^+\pi^-\pi^0$ and $D^0 \to K_S^0\pi^-\mu^+\nu_\mu$ due to the mis-identification of a charged kaon. Also the $D^0 \to K^-\pi^+\pi^+\pi^-$ background contributes, but it is suppressed by the baseline requirement $\log(\chi^2_{FD}) > 5$. A small contribution from the $D^0 \to K_S^0\pi^+\pi^-\pi^0$ remains in the Δm distribution [8].

- The $\boldsymbol{K_S^0\pi\pi}$ final state, of the three-body calibration mode, has backgrounds with mis-identified hadrons ($D^0 \to K_S^0 KK$ or $D^0 \to K_S^0 K\pi$) but they are suppressed by mass windows and PID cuts. The $D^0 \to \pi\pi\pi\pi$, where a pair of $\pi\pi$ has an invariant mass near to that of the K_S^0, are suppressed thanks to the $\log(\chi^2_{FD} > 5)$. Another physical background that might peak in the signal region is the semileptonic $D^0 \to K^{*-}\ell^+\overline{\nu_\ell}$, where ℓ stands for an electron or a muon. These backgrounds have branching ratios 1.89% and 2.15% respectively for the final state with the muon and the electron.

- The $\boldsymbol{D^0 \to K\pi}$ decay mode has sources of physics backgrounds from mis-reconstructed charm decays such as the $D^0 \to \pi^+\pi^-\pi^0$, the $D^0 \to \pi^+\pi^-$ and $D^0 \to K^+K^-$, and from semi-leptonic $D^0 \to K^-\ell^+\nu_\ell$ decays.

- The $\boldsymbol{D^0 \to \pi\pi}$ decay mode has the contribute from the $D^0 \to K^-\pi^+$, where the π^+ is misidentified with a kaon. Moreover, the $D^0 \to \pi^-\ell^+\nu_\ell$ contribute to the background, where the lepton is mis-identified with a pion and the neutrino is not reconstructed.

All these physics backgrounds are highly suppressed in the mass region of interest, with a residual contamination at the level of a few per mil. This kind of studies are already performed in Ref. [3], where the systematic uncertainty for the full Run 2 data sample is found to be 0.005%. Hence, a systematic uncertainty of the same level is expected for the measurement described in this thesis.

Re-weighting procedure Another source of systematic uncertainty accounts for the finite knowledge of the weights used in the kinematic weighting procedure. If the kinematic distributions between signal and calibration modes are not well aligned the nuisance detection and production asymmetries may not accurately cancel out in the difference. An associated systematic uncertainty has to be studied in order to account for the statistical uncertainties on the value of the weights (δw). A standard practice is to repeat the final measurement by sampling the values of the weights within their statistical uncertainties, and assessing as systematic uncertainty the standard deviation from the baseline. Also this uncertainty is expected to be small with respect to the statistical uncertainty achieved in this thesis because of the similarities between the signal and the calibration samples.

Contamination from secondary $\boldsymbol{D^0}$ A residual fraction of D^0 mesons coming from B decays (secondary decays) is still present in the final sample even after the application of the requirement that the D^0 trajectory points back to the PV (baseline cut $\chi^2_{IP} < 9$). However, a certain fraction of secondary decays, f_{sec}, can be still present [2]. Possible different levels of contamination between signal and calibration samples may bias the value of ΔA_{CP} because an incomplete cancellation of the charm meson production

[2]For two-body $D^0 \to K^-\pi^+$ decays the residual fraction of secondary decays is of the order of 3-5%.

asymmetries can occur. The raw asymmetries for the prompt, $A^{prt}_{raw}(f)$, and secondary decays, $A^{sec}_{raw}(f)$ can be expanded as usual as

$$A^{prt}_{raw}(f) = A^{prt}_{P}(D^*) + A_{CP}(f) + A^{prt}_{D}(\pi_s), \tag{8.1}$$
$$A^{sec}_{raw}(f) = A^{sec}_{P}(D^*) + A_{CP}(f) + A^{sec}_{D}(\pi_s), \tag{8.2}$$

where f stands for a generic final state. If the secondary fraction of secondary $D^0 \to K^0_S K\pi$ decays ($f^{K\pi}_{sec}$) and $D^0 \to K^0_S \pi\pi$ ($f^{\pi\pi}_{sec}$) decays are different, the result is a systematic shift Δ_{sec} on the ΔA_{CP} measurement that reads as [3]

$$\Delta_{sec} = \frac{f^{K\pi}_{sec} - f^{\pi\pi}_{sec}}{2}\left[A^{sec}_{raw}(K^0_S K\pi) + A^{sec}_{raw}(K^0_S\pi\pi) - A^{prt}_{raw}(K^0_S K\pi) - A^{prt}_{raw}(K^0_S\pi\pi)\right]. \tag{8.3}$$

Hence, in order to determine the bias given by the presence of secondary decays, it is necessary to measure their relative fractions in both decay modes. This can be done by performing a fit to the distribution of the D^0 candidates impact parameter χ^2 (or the D^0 impact parameter). This systematic uncertainty is assessed to be $\mathcal{O}(10^{-4})$ for two-body decay modes, as described in Ref.[3]. Hence, also for the present analysis it is expected to obtain a comparable uncertainty, lesser than the statistical uncertainty of the measurement described in this thesis.

Systematic uncertainty linked to the $A_D(\pi^+\pi^-)$ As explained in Sect. 2.3, this is the detection asymmetry of the $\pi\pi$ pair caused by the differences in the momentum dependent reconstruction efficiency of the charged pions, that in the case of a three-body decay, where the intermediate resonances arrange differently in the Dalitz Plot, they becomes relevant. These differences do not cancel out between the particle and antiparticle (D^0 and $\overline{D}^0$) causing a net detection asymmetry different from zero. The term $A_D(\pi^+\pi^-)$ is expected to be of the order of 0.1%, and it is measured with great accuracy using a sample of two-body $D^0 \to \pi^+\pi^-$ decays. The determination of this term is not subject of study of this thesis, and it will be assumed to be known with a very high precision. The methodology used to measure this quantity is currently developed within the LHCb-Pisa group in a parallel analysis effort.

Systematic uncertainty associated to the $A_D(K\pi)$ As explained in Sect. 2.3 the measurement of ΔA_{raw}, for RS and WS signal decays, is not sufficient to determine the physics observables of interest, the direct *CP*-violating asymmetries $A^{RS,WS}_{CP}(D^0 \to K^0_S K\pi)$. It is necessary to measure the detection asymmetry $A_D(K\pi) = A^{RS}_D(K\pi) = -A^{WS}_D(K\pi)$. This term can be determined using a similar ΔA_{raw} cancellation mechanism with the two-body $D^0 \to K^-\pi^+$ and $D^0 \to \pi^+\pi^-$, after an appropriate re-weighting of the kinematics of the $K\pi$ pair to that one of the $D^0 \to K^0_S K\pi$ decays. The size of this term is of about 1%, as it can be seen from Ref. [51], while its uncertainty will be dominated by the current measured value of $A_{CP}(D^0 \to \pi^+\pi^-)$, which is known to be $(0.07 \pm 0.14(\text{stat}) \pm 0.11(\text{syst}))\%$ from literature [27]. This uncertainty has the same size to the statistical uncertainty on ΔA^{RS}_{raw} and ΔA^{WS}_{raw}, which are 1.1×10^{-3} and 1.3×10^{-3} respectively, for the analysis of the full Dalitz plot[3]. It will be therefore the dominant systematic uncertainty for the moment. At the current level of precision this term can be assumed to be independent of the specific K^0_S proper decay-time bin, and, therefore, it will be applied just as a simple

[3]The LHCb Collaboration will soon publish the new measurement of $A_{CP}(D^0 \to \pi^+\pi^-)$ using the full Run 1 and Run 2 data sample, achieving an uncertainty of 0.7×10^{-3} [52].

translation of the measured ΔA_{raw}[4]. The variations of the kinematics of the $K\pi$ pair as a function of the different time bins can be considered as a second order effect. In this regard, Fig. 8.1 shows the distribution of the A_p and A_η in the different proper decay-time bins of the K^0_S. They are almost unchanged moving from the fist time bin (bin 0) of the Long sample to the last bin (bin 17) of the Downstream sample. This ensures that

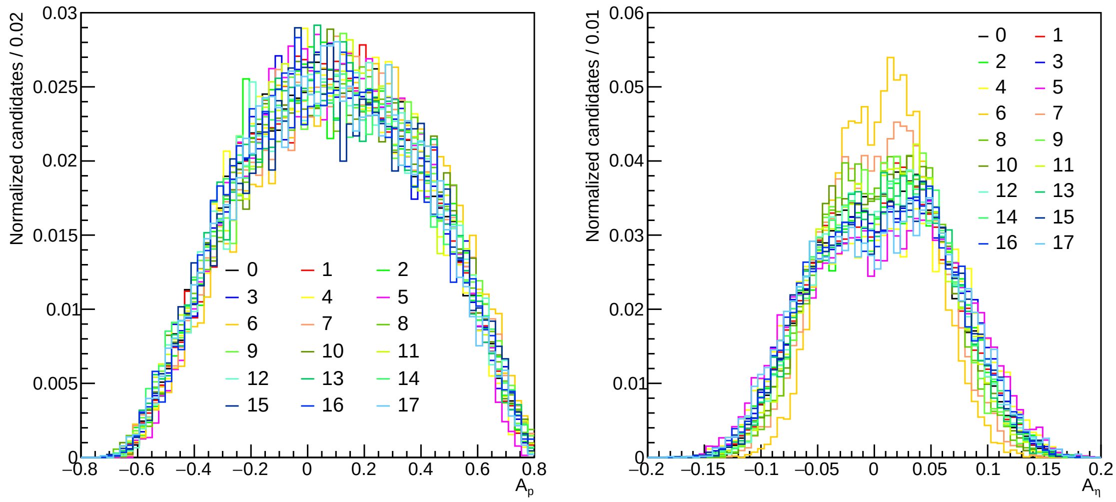

Figure 8.1: *Left: Distributions of A_p for each K^0_S proper decay-time bin. Left: Distributions of A_η for each K^0_S proper decay-time bin. The bins $[0-5]$ refer to Long K^0_S candidates, whereas the bins $[6-17]$ to the Downstream K^0_S candidates.*

any possible variation of the detection asymmetry $A_D(K\pi)$, as a function of the proper decay-time bin of the K^0_S, is a small correction, since the detection asymmetries are of the order of few per cents. This effect can be easily bounded and assigned as an additional systematic uncertainty. At some point, at very high precision, it will be necessary to extract a different $A_D(K\pi)$ term for each decay-time bin, and independently correct the measured $\Delta A_{raw}(t)$ asymmetry values before performing the linear (or constant) fit.

8.2 Results and conclusions

This thesis presents the most recent studies of the D^*-tagged $D^0 \to K^0_S K\pi$ decay channels, using the LHCb data sample collected during the LHC Run 2. The core of the work consists both in the design and implementation of a novel and robust analysis methodology that aims at measuring the time-integrated A_{CP}, both by integrating over the entire phase space (Dalitz plot) and in a restricted region, such as in the vicinity of the $K^*(892)^0 \to K\pi$ resonance. The driving idea of the method exploits the cancellation of all nuisance asymmetries by means a double ΔA_{CP} mechanism [3] between decay modes with very similar kinematics, and collected with very similar selections. The $D^0 \to K^0_S\pi^+\pi^-$ decay mode is dominated by Cabibbo-favoured processes, and because its similarities with the signal decays is used as an excellent calibration mode. The difference of the two raw asymmetries allows a reliable cancellation of the asymmetry in producing a charged D^* meson at the LHC, $A_P(D^*)$, and of the detector-induced charge asymmetry in reconstructing the "soft" pion to form a D^* meson candidate, $A_D(\pi_s)$.

[4]The sign of the correction is opposite for RS and WS decays, being $A_D^{RS}(K\pi) = -A_D^{WS}(K\pi)$.

However, residual detection asymmetries survive the cancellation mechanism, such as the detector-induced charge asymmetry in reconstructing the $K\pi$ pair, $A_D(K\pi)$, and the detection asymmetries due to the different probability of interaction with matter of neutral kaons, also including *CP*-violating effects present in the kaon system, $A_D(K^0)$. A precise value of the $A_D(K\pi)$ term can be measured using the two abundant two-body $D^0 \to K\pi$ and $D^0 \to \pi\pi$ decay modes, performing a similar difference between the raw asymmetries, while the $A_D(K^0)$ term requires an accurate time-dependent analysis as a function of the K^0_S proper decay time.

The full data sample collected by the LHCb experiment during the LHC Run 2 (2015-2018), corresponding to an integrated luminosity of about 5.6 fb^{-1}, is used in the analysis described in this thesis. Thanks to the optimized selection, the final sample is very pure and contains about 1,044,000 $D^0 \to K^0_S K^-\pi^+$ RS signal decays and about 718,000 $D^0 \to K^0_S K^+\pi^-$ WS signal decays over the whole phase space. This allows for the first time the measurement of the *CP*-violating asymmetries in these decays at a unprecedented level of 1×10^{-3}. In particular, the resulting statistical uncertainties, separately for the RS and WS samples, are

$$\Delta A_{CP}(D^0 \to K^0_S K^-\pi^+) = [xx \pm 1.1\text{ (stat)}] \times 10^{-3}, \tag{8.4}$$

$$\Delta A_{CP}(D^0 \to K^0_S K^+\pi^-) = [xx \pm 1.3\text{ (stat)}] \times 10^{-3}, \tag{8.5}$$

where the dominant systematic uncertainty, due to an external input [27], is equal to 1.8×10^{-3}. However, this uncertainty is expected to go below the level of 10^{-3} in the near future [52], because of the extension to the full Run 1 and Run 2 data sample of the measurement of $A_{CP}(D^0 \to \pi^+\pi^-)$.

By restricting the measurement in a region enriched with the intermediate $K^{*0} \to K^+\pi^-$ resonance, the final data sample contains about 22,000 $D^0 \to K^0_S K^-\pi^+$ RS signal decays and about 61,500 $D^0 \to K^0_S K^+\pi^-$ WS signal decays. The resulting statistical uncertainties in this restricted region of the phase space are

$$\Delta A_{CP}(D^0 \to K^0_S K^-\pi^+) = [xx \pm 7.3\text{ (stat)}] \times 10^{-3}, \tag{8.6}$$

$$\Delta A_{CP}(D^0 \to K^0_S K^+\pi^-) = [xx \pm 4.2\text{ (stat)}] \times 10^{-3}, \tag{8.7}$$

where the systematic uncertainties are expected of the same size of those of the analysis performed over the whole phase space.

The sensitivity achieved thanks to this thesis work is very intriguing. It will allow for the first time to experimentally reach the upper bound of the theoretical predictions of the *CP* violation for these decay modes. In particular, the difference between the measurement over the full phase space and the same measurement performed in the vicinity of the intermediate $K^{*0} \to K^+\pi^-$ resonance, is a powerful probe to look for hints of new sources of *CP* violation. Indeed, SM predictions for the *CP*-violating asymmetries in the $D^0 \to K^0_S K^{*0}$ and $D^0 \to K^0_S \overline{K}^{*0}$ decays are very small $\leq 3 \times 10^{-3}$ [9]. In conclusion, the study reported in this thesis returned to be very robust, since a double ΔA_{CP} difference mechanism is exploited to search for possible hints of *CP*-violating asymmetries in the $D^0 \to K^0_S K^\pm\pi^\mp$ decays. It paves the way for a measurement with the already available Run 2 data sample at the per mil level, and for future measurements, at much higher statistics, in the Upgraded LHCb era.

A Selection of untagged $D^0 \to K_S^0 K\pi$ decays

A.1 Selection of the *untagged* candidates

The D^0 candidates, where the flavour at production cannot be identified, are called *untagged*. As explained in the Sect 5.4, LHCb does not have a dedicated trigger line for the untagged $D^0 \to K_S^0 K^{\pm}\pi^{\mp}$ decays. However, it is possible to overcome this problem, selecting a small sample of such decays using the combination of a real reconstructed D^0 meson with a random pion. The D^0 candidates populating Δm mass side-band at higher mass values are mainly candidates of this type and they can be considered as untagged decays. Therefore, the region $\Delta m = [149, 160]$ MeV$/c^2$ is selected, it is shown in Fig. A.1 between the two blue dashed lines. The same optimization process described in Chapt. 5, is then applied.

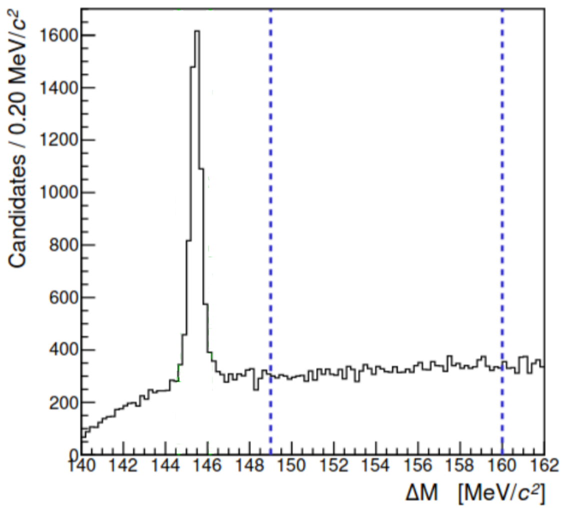

Figure A.1: *Invariant Δm distribution after trigger requirements and baseline selection. The blue dashed lines enclose the region that identifies the untagged candidates.*

A.2 The optimization strategy

The optimization strategy used with the *untagged* candidates is analogous to that used with the *tagged* ones. Hence, the optimization process aims at enhancing the value of the figure of merit $\mathcal{R}$, defined as in Sect. 5.4

$$\mathcal{R} = \frac{S}{\sqrt{S+B}}. \tag{A.1}$$

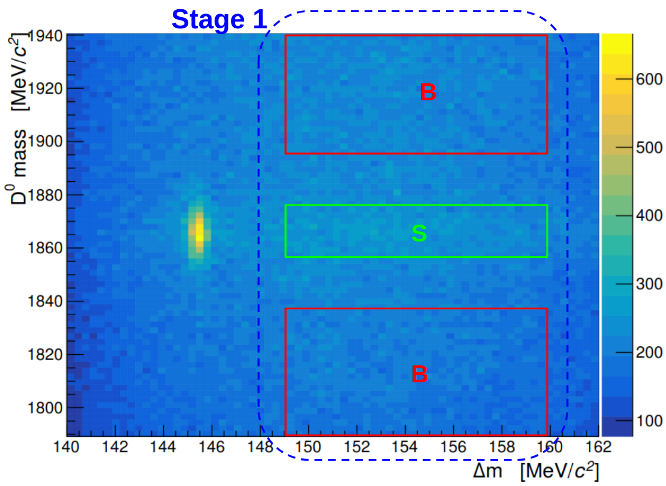

Figure A.2: *2D histogram of invariant $m(D^0)$ vs Δm distributions. The red and green regions qualitatively represent the background and the signal respectively, where the counting of S and B is performed.*

Figure A.2 shows the 2D histogram where the invariant $m(D^0)$ mass is reported on the y axis, while the invariant Δm mass is reported on the x axis. The S and B regions are located in the sideband of the Δm distribution, in three different ranges of the D^0 mass, as shown in Fig. A.3. Each interval is precisely identified:

- **Bl**, the blue shaded region on the left of the peak is the left background region: $m(D^0) \in [1790, 1810]$ MeV$/c^2$,
- **Br**, the blue shaded region on the right of the peak is the right background region: $m(D^0) \in [1920, 1940]$ MeV$/c^2$,
- **SB**, the green shaded region is the signal region: $m(D^0) \in [1855, 1875]$ MeV$/c^2$.

The same figure (Fig. A.3) also shows the starting $m(D^0)$ distribution, where the trigger decisions, the baseline cuts and the Δm requirements are applied. In order to quantify the purity of the sample before the optimization process, we calculate the value of the figure of merit $S/\sqrt{S+B}$ under the signal peak. The value returns to be equal to 53.57.

As explained in Sect. 5.4, using the above mentioned regions, three histograms (h_{Bl}, h_{Br}, h_{SB}) are built with the events belonging to the respective $m(D^0)$ regions. As long as the three regions have the same length (20 MeV$/c^2$) and the background is assumed to be linear, the background and signal histograms (h_B and h_S, respectively) are built using the following relations:

$$h_B = \frac{h_{Br} + h_{Bl}}{2}, \quad h_S = h_{BS} - h_B.$$

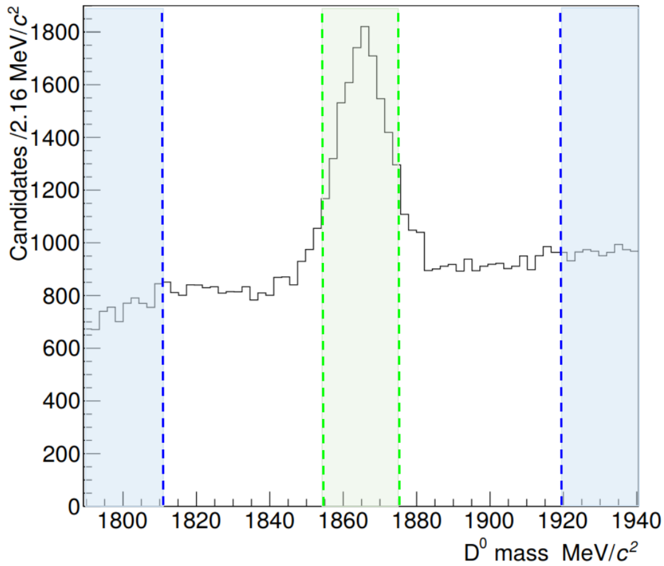

Figure A.3: *Invariant $m(D^0)$ distribution after the trigger requirements, baseline cuts and the cut $\Delta m \in [149, 160]$ MeV/c^2. The blue shaded regions are the background regions respectively on the left* **Bl** *and on the right* **Br** *of the peak. The green shaded region is the* **SB** *region.*

The cumulant distribution for both of them is built, in order to quantify the number of signal and background candidates passing the cut of interest. In this way each bin univocally corresponds to a precise combination of cuts, as described in Sect 5.4. At this point, it is possible to compute the value of the figure of merit $\mathcal{R}$ for each bin and find the combination of cuts that gives the highest value of $\mathcal{R}$. It is computed using Eq. A.1 for each bin, where S will be replaced by the bins content of the h_S histogram, while B will be replaced by the bins content of the h_B histogram.

A.3 The optimization process

The optimization process uses the sample, shown in Fig. A.3, selected by applying the following requirements:

- trigger decision,
- baseline selection,
- $\Delta m \in [149, 160]$ MeV/c^2.

The number of available variables is higher than 8, the maximum number of input variables that the optimization algorithm can simultaneously process. Therefore, the whole multi-dimensional space is factorized in sub-spaces, that can be considered independent with a good level of approximation. The optimization is performed independently on each sub-space, and a posteriori the accuracy of such an approximation is checked. Hence, the optimization process is divided in the following steps:

i. scan of the K^0_S and K^0_S daughters space - (*6 dimensions*),

ii. scan of the kinematic variables of the D^0 daughters K and π - (*7 dimensions*),

iii. scan of the quality track variables of D^0 daughters K and π - (*4 dimensions*).

iv. scan of the D^0 variables - (*5 dimensions*).

The data sample used for the untagged optimization is the same used for the tagged otimization, *i.e.* 2/5 of the 2016 magnet Down sample. The results of these individual steps are reported in Tab. A.1, where the total range indicates the interval that includes all the domain of the variable, while the final range indicates the interval used by the optimization algorithm to refine the position of the optimal configuration. The algorithm is able to scan 10 bins for each observable at a time.

Table A.1: *List of input variables used in the untagged selection optimization process. *Trigger Cut.**Baseline cut.*

Candidate	Variable	Range (n.bin 10) *Total*	*Final*	Result	Units
K_S	p	$[3, 180]$	$[5, 100]$	-	GeV/c
	p_T	$[0, 8000]$	$[400, 1000]$	> 640	MeV/c^2
	Vertex fit χ^2/ndf	$[0, 30^*]$	$[0, 30^*]$	-	-
$h^\pm$ of K_S	Track χ^2/ndf	$[0, 3^*]$	$[0, 3^*]$ $\pi^\pm$	-	-
		$[0, 3^*]$	$[0, 3^*]$ $\pi^\pm$	-	-
	$\cos\theta_{\pi\pi}$	$[0.97, 1]$	$[0.97, 1]$	> 0.982	-
$K\pi$ of D^0	p	$[5^*, 140]$	$[5^*, 100]$ $\pi^\pm$	-	GeV/c
		$[5^*, 140]$	$[5^*, 100]$ $K^\pm$	-	GeV/c
	p_T	$[800^*, 9000]$	$[800^*, 4000]$ $\pi^\pm$	-	MeV/c
		$[800^*, 9000]$	$[800^*, 4000]$ $K^\pm$	-	MeV/c
	χ^2_{IP}	$[4^*, 10000]$	$[4^*, 500]$ $\pi^\pm$	-	-
		$[4^*, 10000]$	$[4^*, 500]$ $K^\pm$	-	-
	DLL_{KPi}	$[-100, 5^*]$	$[-15, 5^*]$ $\pi^\pm$	-	-
		$[5^*, 100]$	$[5^*, 20]$ $K^\pm$	-	-
	$\cos\theta_{K\pi}$	$[0.98, 1]$	$[0.99, 1]$	-	-
	Track χ^2/ndf	$[0, 3^*]$	$[0, 3^*]$ $\pi^\pm$	-	-
		$[0, 3^*]$	$[0, 3^*]$ $K^\pm$	< 2.7	-
	$\mathcal{P}_{GHOST}$	$[0, 0.4^*]$	$[0, 0.4^*]$ $\pi^\pm$	-	-
		$[0, 0.4^*]$	$[0, 0.4^*]$ $K^\pm$	-	-
D^0	p	$[15, 350]$	$[20, 200]$	> 20	GeV/c
	p_T	$[1.8^*, 16]$	$[1.8^*, 3]$	> 2.52	GeV/c
	Vertex fit χ^2/ndf	$[0, 20^*]$	$[0, 20^*]$	< 4	-
	χ^2_{FD}	$[0, 400]$	$[0, 100]$	-	-
	FD	$[0, 1000]$	$[0, 200]$	-	-
	χ^2_{IP}	-	$[0, 9^{**}]$	< 6.3	-

The comparison between the $m(D^0)$ distribution before and after the optimized selection is shown in Fig. A.4. The light blue histogram is the m(D^0) distribution before the application of the optimized selection (Fig. A.3), whereas the blue one shows the result given by the selection returned by the optimization process. It is possible to notice that the background has been halved, moreover the value of $\mathcal{R}$ moves from 53.57 to 57.96. The optimized selection significantly reduces the background keeping the signal efficiency very high.

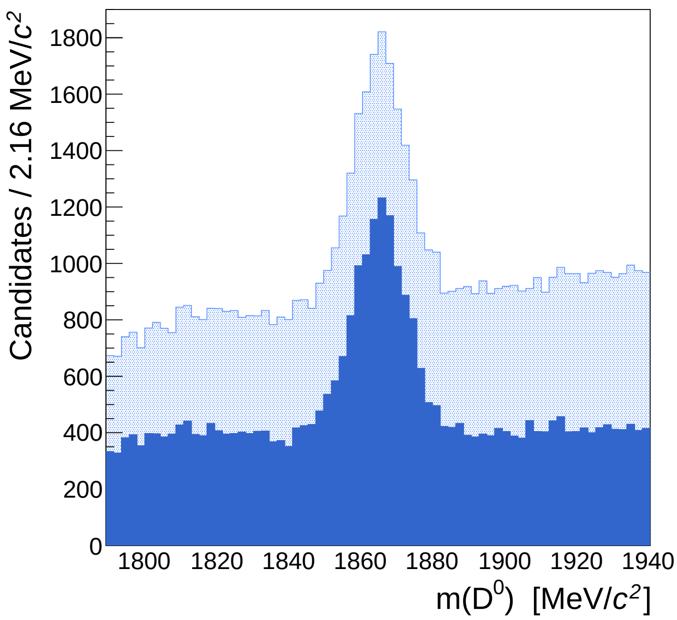

Figure A.4: *Comparison of the invariant $m(D^0)$ distributions. The light blue distribution is the distribution before the to perform the optimization process, whereas the blue one is the distribution where the optimized selection is applied.*

This optimization process assumes that whole space can be factorized in small independent sub-spaces. In order to check the accuracy of such an approximation only the sensible variables of the optimization algorithm among the several steps are used as new inputs, and simultaneously re-optimized to account for possible correlations. If the factorization is accurate, *i.e.* the sub-spaces are independent with a good level of accuracy, a similar output is expected. The results of this final check are reported in Tab. A.2. They are very similar to the previous ones, indeed the value of the figure of merit, $\mathcal{R} = 58.54$, is near to that previously obtained 57.96.

Table A.2: *Check of the factorization of the variables space, the outputs shown in Tab. A.1 are used as inputs of the optimization algorithm.*

Candidate	Variable	Range (n.bin 10) *Total*	*Final*	Result	Units
K_S	p_T	$[0, 8000]$	$[400, 1000]$	> 500	MeV/c^2
$h^{\pm}$ of K_S	$\cos\theta_{\pi\pi}$	$[0.97, 1]$	$[0.97, 1]$	> 0.982	-
$K\pi$ of D^0	Track χ^2/ndf	$[0, 3^*]$	$[0, 3^*]$ $K^{\pm}$	< 2.9	-
D^0	p	$[15, 350]$	$[20, 200]$	> 20	GeV/c
	p_T	$[1.8^*, 16]$	$[1.8^*, 3]$	> 2.46	GeV/c
	Vertex fit χ^2/ndf	$[0, 20^*]$	$[0, 20*]$	< 4.6	-
	χ^2_{IP}	-	$[0, 9^{**}]$	< 6.4	-

B Yield Fits

This appendix shows the fits performed to the Δm distributions in order to compute the signal yields that are reported in Sect. 5.7, Tab. 5.7. The fit are performed separately for all the available data samples (24 fits), for the total amount of data of each year (6 fits) and for each sample integrating over the year of data taking (10 fits). The resulting yields are reported in Tab. B.1 and Tab. B.2, instead the distribution of χ^2 and p-value of the fits are shown in Fig. B.1 on the left and on the right hand side, respectively.

Table B.1: *Signal yields of the WS samples.*

year	K_S track		Magnet		TOT
	Long	Downstream	Up	Down	**WS**
2016	80k	128k	95k	108k	204k
2017	88k	162k	119k	130k	245k
2018	94k	177k	141k	134k	266k
TOT	260k	460k	352k	363k	**718k**

Table B.2: *Signal yields of the RS samples.*

year	K_S track		Magnet		TOT
	Long	Downstream	Up	Down	**RS**
2016	128k	190k	157k	153k	302k
2017	123k	230k	174k	180k	356k
2018	139k	250k	200k	188k	389k
TOT	387k	673k	517k	527k	**1M 44k**

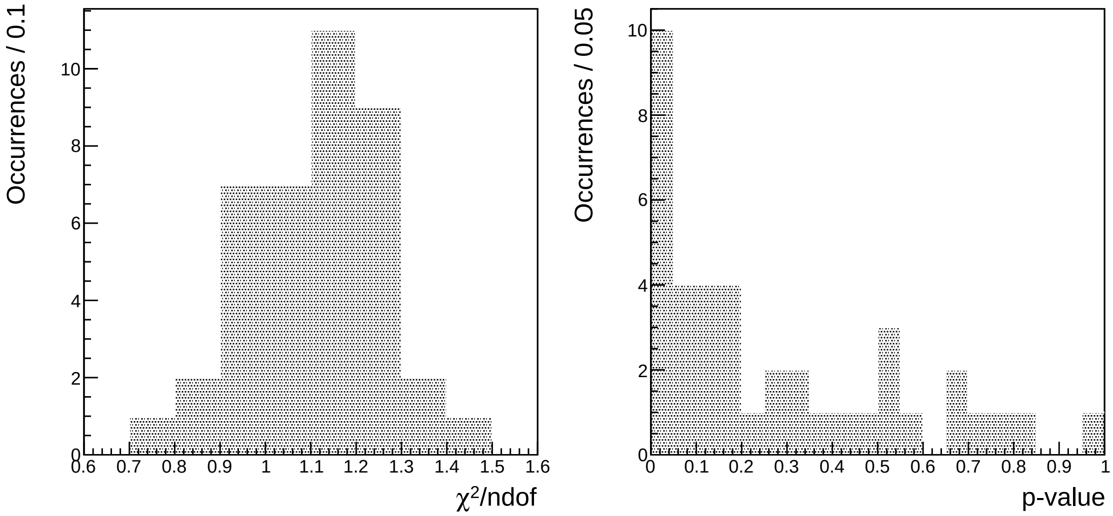

Figure B.1: *Left: distribution of the χ^2 returned by the fits. Right: distribution of the p-value returned by the fits.*

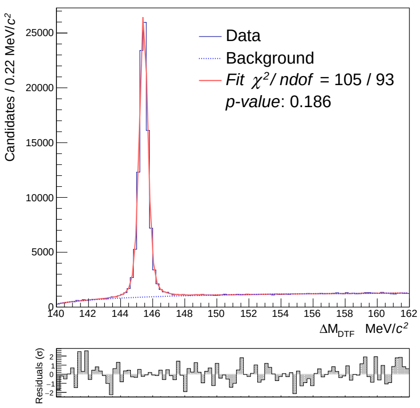

(a) WS, 2016, Up polarity

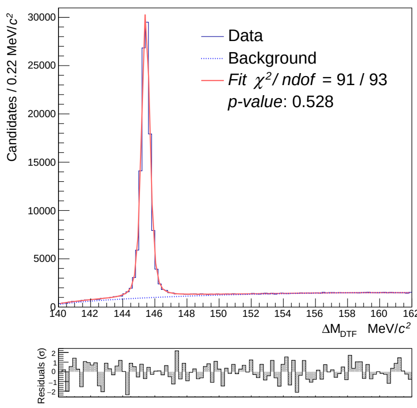

(b) WS, 2016, Down polarity

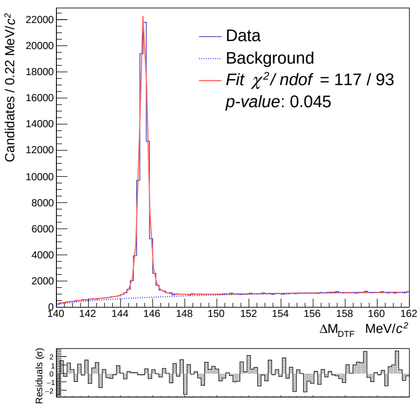

(c) WS, 2016, Long K_S tracks

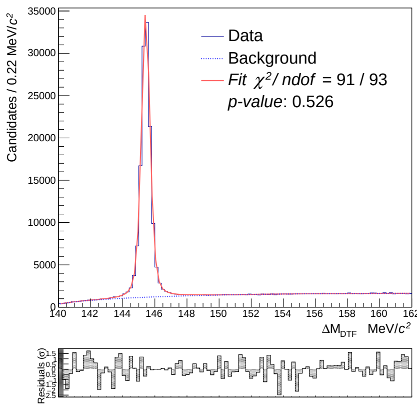

(d) WS, 2016, Downstream K_S tracks

Figure B.2

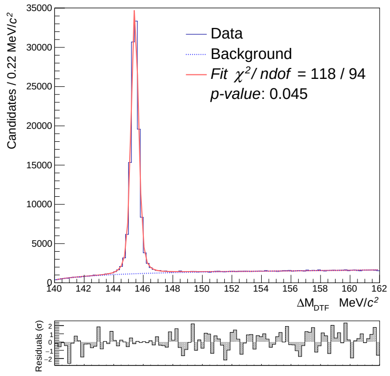

(a) WS, 2017, Up polarity

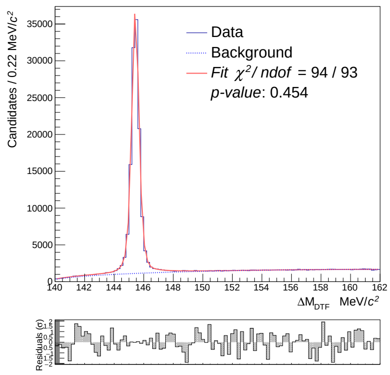

(b) WS, 2017, Down polarity

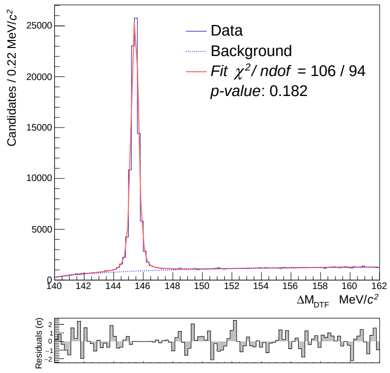

(c) WS, 2017, Long K_S tracks

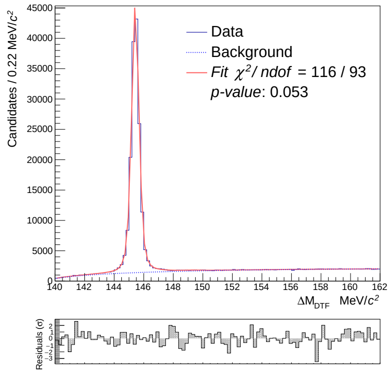

(d) WS, 2017, Downstream K_S tracks

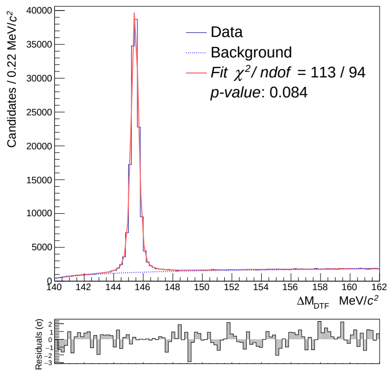

(e) WS, 2018, Up polarity

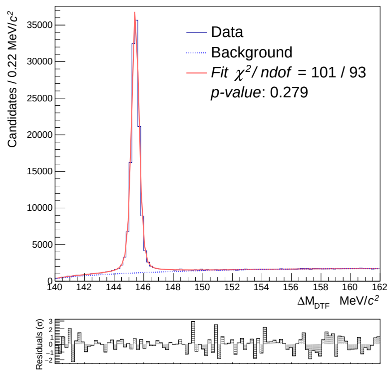

(f) WS, 2018, Down polarity

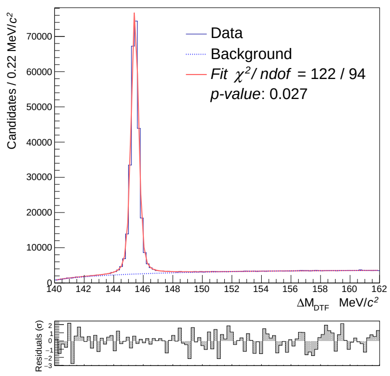

(g) WS, 2018, Long K_S tracks

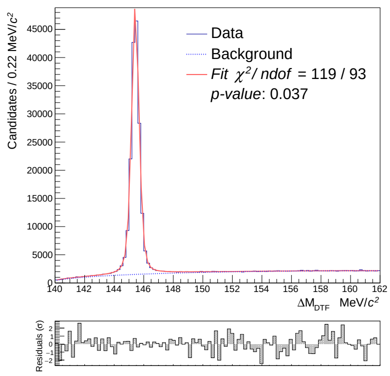

(h) WS, 2018, Downstream K_S tracks

Figure B.3

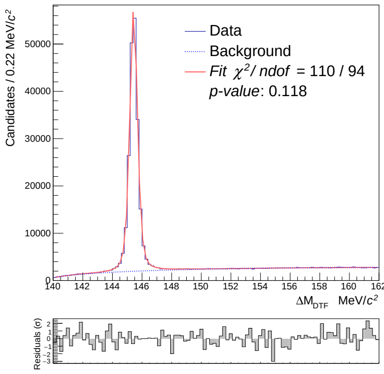

(a) WS, Total 2016

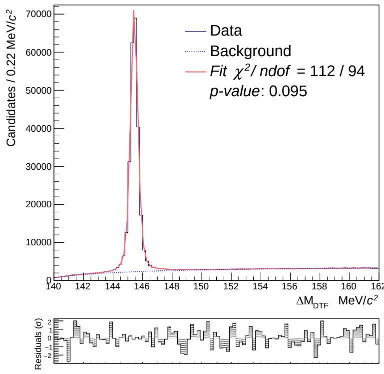

(b) WS, Total 2017

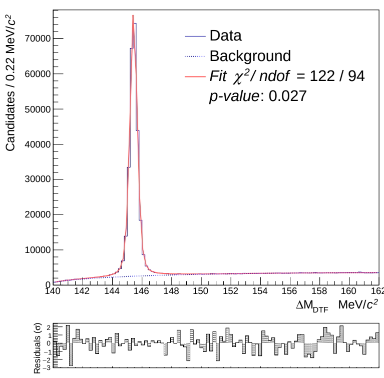

(c) WS, Total 2018

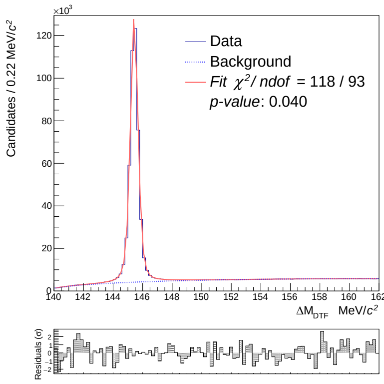

(d) WS, Total Downstream K_S tracks

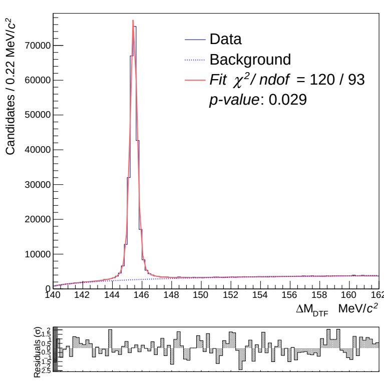

(e) WS, Total Long K_S tracks

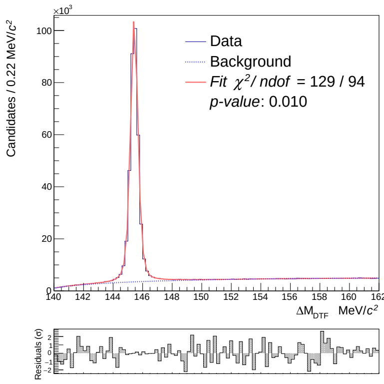

(f) WS, Total Down polarity

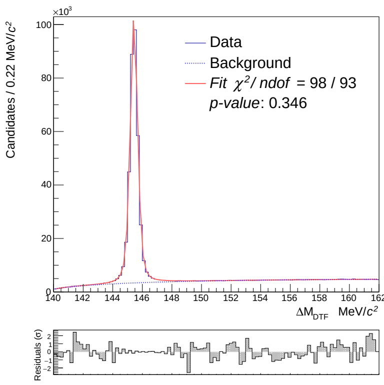

(g) WS, Total Up polarity

Figure B.4

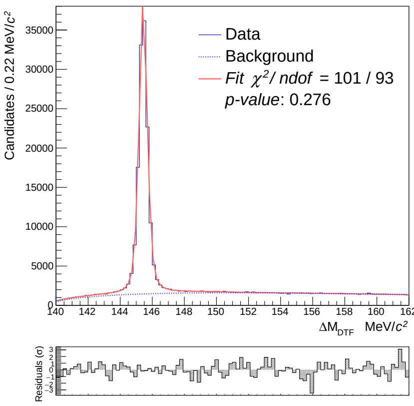

(a) RS, 2016, Up polarity

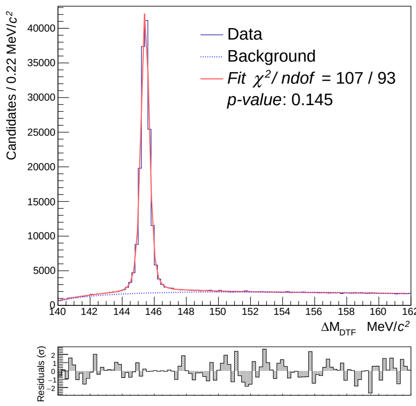

(b) RS, 2016, Down polarity

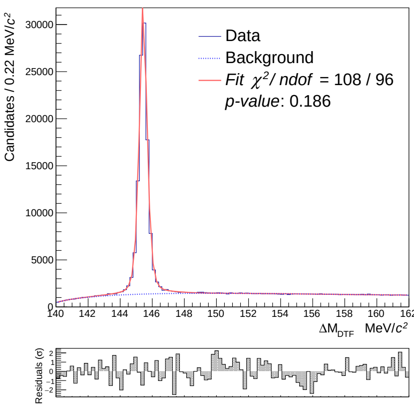

(c) RS, 2016, Long K_S tracks

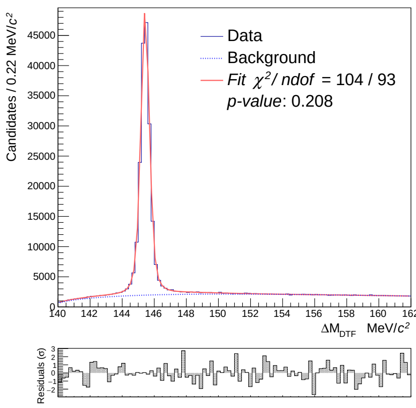

(d) RS, 2016, Downstream K_S tracks

Figure B.5

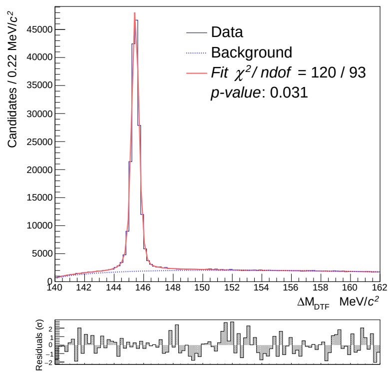

(a) RS, 2017, Up polarity

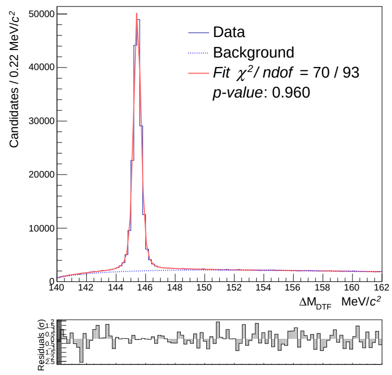

(b) RS, 2017, Down polarity

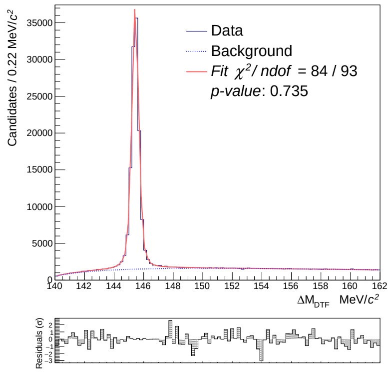

(c) RS, 2017, Long K_S tracks

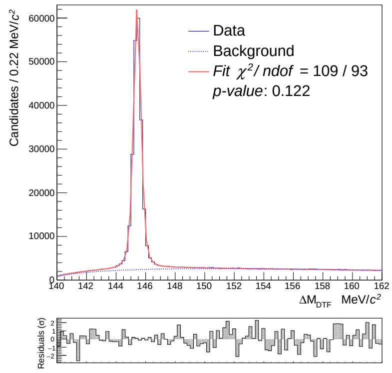

(d) RS, 2017, Downstream K_S tracks

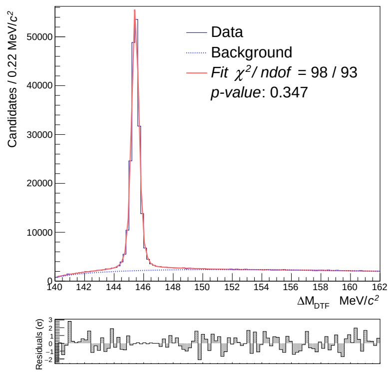

(e) RS, 2018, Up polarity

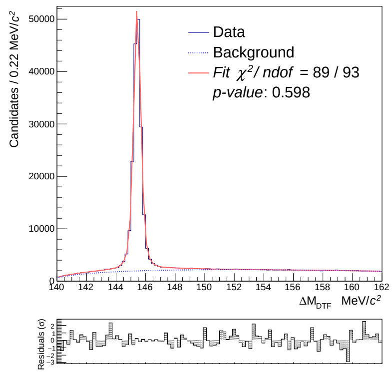

(f) RS, 2018, Down polarity

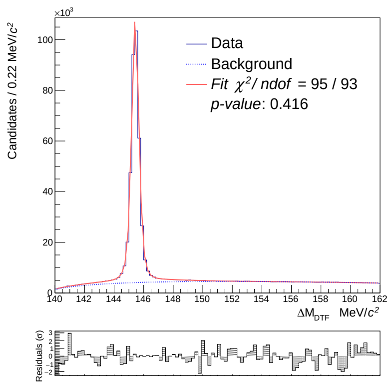

(g) RS, 2018, Long K_S tracks

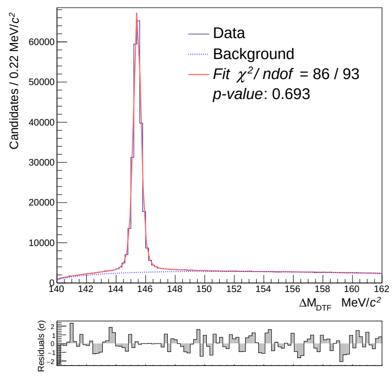

(h) RS, 2018, Downstream K_S tracks

Figure B.6

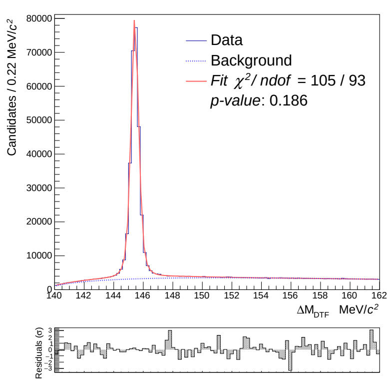

(a) RS, Total 2016

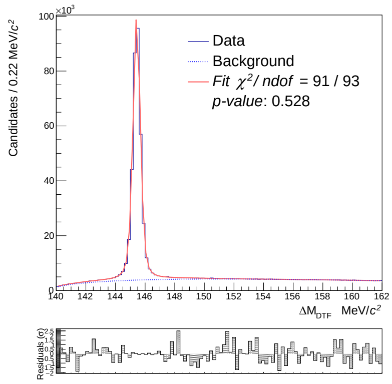

(b) RS, Total 2017

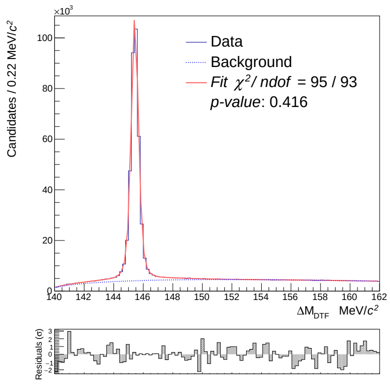

(c) RS, Total 2018

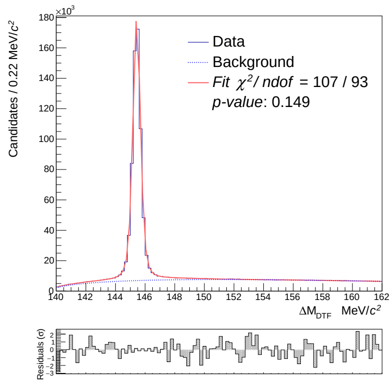

(d) RS, Total Downstream K_S tracks

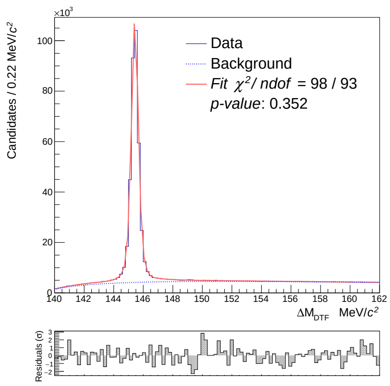

(e) RS, Total Long K_S tracks

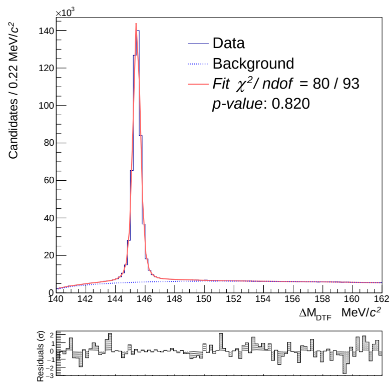

(f) RS, Total Down polarity

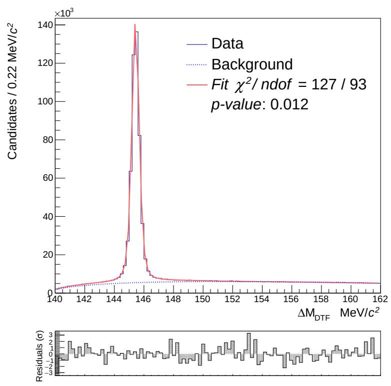

(g) RS, Total Up polarity

Figure B.7

C Additional material

C.1 Kinematic variables after re-weighting procedure

This section illustrates the comparison between the kinematic distributions of the signal and controle modes in each bin of K_S^0 proper decay time, after the re-weighting procedure described in Sect. 6.4. The distribution shown in this Appendix correspond to the whole Long, WS sample.

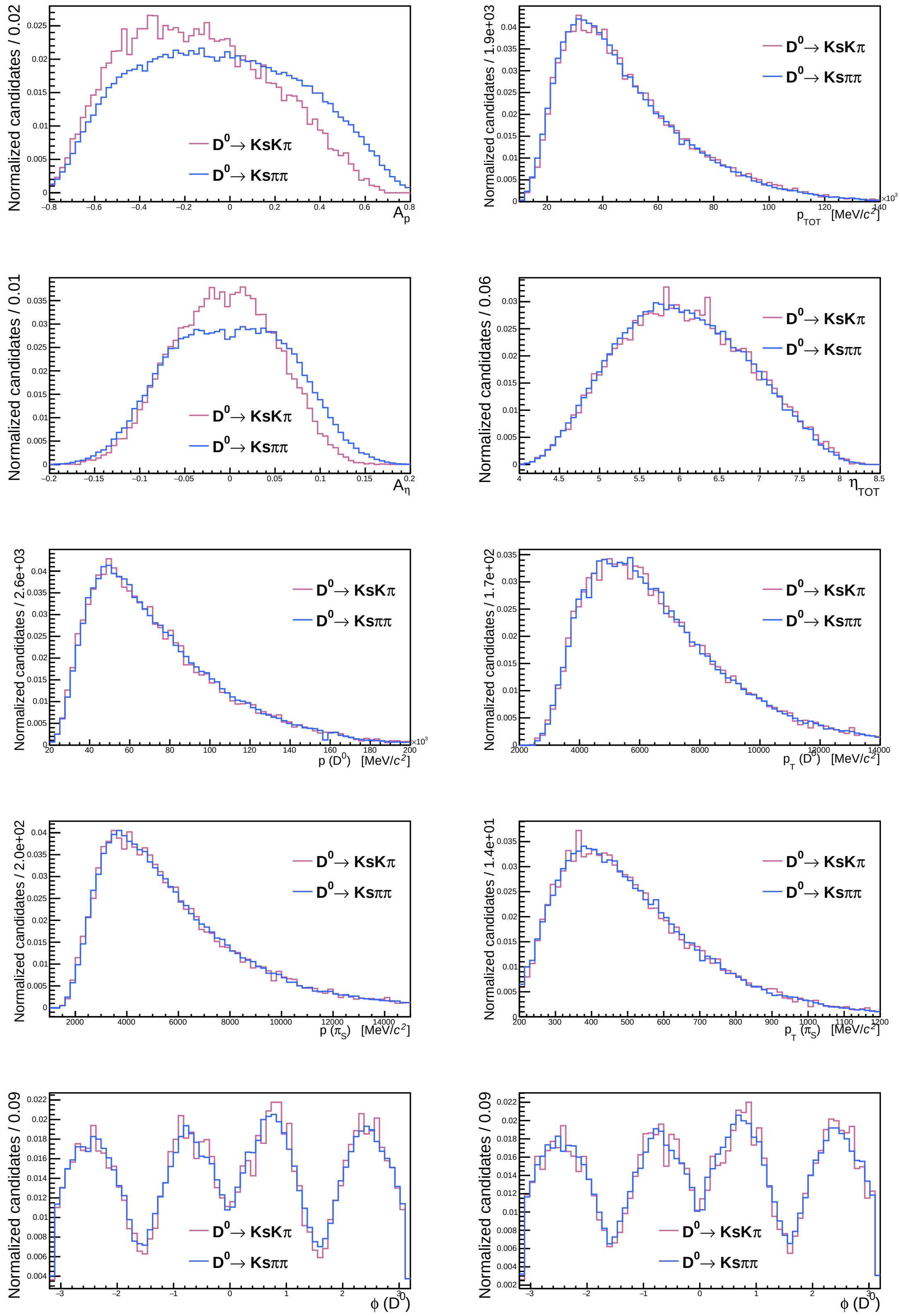

Figure C.1: *Comparison between the normalized kinematic distributions of the signal and control modes. K^0_S decay-time bin 0. WS, Long sub-sample.*

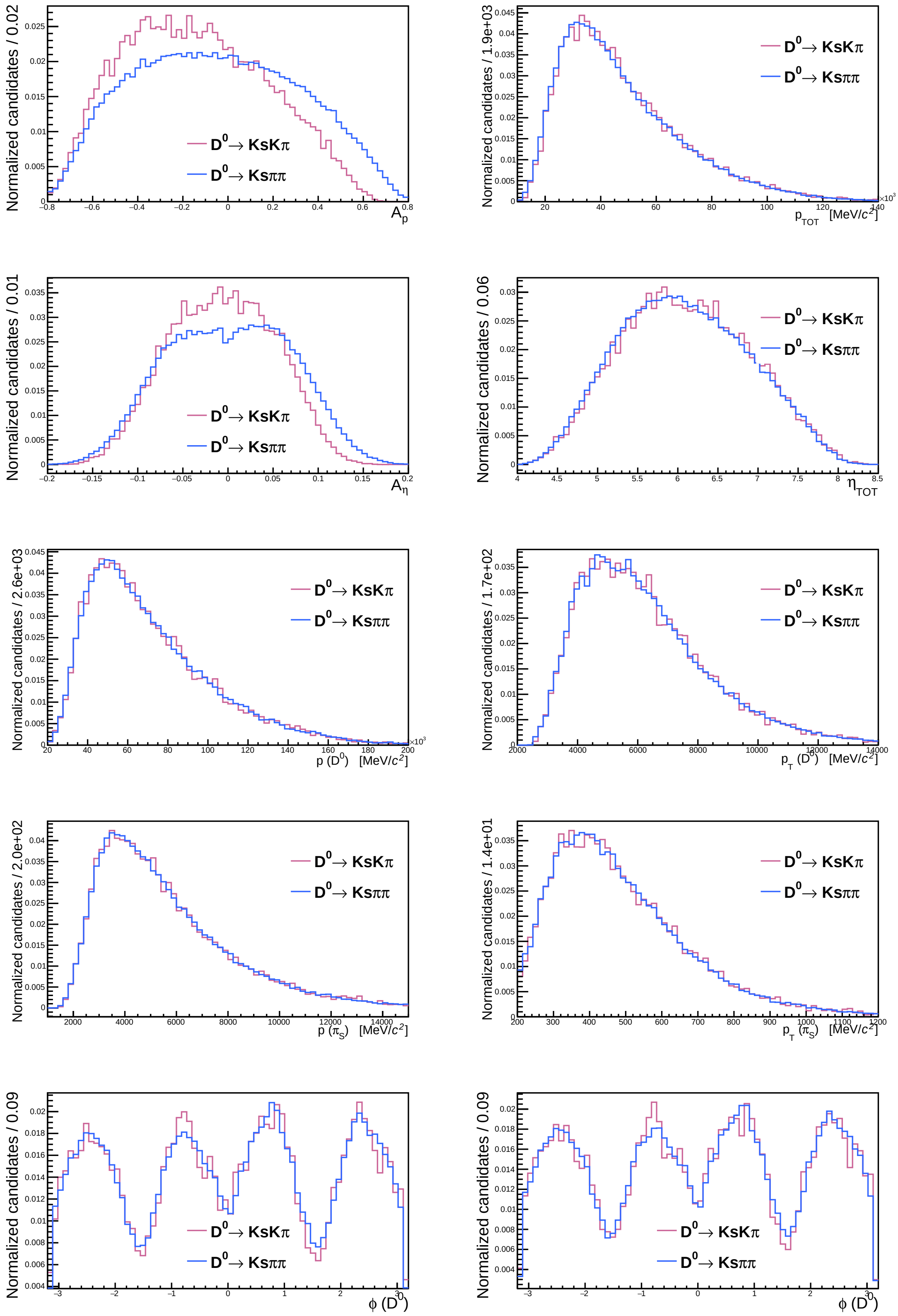

Figure C.2: *Comparison between the normalized kinematic distributions of the signal and control modes. K^0_S decay-time bin 1. WS, Long sub-sample.*

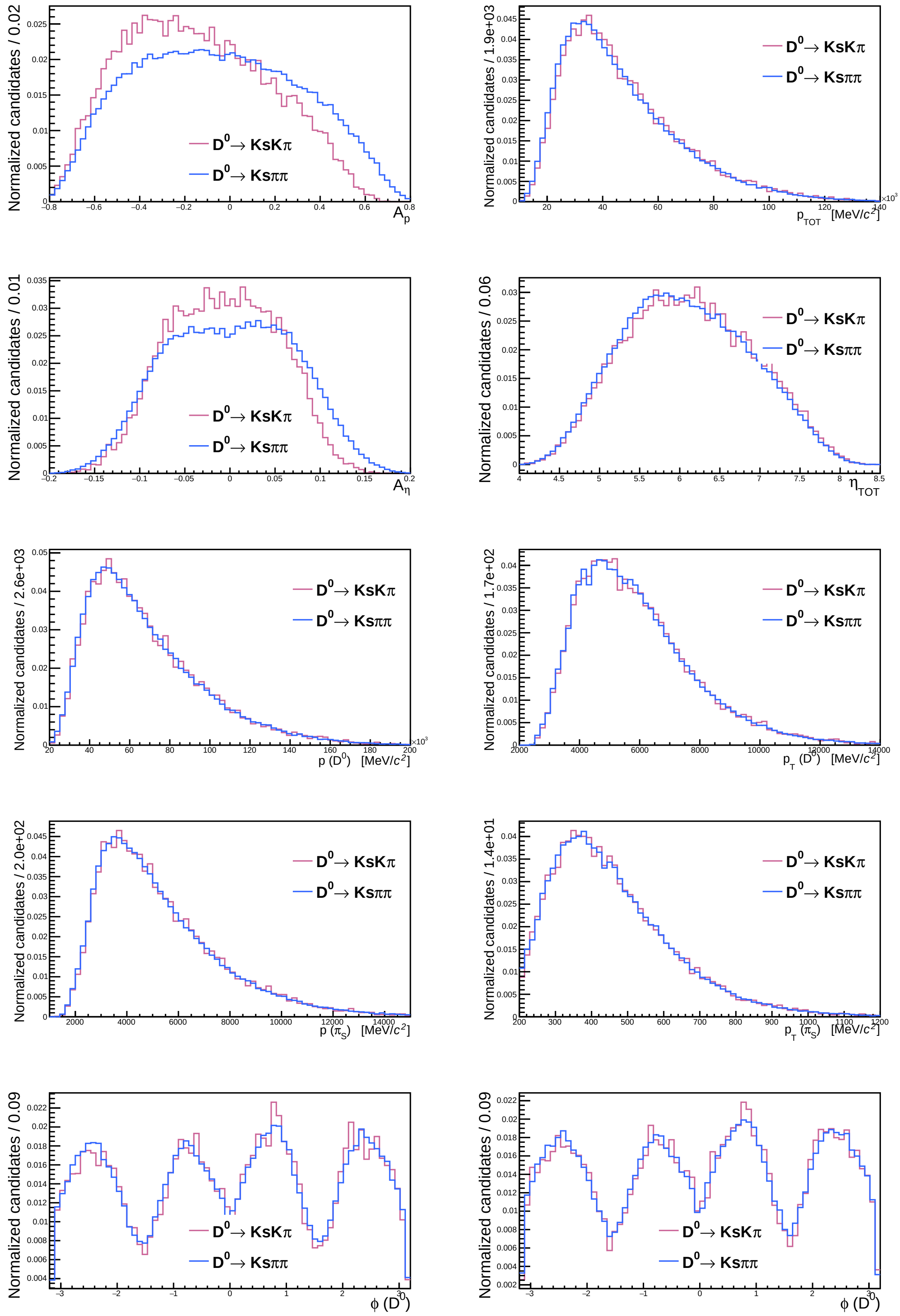

Figure C.3: *Comparison between the normalized kinematic distributions of the signal and control modes. K^0_S decay-time bin 2. WS, Long sub-sample.*

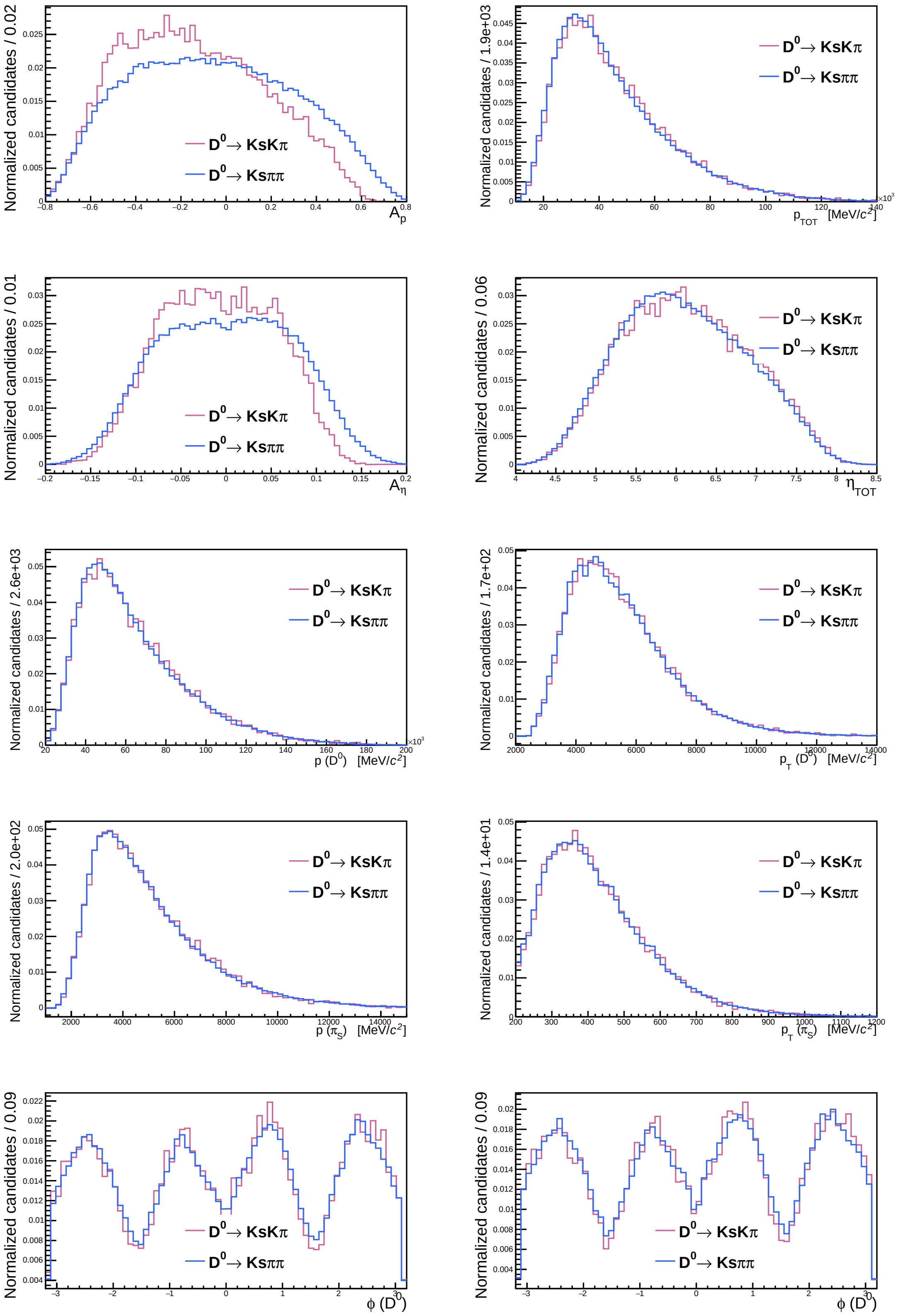

Figure C.4: *Comparison between the normalized kinematic distributions of the signal and control modes. K_S^0 decay-time bin 3. WS, Long sub-sample.*

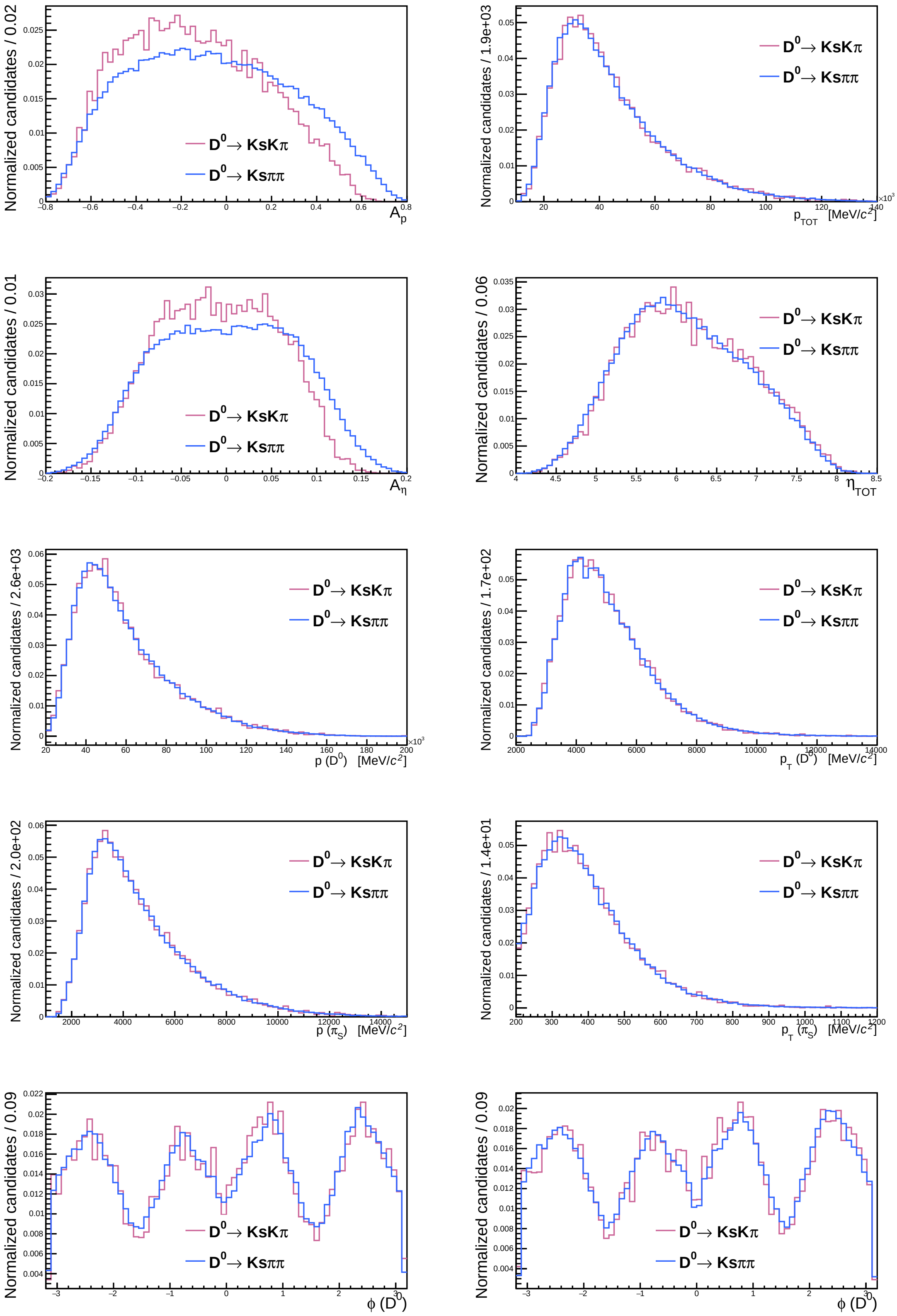

Figure C.5: *Comparison between the normalized kinematic distributions of the signal and control modes. K_S^0 decay-time bin 4. WS, Long sub-sample.*

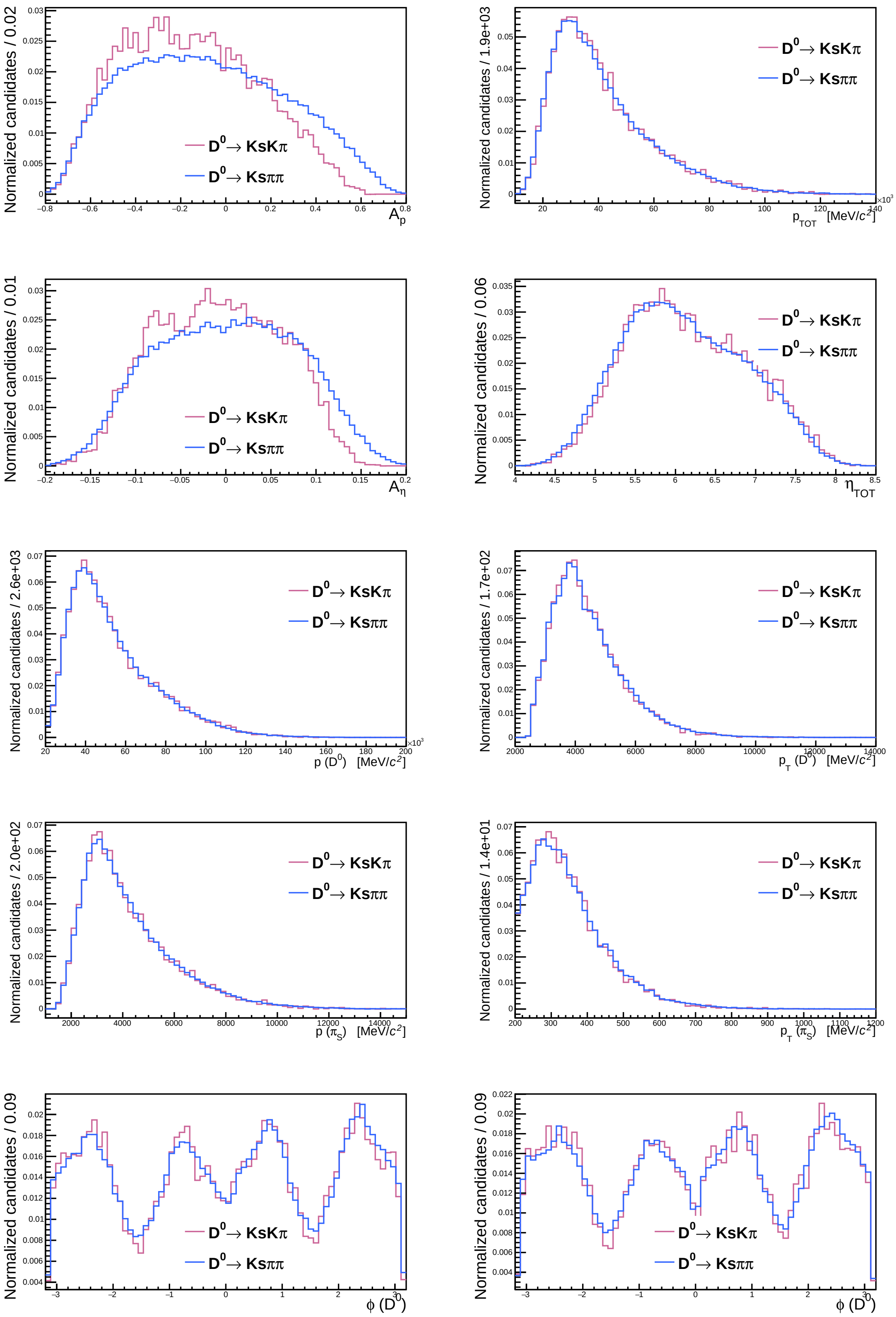

Figure C.6: *Comparison between the normalized kinematic distributions of the signal and control modes. K^0_S decay-time bin 5. WS, Long sub-sample.*

C.2 Time dependent raw *CP* asymmetry

This section shows the blinded measurement of the $A^{RS(WS)}_{raw}(t)$ compared with the $A^{\pi\pi}_{raw}(t)$ for each data taking year.

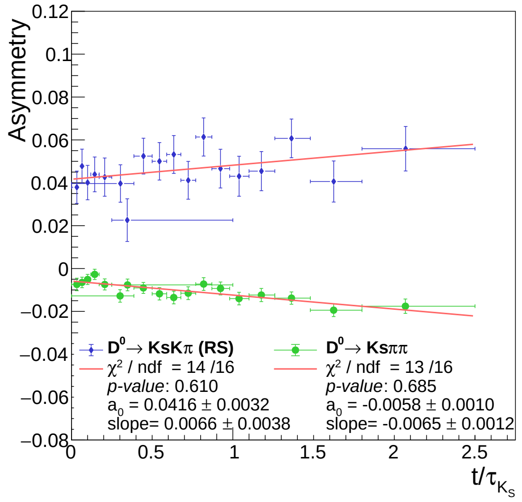

(a) RS sample, 2016

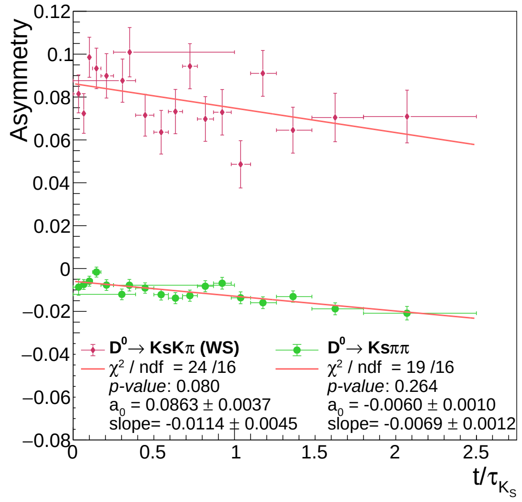

(b) WS sample, 2016

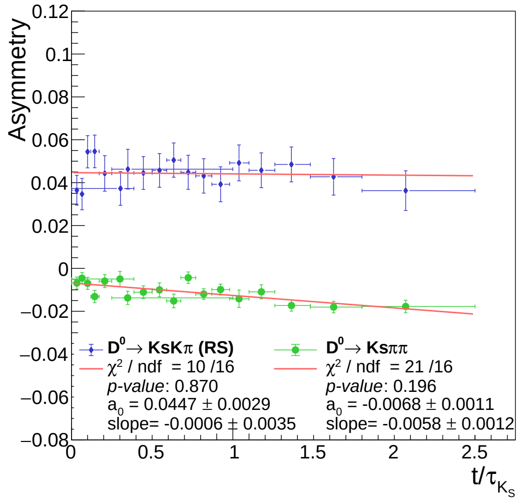

(c) RS sample, 2017

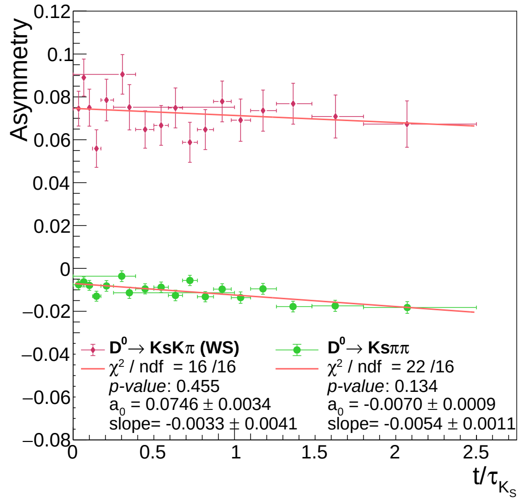

(d) WS sample, 2017

Figure C.7

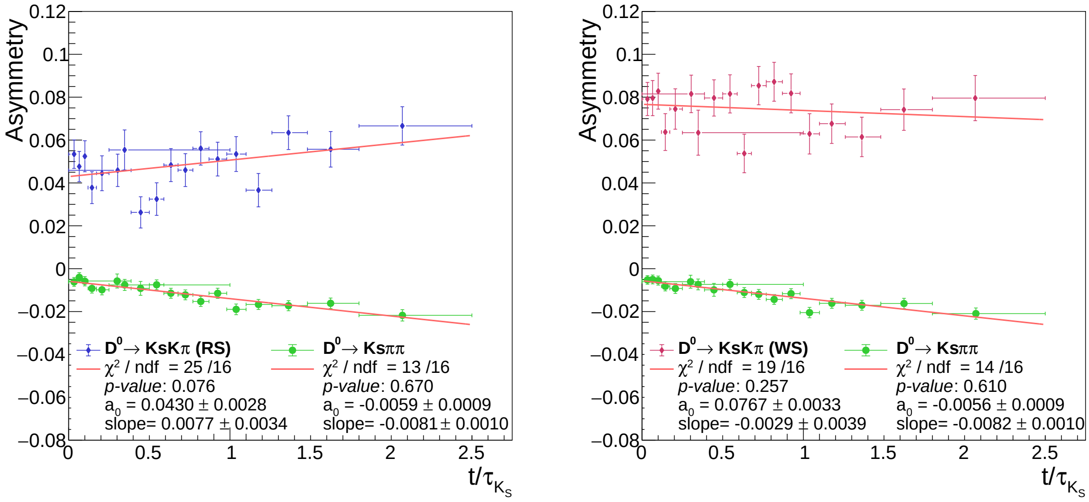

(a) RS sample, 2018 **(b)** WS sample, 2018

Figure C.8

C.3 $\Delta A^{RS(WS)}_{raw}(t)$ data

This section illustrates the measurement of the blinded $\Delta A^{RS(WS)}_{raw}(t)$ for each data taking year.

The RS data fitted to a constant function are the result of the difference of the $A^{RS}_{raw}(t)$ to the reversed $A^{\pi\pi}_{raw}(t)$.

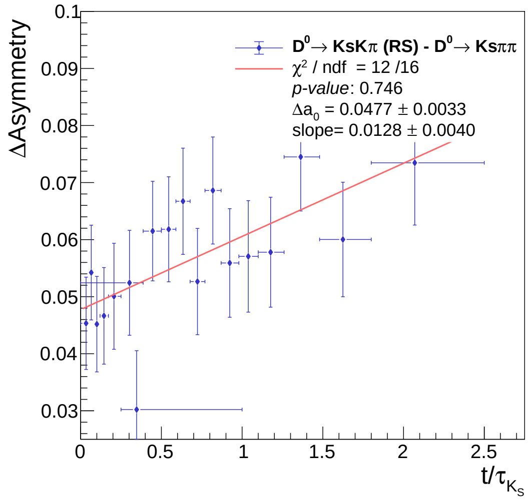

(a) RS sample, 2016

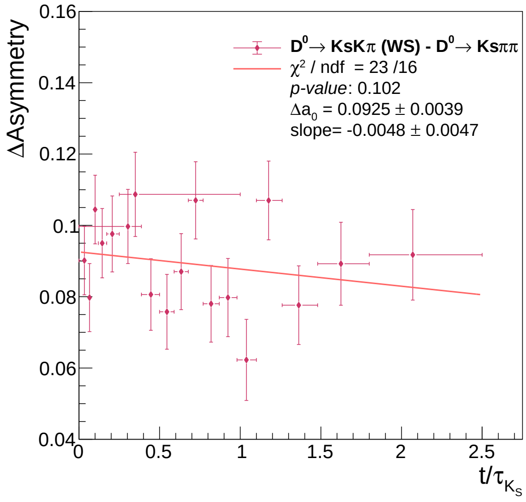

(b) WS sample, 2016

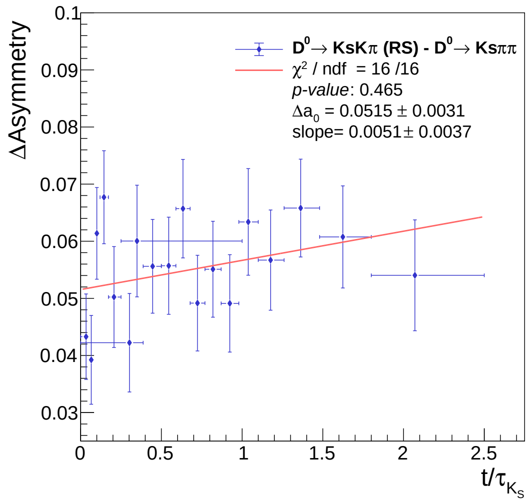

(c) RS sample, 2017

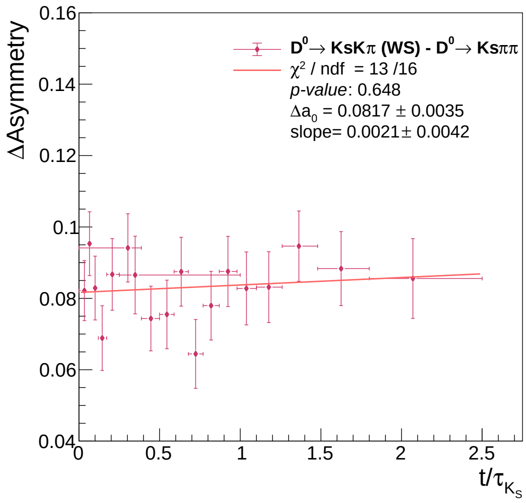

(d) WS sample, 2017

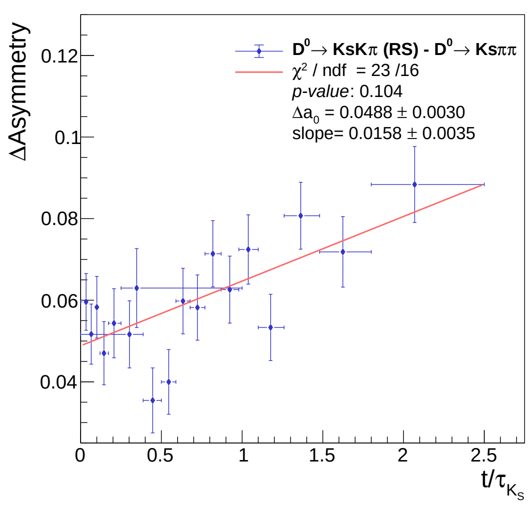

(e) RS sample, 2018

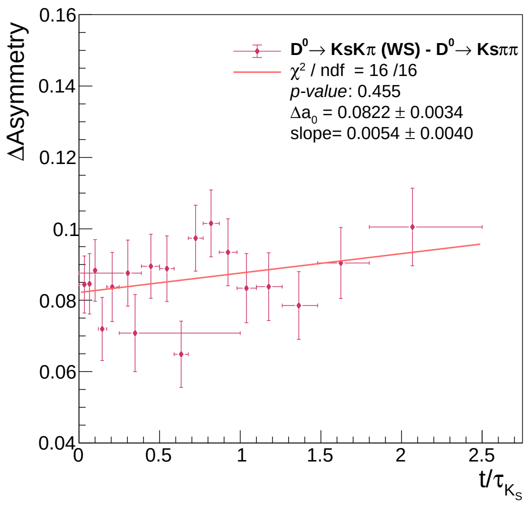

(f) WS sample, 2018

Figure C.9

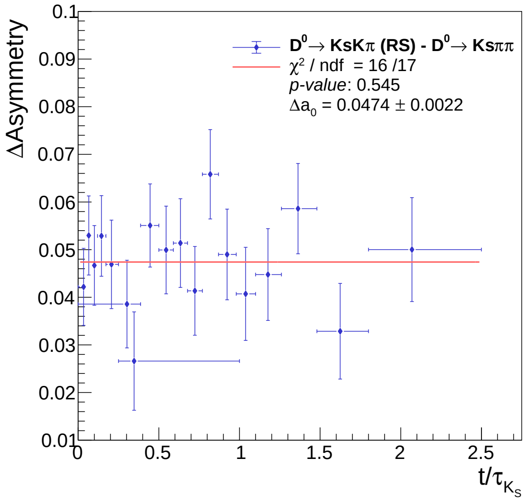

(a) RS sample, 2016. Reversing of the $A^{\pi\pi}_{raw}$ data.

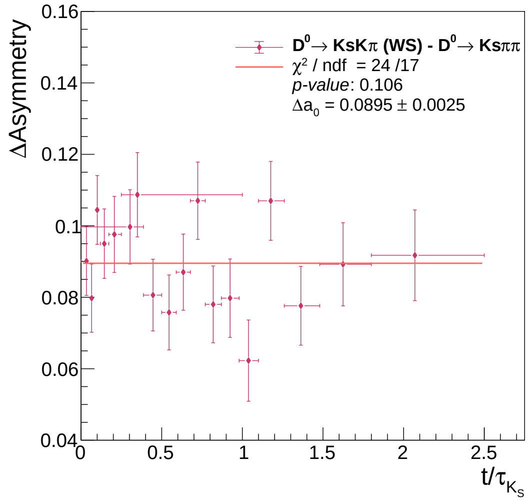

(b) WS sample, 2016.

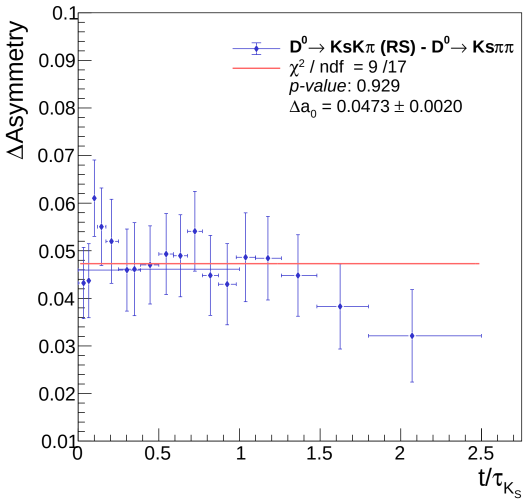

(c) RS sample, 2017. Reversing of the $A^{\pi\pi}_{raw}$ data.

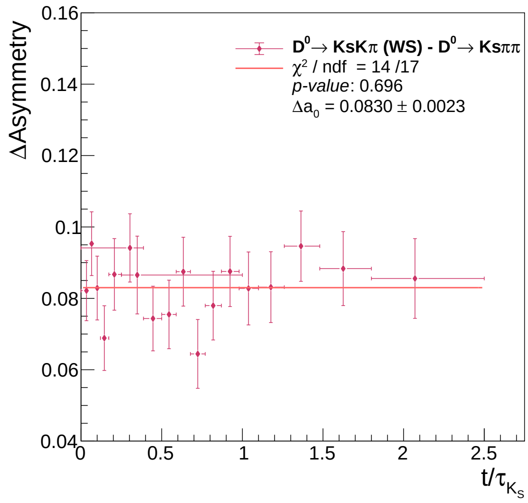

(d) WS sample, 2017.

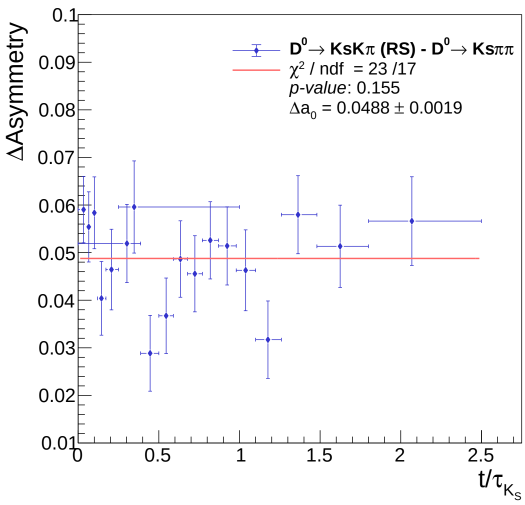

(e) RS sample, 2018. Reversing of the $A^{\pi\pi}_{raw}$ data.

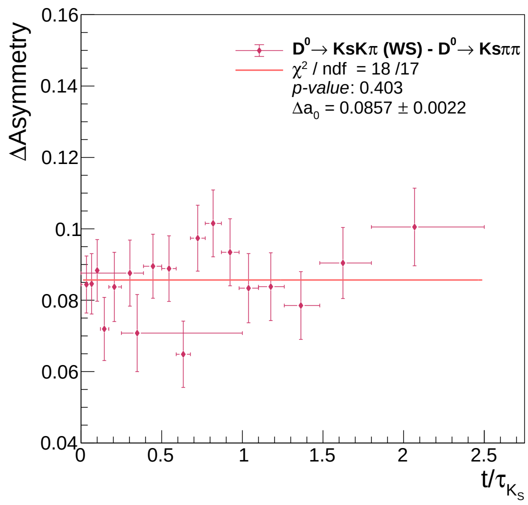

(f) WS sample, 2018.

Figure C.10

Bibliography

[1] N. Cabibbo, *Unitary Symmetry and Leptonic Decays*, Phys. Rev. Lett. **10** (1963) 531.

[2] M. Kobayashi and T. Maskawa, *CP Violation in the Renormalizable Theory of Weak Interaction*, Prog. Theor. Phys. **49** (1973) 652.

[3] LHCb, R. Aaij *et al.*, *Observation of CP Violation in Charm Decays*, Phys. Rev. Lett. **122** (2019), no. 21 211803, `arXiv:1903.08726`.

[4] M. Chala, A. Lenz, A. V. Rusov, and J. Scholtz, *ΔA_{CP} within the Standard Model and beyond*, JHEP **07** (2019) 161, `arXiv:1903.10490`.

[5] H.-N. Li, C.-D. Lü, and F.-S. Yu, *Implications on the first observation of charm CPV at LHCb*, `arXiv:1903.10638`.

[6] Y. Grossman and S. Schacht, *The emergence of the $\Delta U = 0$ rule in charm physics*, JHEP **07** (2019) 020, `arXiv:1903.10952`.

[7] A. Soni, *Resonance enhancement of Charm CP*, `arXiv:1905.00907`.

[8] LHCb, R. Aaij *et al.*, *Studies of the resonance structure in $D^0 \to K^0_S K^{\pm}\pi^{\mp}$ decays*, Phys. Rev. D **93** (2016), no. 5 052018, `arXiv:1509.06628`.

[9] U. Nierste and S. Schacht, *Neutral $D \to KK^*$ decays as discovery channels for charm CP violation*, Phys. Rev. Lett. **119** (2017), no. 25 251801, `arXiv:1708.03572`.

[10] CLEO, J. Insler *et al.*, *Studies of the decays $D^0 \to K^0_S K^-\pi^+$ and $D^0 \to K^0_S K^+\pi^-$*, Phys. Rev. D **85** (2012) 092016, `arXiv:1203.3804`, [Erratum: Phys.Rev.D 94, 099905 (2016)].

[11] Particle Data Group, P. A. Zyla *et al.*, *Review of Particle Physics*, PTEP **2020** (2020), no. 8 083C01.

[12] R. Huerta and R. Pérez-Marcial, *Comment on "commutator of the quark mass matrices in the standard electroweak model and a measure of maximal* CP *nonconservation"*, Phys. Rev. Lett. **57** (1986) 2874.

[13] M. S. Sozzi, *Discrete symmetries and CP violation: from experiment to theory*, Oxford Graduate Texts, Oxford Univ. Press, New York, NY, 2008. doi: 10.1093/acprof:oso/9780199296668.001.0001.

[14] A. Pich, *CP violation*, ICTP Ser. Theor. Phys. **10** (1994) 14, `arXiv:hep-ph/9312297`.

[15] M. Gersabeck, *Introduction to Charm Physics*, PoS **FWNP** (2015) 001, `arXiv:1503.00032`.

[16] V. Weisskopf and E. Wigner, *Over the natural line width in the radiation of the harmonius oscillator*, Z. Phys. **65** (1930) 18.

[17] J. D. Bjorken and S. L. Glashow, *Elementary Particles and SU(4)*, Phys. Lett. **11** (1964) 255.

[18] E598, J. J. Aubert *et al.*, *Experimental Observation of a Heavy Particle J*, Phys. Rev. Lett. **33** (1974) 1404.

[19] SLAC-SP-017, J. E. Augustin *et al.*, *Discovery of a Narrow Resonance in e^+e^- Annihilation*, Phys. Rev. Lett. **33** (1974) 1406.

[20] LHCb, R. Aaij *et al.*, *Measurements of prompt charm production cross-sections in pp collisions at $\sqrt{s} = 13$ TeV*, JHEP **03** (2016) 159, `arXiv:1510.01707`, [Erratum: JHEP 09, 013 (2016), Erratum: JHEP 05, 074 (2017)].

[21] LHCb, R. Aaij *et al.*, *Prompt charm production in pp collisions at sqrt(s)=7 TeV*, Nucl. Phys. B **871** (2013) 1, `arXiv:1302.2864`.

[22] H.-Y. Cheng and C.-W. Chiang, *Direct CP violation in two-body hadronic charmed meson decays*, Phys. Rev. D **85** (2012) 034036, `arXiv:1201.0785`, [Erratum: Phys.Rev.D 85, 079903 (2012)].

[23] B. Guegan, J. Hardin, J. Stevens, and M. Williams, *Model selection for amplitude analysis*, JINST **10** (2015), no. 09 P09002, `arXiv:1505.05133`.

[24] J. M. Blatt and V. F. Weisskopf, *Theoretical nuclear physics*, Courier Corporation, 1991.

[25] LHCb, R. Aaij *et al.*, *Measurement of the D+/- production asymmetry in 7 TeV pp collisions*, Phys. Lett. B **718** (2013) 902, `arXiv:1210.4112`.

[26] S. Stahl, *Measurement of CP asymmetry in muon-tagged $D^0 \to K^-K^+ and D^0 \to \pi^-\pi^+$ decays at LHCb*, PhD thesis, 2014.

[27] LHCb, R. Aaij *et al.*, *Measurement of CP asymmetry in $D^0 \to K^-K^+$ decays*, Phys. Lett. B **767** (2017) 177, `arXiv:1610.09476`.

[28] *LHC Machine*, JINST **3** (2008) S08001.

[29] B. Muratori and T. Pieloni, *Luminosity levelling techniques for the LHC*, in *ICFA Mini-Workshop on Beam-Beam Effects in Hadron Colliders*, pp. 177–181, 2014. `arXiv:1410.5646`. doi: 10.5170/CERN-2014-004.177.

[30] LHCb RICH, A. Papanestis and C. D'Ambrosio, *Performance of the LHCb RICH detectors during the LHC Run II*, Nucl. Instrum. Meth. A **876** (2017) 221, `arXiv:1703.08152`.

[31] T. Sjostrand, S. Mrenna, and P. Z. Skands, *PYTHIA 6.4 Physics and Manual*, JHEP **05** (2006) 026, `arXiv:hep-ph/0603175`.

[32] LHCb collaboration, C. Elsässer, *$\bar{b}b$ production angle plots*, `https://twiki.cern.ch/twiki/bin/view/LHCb/VertexFitters`.

[33] L. Collaboration, *LHCb VELO Upgrade Technical Design Report*, Tech. Rep. CERN-LHCC-2013-021. LHCB-TDR-013, Nov, 2013.

[34] LHCb, *LHCb: Inner tracker technical design report*, Tech. Rep. CERN-LHCC-2002-029, 11, 2002.

[35] LHCb Outer Tracker Group, R. Arink *et al.*, *Performance of the LHCb Outer Tracker*, JINST **9** (2014), no. 01 P01002, `arXiv:1311.3893`.

[36] LHCb RICH Group, M. Adinolfi *et al.*, *Performance of the LHCb RICH detector at the LHC*, Eur. Phys. J. C **73** (2013) 2431, `arXiv:1211.6759`.

[37] LHCb, E. Picatoste Olloqui, *LHCb preshower(PS) and scintillating pad detector (SPD): Commissioning, calibration, and monitoring*, J. Phys. Conf. Ser. **160** (2009) 012046.

[38] I. Machikhiliyan *et al.*, *Current status and performance of the lhcb electromagnetic and hadron calorimeters*, in *Journal of Physics: Conference Series*, vol. 293, p. 012052, IOP Publishing, 2011.

[39] J. Alves, A.Ã. *et al.*, *Performance of the LHCb muon system*, JINST **8** (2013) P02022, `arXiv:1211.1346`.

[40] T. Head, *The LHCb trigger system*, JINST **9** (2014) C09015.

[41] S. Benson, V. Gligorov, M. A. Vesterinen, and J. M. Williams, *The lhcb turbo stream*, in *J. Phys. Conf. Ser*, vol. 664, p. 082004, 2015.

[42] LHCb, R. Aaij *et al.*, *Design and performance of the LHCb trigger and full real-time reconstruction in Run 2 of the LHC*, JINST **14** (2019), no. 04 P04013, `arXiv:1812.10790`.

[43] T. Likhomanenko *et al.*, *LHCb Topological Trigger Reoptimization*, J. Phys. Conf. Ser. **664** (2015), no. 8 082025, `arXiv:1510.00572`.

[44] `https://twiki.cern.ch/twiki/bin/view/LHCb/DecayTreeFitter`.

[45] `https://twiki.cern.ch/twiki/bin/view/LHCb/VertexFitters`.

[46] `https://twiki.cern.ch/twiki/bin/view/LHCb/TrackingEffAbsLength`.

[47] LHCb, R. Aaij *et al.*, *Measurement of the mass difference between neutral charm-meson eigenstates*, Phys. Rev. Lett. **122** (2019), no. 23 231802, `arXiv:1903.03074`.

[48] N. L. Johnson, *Systems of frequency curves generated by methods of translation*, Biometrika **36** (1949) 149.

[49] G. Bohm and G. Zech, *Statistics of weighted Poisson events and its applications*, Nucl. Instrum. Meth. A **748** (2014) 1, `arXiv:1309.1287`.

[50] A. Roodman, *Blind analysis in particle physics*, eConf **C030908** (2003) TUIT001, `arXiv:physics/0312102`.

[51] LHCb, R. Aaij *et al.*, *Updated determination of D^0-$\overline{D}^0$ mixing and CP violation parameters with $D^0 \to K^+\pi^-$ decays*, Phys. Rev. D **97** (2018), no. 3 031101, `arXiv:1712.03220`.

[52] LHCb, R. Aaij *et al.*, *Physics case for an LHCb Upgrade II - Opportunities in flavour physics, and beyond, in the HL-LHC era*, `arXiv:1808.08865`.